Spectroscopic and Crystallographic Characterization of Peroxo- and Oxoiron Complexes

A DISSERTATION
SUBMITTED TO THE FACULTY OF THE GRADUATE SCHOOL
OF THE UNIVERSITY OF MINNESOTA
BY

Jonathan Robert Frisch

IN PARTIAL FULFILLMENT OF THE REQUIREMENTS
FOR THE DEGREE OF
DOCTOR OF PHILOSOPHY

Professor Lawrence Que, Jr., Adviser

January, 2010

Acknowledgements

None of this work would have been possible without the opportunities given to me by Professor Lawrence Que, Jr. and the funding provided by the National Institutes of Health. Many people have assisted and influenced me during my time in Larry's lab and I would like to use this space to thank the ones who had the greatest impact on my research. One of the first people I met upon joining Larry's group was Dr. Michael Jensen. Mike is an excellent scientist who was not put off by my obsessive attention to detail. In fact, he encouraged it by citing cases where a small thing was overlooked by many people until it was noticed by someone else, thus leading to a better understanding of a problem. My detail-oriented personality also meshed well with that of X-ray crystallographer Dr. Victor Young, Jr., under whose tutelage I discovered the minutiae involved in the art of solving crystal structures. I think if Larry had known how much time I would end up spending in the crystallography lab, he would never have encouraged me to learn the technique. I am also indebted to Dr. William Brennessel and Benjamin Kucera for helping me to learn crystallography.

Much of my work hinged on collaborations with spectroscopists. Chief among these is Van Van Vu, who went above and beyond when we were trying to sort out thorny EXAFS issues. In addition to acting as my go-to EXAFS specialist, Van operated as a great sounding board and we spent many hours in fruitful discussions. Mössbauer spectroscopy was also integral to my work, and I

feel compelled to thank Professor Eckard Münck for the use of his facilities at Carnegie Mellon University and more importantly, Dr. Marlène Martinho for doing the actual spectroscopy.

Many of the complexes which I discuss in this work were prepared or provided by others. These scientists include Dr. Jason England, Dr. Kallol Ray, Dr. Genqiang "Ken" Xue, Dr. Anna Company, Clyde Cady and Laura Gomez. In addition to giving me materials, they also offered encouragement and enlightenment, particularly Jason, Kallol and Ken, with whom I spent far too many hours conferring.

Finally, I wish to thank everyone else with whom I have worked over the last few years. It was a long, hard road and I wouldn't have made it without you.

Jonathan R. Frisch

January 2010

For Jennifer,

my darling wife

and

the love of my life.

She knows why…

Abstract

Nonheme oxygen activating enzymes are found as both diiron and monoiron complexes. Prior to undertaking substrate oxidation, many diiron enzymes produce (μ-peroxo)diiron(III) intermediates, while the catalytically important oxidant found in most monoiron enzymatic cycles is an oxoiron(IV) moiety. Synthetic chemists design small molecules to serve as models for study of these transient species. This work is intended to supplement what is known about both synthetic (μ-peroxo)diiron(III) and oxoiron(IV) complexes.

A series of diiron(II) compounds was synthesized and reacted with oxygen. Through ligand rearrangements, some of the resultant (μ-η^1:η^1-peroxo)diiron(III) species initially observed converted to secondary (μ-η^1:η^1-peroxo)diiron(III) intermediates exhibiting spectroscopic features akin to complexes already known. The identities of oxyanion bridges present in the diiron(II) precursors drastically affected the stability of the (μ-η^1:η^1-peroxo)diiron(III) species initially produced upon oxygenation. Upon decay, compounds of this type putatively produce tetranuclear iron(III) clusters. A set of these clusters was synthesized and examined via x-ray crystallography. Also, a new method was developed for examining oxoiron(IV) intermediates using resonance Raman spectroscopy.

Synthetic complexes are often used as models for biological systems. A thorough understanding of these models may lead to catalytic systems usable on an industrial scale.

Table of Contents

List of Tables

List of Figures

List of Schemes

Chapter 1: Dinuclear and Mononuclear Nonheme Iron Enzymes and Their Synthetic Analogues

1.1 Introduction

It is not surprising that nearly all aerobic life on Earth depends on iron. It is the most abundant transition metal on the planet and as such, it is readily available to almost every organism. What is surprising is the enormous number of ways in which enzymes put it to use. The list of reactions mediated by iron-dependent biological systems is nearly endless. Without this innocuous metal as the catalyst for these reactions, life as it evolved on Earth would not exist. Addressing all of these reactions would take several lifetimes, so we will direct our attention instead to a small subset of iron-using enzymes. This group consists of enzymes that employ iron to activate dioxygen for use in oxidative catalysis.[1-4] Again, we find an overwhelming amount of information about these systems, so we will once more pare our subject matter. These systems can be divided into two smaller categories, heme and nonheme enzymes. Leaving aside the heme-based enzymes, we will focus this work on nonheme iron-dependent enzymes that take part in oxidative catalysis.

These enzymes are of great interest, because they perform difficult reactions at ambient pressures and temperatures. Some of these reactions are undertaken on industrial scales by humans, but rarely are we capable of replicating biological chemistry in the absence of increased pressures and temperatures. Add to this the fact that many of these industrial processes require toxic and heavy metal catalysts, and the reason for the desire to understand and

mimic natural systems becomes apparent. Part of the process of investigating these enzymes involves synthetic chemistry. This is because biological systems are very efficient, meaning it is often difficult, if not impossible to trap and characterize catalytic cycle intermediates. To counter this problem, chemists design and synthesize complexes intended to be analogous to the active sites of enzymes. Billions of years of evolution produced these biological systems, so it should come as no surprise that the synthetic copies are almost invariably slower and less efficient. This slowness and inefficiency works to the advantage of spectroscopists attempting to study transient intermediates. It allows them to trap and characterize synthetic species which hopefully sheds light on the character of their biological counterparts. This thesis is primarily about spectroscopic characterization of synthetic intermediates intended to mimic those produced by the two classes of nonheme iron enzymes, di- and monoiron systems.

1.2 Diiron systems

Diiron enzymes capable of dioxygen activation constitute an ever growing family.[1,3,5-10] Among the best known of these enzymes are soluble methane monooxygenase (sMMOH), the R2 subunit of class I ribonucleotide reductases (RNR), toluene and *o*-xylene monooxygenases, phenol hydroxylase and stearoyl acyl carrier protein Δ^9-desaturase. Interest in these enzymes has been piqued, because despite their similar active sites, they catalyze a wide variety of reactions. These include oxygen atom insertion into an alkane C-H bond by sMMOH,

oxygen atom insertion into aromatic C-H bonds by toluene and *o*-xylene monooxygenases and phenol hydroxylase, extraction of a hydrogen atom to produce a stable tyrosyl radical by class I RNR and dehydrogenation of a fatty acid hydrocarbon chain by stearoyl acyl carrier protein Δ^9-desaturase. Interestingly, one of the steps in the catalytic cycles of most of these enzymes is production of peroxide-bridged diiron(III) intermediates. For some enzymes, these intermediates are stable enough to be detected and characterized.[11-19] While these peroxo-iron(III) moieties are well-studied, an understanding of their role in biological reactions remains elusive. Because biological molecules are often difficult to work with due to solvent and temperature limitations, various biomimetic diiron complexes have been synthesized and characterized.[20-29] As with the biological systems they are designed to emulate, these synthetic compounds often produce peroxide-bridged diiron(III) species. Most prevalent among these synthetic diiron complexes are a class of carboxylate-bridged compounds, which can be used to produce the common motif of a (μ-η^1:η^1-peroxo)diiron(III) moiety.

As the point of catalysis is to speed up otherwise untenable reactions, it is odd that many of the biological catalytic cycles include quasi-stable peroxide intermediates. Synthetic analogues share this quasi-stability as evidenced by the number of trapped and characterized peroxo moieties.[20-24] These synthetic systems often employ carboxylate bridges as supports for the (μ-peroxo)diiron(III)

species formed. In fact, non-carboxylate bridges are so rare that only two papers report (μ-peroxo)diiron(III) complexes with them.[30,31]

1.3 Monoiron systems

Nonheme oxygen-activating monoiron enzymes also encompass a wide variety of species.[4,32] These include intradiol-cleaving catechol dioxygenases, extradiol-cleaving catechol dioxygenases, lipoxygenases, pterin-dependent hydroxylases and Rieske dioxygenases among others. As their names imply, the types of reactions performed by these systems also vary widely. As with the biological diiron systems, solvent and temperature constraints limit the study of monoiron enzymes, so synthetic complexes have been produced in attempts to mimic the catalytic behavior of the natural systems.[33] Because oxoiron(IV) intermediates are often the oxidative species in biological catalytic cycles, synthesizing, trapping and characterizing synthetic oxoiron(IV) species is of paramount importance to the study of monoiron systems. Resonance Raman (rR) spectroscopy has been employed as an investigative technique to examine the frequency of the Fe-O stretches in oxoiron(IV) intermediates. However, most oxoiron(IV) species have little or no absorbance in the visible spectrum, making rR spectroscopy an underutilized technique. For this reason, only a small number of synthetic nonheme oxoiron(IV) papers have been published with rR investigation of Fe-O stretches included.[34-39]

1.4 Scope and Aim of Thesis

The nature of the bridging peroxides present in various diiron enzyme catalytic cycles is still in question. Even more in question is how the O-O bond is broken prior to participation in oxidative reactions. In Chapters 2 and 3 of this thesis, we will examine how small changes in the molecules coordinating to the iron atoms in synthetic systems can influence both the nature and the stability of (μ-peroxo)diiron(III) moieties synthesized as analogues for biological intermediates.

Upon decay, (μ-peroxo)diiron(III) intermediates often crystallize into tetranuclear complexes. The ligands surrounding the iron atoms in these species take on a bewildering array of conformations. In Chapter 4, we will use x-ray crystallography to examine a series of tetranuclear complexes and attempt to relate ligand conformations to possible decay pathways.

Many oxoiron(IV) oxide-to-iron charge transfer bands lie in the UV region. This has made rR spectroscopic investigation rather difficult. As a technique, rR spectroscopy relies on photo-excitation into a chromophore. This is a problem for two reasons: *(i)* excitation with an UV laser often results in photoreduction of the highly oxidized iron(IV) center and *(ii)* moving to lower excitation frequencies to avoid this issue results in poor resonance enhancement as the longer wavelengths are no longer coincident with the wavelengths absorbed by the oxoiron(IV)

chromophore. In Chapter 5, we will address these problems and introduce a new method for rR spectroscopy of oxoiron(IV) complexes.

Chapter 2: Characterization of Two (μ-η^1:η^1-Peroxo)Diiron(III) Intermediates Produced from a Single Diiron(II) Precursor

2.1 Introduction

Over the last twenty years, a growing family of oxygen-activating, non-heme diiron enzymes has been revealed and cataloged.[1,3,5-10] Most notably, this group includes soluble methane monooxygenase, the R2 subunit of class I ribonucleotide reductases, toluene and *o*-xylene monooxygenases, phenol hydroxylase and stearoyl acyl carrier protein Δ^9-desaturase. The catalytic cycles of several of these enzymes include peroxide-bridged diiron(III) intermediates that are stable enough to be detected and characterized.[11-19] The precise role of the peroxide moieties commonly observed in biological reactions remains poorly understood, in spite of the existence of a fairly large body of work describing them. To complement these biological studies, a variety of biomimetic diiron complexes has been synthesized and characterized.[20-29] Using synthetic compounds, it is also not unusual to observe peroxide-bridged diiron(III) species, especially in carboxylate-bridged complexes, wherein a common motif is a (μ-η^1:η^1-peroxo)diiron(III) moiety.

It is curious that nature evolved mechanisms that include quasi-stable peroxide intermediates as steps along catalytic pathways. The growing number of trapped and characterized synthetic analogues to these peroxo moieties indicates that this inherent stability is not limited to biological systems.[20-24] Carboxylates are most often used as bridges supporting the (μ-peroxo)diiron(III) species, with only two papers reporting (μ-peroxo)diiron(III) complexes with non-carboxylate

bridges.[30,31] To investigate how substitution of the carboxylate bridge would affect the properties of the (μ-peroxo)diiron(III) unit, we synthesized and crystallized two diiron(II) complexes using the ligand N-EtHPTB (anion of *N,N,N′N′*-tetrakis(2-benzimidazolylmethyl)-2-hydroxy-1,3-diaminopropane), wherein the benzoate bridge of $[Fe_2(\text{N-EtHPTB})(O_2CPh)]^{2+}$ (**1**•O_2CPh), a complex first reported in 1990 by Ménage *et al.*,[40] is replaced with diphenylphosphinate (**1**•O_2PPh_2) or dimethylarsinate (**1**•O_2AsMe_2). Reaction of these new species with O_2 produces (μ-η^1:η^1-peroxo)diiron(III) moieties that exhibit surprising behaviors. In this paper we report the crystallographic details of the precursor diiron(II) complexes and the spectroscopic characterization of their dioxygen adducts.

2.2 Experimental Section

2.2.1 Materials and Syntheses

All reagents and solvents were purchased from commercial sources and were used as received, unless noted otherwise. The $^{18}O_2$ (97%) and the $^{16}O_2$:$^{16}O^{18}O$:$^{18}O_2$ mixture (1:2:1) were purchased from Cambridge Isotope Laboratories, Inc., Andover, MA. The ligand N-EtHPTB was synthesized using a published procedure.[41] Solvents were dried according to published procedures and distilled under Ar prior to use.[42] Preparation and handling of air sensitive materials were carried out under an inert atmosphere by using either standard

Schlenk and vacuum line techniques or a glovebox. Elemental analyses were performed by Atlantic Microlab, Inc., Norcross, GA.

1•O_2PPh_2. N-EtHPTB (181 mg, 0.250 mmol) was dissolved in MeOH (~10 mL) along with Et_3N (0.19 mL, 1.4 mmol). Diphenylphosphinic acid (54.5 mg, 0.250 mmol) was added and allowed to dissolve. $Fe(OTf)_2$•2MeCN (238 mg, 0.546 mmol) was added, producing a yellow solution. After 5 minutes, $NaBPh_4$ (180 mg, 0.526 mmol) was added, resulting in immediate precipitation of a white powder. The solid was filtered and dried *in vacuo*. Recrystallization from MeCN and Et_2O produced colorless crystals, some suitable for X-ray diffraction structural analysis. Yield: 341 mg (79%). Anal. for [Fe_2(N-EtHPTB)(O_2PPh_2)](BPh_4)$_2$ and calcd for $C_{105}H_{102}B_2Fe_2N_{11}O_3P$: C, 72.89; H, 5.94; N, 8.90%. Found: C, 72.87; H, 5.97; N, 8.84%.

1•O_2AsMe_2. N-EtHPTB (146.3 mg, 0.202 mmol) was dissolved in MeOH (~10 mL) along with Et_3N (0.141 mL, 1.01 mmol). Dimethylarsinic acid (30.0 mg, 0.217 mmol) was added and allowed to dissolve. $Fe(OTf)_2$•2MeCN[43] (182.7 mg, 0.419 mmol) was added, producing a yellow solution. After 5 minutes, $NaBPh_4$ (212.8 mg, 0.622 mmol) was added, resulting in immediate precipitation of a white powder. The solid was filtered and dried *in vacuo*. Recrystallization from MeCN and Et_2O produced pale yellow crystals, some suitable for X-ray diffraction structural analysis. Yield: 270 mg (93%). Anal. for [Fe_2(N-

EtHPTB)(O_2AsMe_2)](BPh_4)(OTf) and calcd for $C_{70}H_{75}AsBF_3Fe_2N_{10}O_6S$: C, 58.43; H, 5.25; N, 9.73%. Found: C, 58.62; H, 4.97; N, 9.74%.

1•O_2CPh. N-EtHPTB (107.6 mg, 0.149 mmol) was dissolved in MeOH (~10 mL) along with Et_3N (0.11 mL, 0.82 mmol). Sodium benzoate (23.1 mg, 0.160 mmol) was added and allowed to dissolve. $Fe(OTf)_2$•2MeCN (144.4 mg, 0.331 mmol) was added, producing a yellow solution. After 5 minutes, $NaBPh_4$ (119 mg, 0.348 mmol) was added, resulting in immediate precipitation of a white powder. The solid was filtered and dried *in vacuo*. Recrystallization from MeCN and Et_2O produced pale yellow-green crystals. Yield: 132 mg (71%). Anal. for [Fe_2(N-EtHPTB)(O_2CPh)](OTf)$_2$ and calcd for $C_{52}H_{54}F_6Fe_2N_{10}O_9S_2$: C, 49.85; H, 4.34; N, 11.18%. Found: C, 49.70; H, 4.38; N, 10.72%.

2.2.2 Physical Methods

UV-Vis spectra were recorded on a Hewlett-Packard 8453 diode array spectrophotometer. Resonance Raman spectra were collected on an ACTON AM-506M3 monochromator with a Princeton LN/CCD data collection system using a Spectra-Physics Model 2060 krypton laser. Low-temperature spectra of the peroxo intermediates in CH_2Cl_2 and MeCN were obtained at 77 K using a 135° backscattering geometry. Samples were frozen onto a gold-plated copper cold finger in thermal contact with a Dewar flask containing liquid nitrogen. Raman frequencies were referenced to the features of indene. Slits were set for a band-pass of 4 cm^{-1} for all spectra. Mössbauer spectra were recorded with two

spectrometers, using Janis Research Super-Varitemp dewars that allowed studies in applied magnetic fields up to 8.0 T in the temperature range from 1.5 to 200 K. Mössbauer spectral simulations were performed using the WMOSS software package (WEB Research, Edina, MN). Isomer shifts are quoted relative to Fe metal at 298 K.

X-ray crystallography. X-ray diffraction data were collected on a Bruker SMART platform CCD diffractometer at 173(2) K.[44] Preliminary sets of cell constants were calculated from reflections harvested from three sets of 20 frames. These initial sets of frames were oriented such that orthogonal wedges of reciprocal space were surveyed. The data collection was carried out using MoKα radiation (graphite monochromator). Randomly oriented regions of reciprocal space were surveyed to the extent of one sphere and to a resolution of 0.84 Å. The intensity data were corrected for absorption and decay using SADABS.[45] Final cell constants were calculated after integration with SAINT.[46] The structures were solved and refined using SHELXL-97.[47] The space group $P2_1/c$ was determined based on systematic absences and intensity statistics. Direct-methods solutions were calculated which provided most non-hydrogen atoms from the E-map. Full-matrix least squares / difference Fourier cycles were performed which located the remaining non-hydrogen atoms. All non-hydrogen atoms were refined with anisotropic displacement parameters. All hydrogen atoms were placed in ideal positions and refined as riding atoms with relative

isotropic displacement parameters. Brief crystal data and intensity collection parameters for the crystalline complexes are shown in Table 2.1.

X-ray absorption spectroscopy. XAS data were collected on beamline 9-3 at Stanford Synchrotron Radiation Lightsource (SSRL) of the SLAC National Accelerator Laboratory and on beamline X3B at the National Synchrotron Lightsource of Brookhaven National Laboratory (NSLS). At SSRL, the synchrotron ring SPEAR was operated at 3.0eV and 50-100 mA beam current. Energy resolution of the focused incoming X-rays was achieved using a Si(220) double crystal monochromator, which was then detuned to 50% of maximal flux to attenuate second harmonic X-rays. At NSLS, the synchrotron ring was operated at 2.8 GeV and 100-300 mA beam current and a Si(111) double crystal monochromator was used. Fluorescence data were collected over the energy range of 6.8 - 8.0 keV using a 30-element Ge detector (SSRL) or 13-element Ge detector (NSLS). The beam spot size on samples was 5 mm (horizontal) x 1 mm (vertical). Thirteen scans were collected for **2**•O_2AsMe_2 at NSLS (55 minutes/scan) and fourteen scans were collected for **2**•O_2PPh_2 and **3**•O_2PPh_2 at SSRL (25 minutes/scan). All spectra were referenced against an iron foil.

Pre-edge quantification was carried out with the SSExafs program using a standard procedure.[48] Standard procedures were used to reduce, average and process the raw data using the EXAFSPAK package,[49] which was also used for EXAFS fitting. Theoretical EXAFS amplitude and phase functions were

calculated using the FEFF package (version 8.4). The input models for FEFF calculations are shown in Figures A2.1 and A2.2. The parameters *r* and σ^2 were floated, while n was kept fixed for each fit and systematically varied in integer steps between fits. Scale factor was fixed at 0.9 and threshold energy (E_0) was varied but maintained at a common value for all shells. The goodness of fit (GOF) was determined using Equation 1:

$$F = \sqrt{\sum k^6 (\ddot{O}_{exp} - \ddot{O}_{cal})^2 / N}$$

Eq. (1)

where *N* is the number of data points.[50]

2.3 Results

Several diiron enzymes activate O_2 via (μ-η^1:η^1-peroxo)diiron(III) intermediates.[11-16,18] In order to better understand the behavior of these biological moieties, we synthesized two diiron(II) complexes and characterized their O_2 adducts. Combining two equivalents of $Fe(OTf)_2$•2MeCN with one equivalent of the ligand N-EtHPTB followed by addition of one equivalent of either diphenylphosphinic acid or dimethylarsinic acid afforded complexes with the general formulation $[Fe_2(N\text{-}EtHPTB)(O_2X)](Y)_2$ (cation = **1**•O_2X where O_2X = O_2PPh_2 or O_2AsMe_2 and Y = counter anions). Recrystallization of these compounds from MeCN and diethyl ether produced crystals suitable for X-ray diffraction structural analysis (Table 2.1). In solution, these complexes reacted

with dioxygen at low temperatures, producing intermediates that were characterized using UV-Vis, resonance Raman, Mössbauer and X-ray absorption spectroscopies.

2.3.1 X-ray Crystallography

The results from analysis of the **1**•O_2PPh_2 and **1**•O_2AsMe_2 structures are compared in Table 2.2 with information from the previously published crystal structure of **1**•O_2CPh.[40,51] Figure 2.1 shows an ORTEP view of **1**•O_2PPh_2 with the hydrogen atoms removed as well as a cartoon of the general structure shared by all three cations. In each complex, both metal atoms are five-coordinate iron(II) and form a six-membered ring along with three atoms of the bridging moiety and the ligand alkoxide oxygen. Other similarities include distorted trigonal-bipyramidal iron centers, the axial positions of which are occupied by amine nitrogen atoms and bridging moiety oxygen atoms. The equatorial sites are occupied by benzimidazole nitrogen atoms and the alkoxide oxygen atom. For the most part, the interatomic distances and angles do not significantly fluctuate between species. However, variations of note include the O-C-O, O-P-O and O-As-O angles formed by the three-atom linkers between the iron atoms, with values of 113.26(7) (**1**•O_2AsMe_2), 115.59(13) (**1**•O_2PPh_2) and 124.2(7) (**1**•O_2CPh) degrees, and the geometry about the iron atoms, with average τ values[52] of 0.81 (**1**•O_2AsMe_2), 0.77 (**1**•O_2PPh_2) and 0.93 (**1**•O_2CPh).

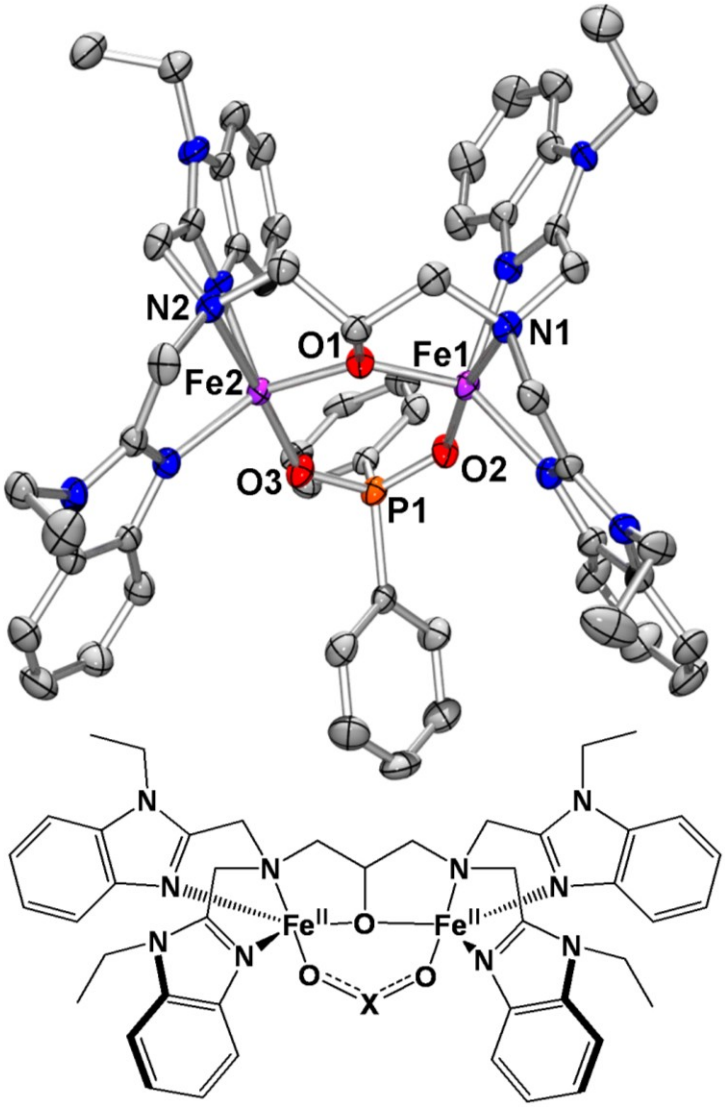

Figure 2.1. Crystal structure of the cation **1**•O_2PPh_2 (50% ellipsoids) with hydrogen atoms removed. Generic cartoon of **1**•O_2X: O_2X = O_2AsMe_2 (**1**•O_2AsMe_2), O_2PPh_2 (**1**•O_2PPh_2), O_2CPh (**1**•O_2CPh).

Clearly, the differences observed between the three-atom linker angles in each complex result from the different hybridization of the central atom. The central carbon atom in the benzoate bridge is sp^2 hybridized, producing an angle

three degrees greater than the ideal 120 degrees predicted for trigonal planar geometry. As the benzoate oxygen atoms bind to the iron atoms, they must spread apart to accommodate the inter-iron distance (3.4749(31) Å), producing an O-C-O angle of 124.2(7) degrees. The same effect is observed in the diphenylphosphinate and dimethylarsinate bridged complexes, where the central atom in each three-atom linker is sp^3 hybridized. However, instead of producing angles of 109.5 degrees, the ligated oxygen atoms are forced apart to accommodate the inter-iron distances of 3.5357(5) (**1**•O_2AsMe_2) and 3.5405(10) (**1**•O_2PPh_2) Å, producing respective O-As-O and O-P-O angles of 113.26(7) and 115.59(13) degrees.

Interestingly, the inter-iron distances found in **1**•O_2AsMe_2 and **1**•O_2PPh_2 are greater than that found in **1**•O_2CPh, in spite of the fact that the former complexes produce sharper angles with their three-atom linkers. Examination of the bond lengths between the oxygen atoms and the central atom in the three-atom linker of each complex reveals a trend with distances in **1**•O_2AsMe_2 being ~0.16 Å longer than those in **1**•O_2PPh_2, which in turn contains distances ~0.25 Å than those found in **1**•O_2CPh. The longer As-O and P-O bond lengths found in **1**•O_2AsMe_2 and **1**•O_2PPh_2 result in significantly increased O···O bite distances of 2.7991(21) (**1**•O_2AsMe_2) and 2.5600(32) Å (**1**•O_2PPh_2) versus 2.2251(74) Å (**1**•O_2CPh). This shorter distance in **1**•O_2CPh is reflected in a shorter inter-iron

distance, in spite of the fact that the three-atom linker has a wider angle than the linkers in either **1**•O_2PPh_2 or **1**•O_2AsMe_2.

Table 2.1. Crystal data and structure refinement for **1**•$O_2PPh_2(BPh_4)_2$•MeCN and **1**•$O_2AsMe_2(BPh_4)(OTf)$•MeCN.

	1•$O_2PPh_2(BPh_4)_2$•MeCN	**1**•$O_2AsMe_2(BPh_4)(OTf)$ •MeCN
empirical formula	$C_{105}H_{102}B_2Fe_2N_{11}O_3P$	$C_{72}H_{78}BF_3$ $Fe_2N_{11}O_6S$
fw	1730.27	1479.94
T (K)	173(2)	173(2)
Mo Kα λ, Å	0.71073	0.71073
space group	$P2_1/c$	$P2_1/c$
a (Å)	18.937(4)	16.1151(12)
b (Å)	23.855(5)	15.6370(12)
c (Å)	21.817(5)	28.473(2)
α (deg)	90	90
β (deg)	114.903(4)	103.4900(10)
γ (deg)	90	90
V (Å^3)	8940(3)	6977.0(9)
Z	4	4
ρ (calc), Mg/m^3	1.286	1.409
abs coeff (mm^{-1})	0.402	0.985
R1[a]	0.0492	0.0338
wR2[b]	0.0957	0.0798

[a] $R1 = \Sigma||F_o|-|F_c|| / \Sigma|F_o|$. [b] $wR2 = [\Sigma[w(F_o^2-F_c^2)^2] / \Sigma [w(F_o^2)^2]]^{1/2}$.

Table 2.2. Selected interatom distances and bond angles for $[Fe_2(N\text{-}EtHPTB)(O_2X)]^{2+}$.

	1•O_2PPh_2	**1**•O_2AsMe_2	**1**•O_2CPh [a]
τ_{ave}	0.77	0.81	0.93
Interatom distances (Å)			
Fe1-O1	2.004(2)	2.0145(13)	1.976(5)
Fe2-O1	1.992(2)	2.0037(14)	1.964(5)
Fe1-N1	2.294(3)	2.3366(16)	2.316(6)
Fe2-N2	2.352(3)	2.3892(16)	2.280(7)
Fe1-O2	2.008(2)	1.9825(14)	2.057(5)
Fe2-O3	2.021(2)	1.9863(14)	2.019(6)
Fe1-N3	2.086(3)	2.1372(17)	2.064(6)
Fe1-N5	2.115(3)	2.1023(18)	2.069(6)
Fe2-N7	2.075(3)	2.1088(17)	2.080(6)
Fe2-N9	2.098(3)	2.0759(17)	2.064(6)
P1/C44/As1-O2	1.514(2)	1.6740(15)	1.264(9)
P1/C44/As1-O3	1.512(2)	1.6776(14)	1.253(9)
Fe1····Fe2	3.5405(10)	3.5357(5)	3.4749(31)
O2····O3	2.5600(32)	2.7991(21)	2.2251(74)
Bond angles (degrees)			
Fe1-O1-Fe2	124.76(11)	123.27(6)	123.8(2)
O1-Fe1-O2	105.55(9)	105.77(6)	98.6(2)
O1-Fe2-O3	99.44(9)	107.92(6)	101.5(2)
Fe1-O2-P1/C44/As1	132.01(14)	127.24(8)	136.4(5)
Fe2-O3-P1/C44/As1	138.88(15)	128.15(8)	133.9(5)
O2-P1/C44/As1-O3	115.59(13)	113.26(7)	124.2(7)

[a] Data for **1**•O_2CPh were re-refined using full-matrix least-squares on F^2 and atoms were renamed to match labeling scheme of **1**•O_2PPh_2 and **1**•O_2AsMe_2. The new solution was deposited directly with the Cambridge Crystallographic Data Centre (deposition number CCDC 731669). Values in the table represent recalculated distances and angles.

2.3.2 UV-Vis Spectroscopy

The UV-Vis spectrum of **1**•O_2PPh_2 in CH_2Cl_2 has no notable features except for a UV tail and an extremely weak absorbance maximum around 1000 nm (Figure 2.2, inset). Bubbling dioxygen through this solution at –80 °C elicits an intense green-blue color (Figure 2.2, solid green line) with absorption maxima at 368 and 678 nm (**2**•O_2PPh_2). Upon warming to –30 °C, the green-blue solution becomes deep blue over an 8-minute period (Figure 2.2, dotted blue line). The absorption maximum at 368 nm shifts to 344 nm while gaining intensity, the maximum at 678 nm shifts to 621 nm with concomitant loss of intensity and a new shoulder appears at 509 nm (Figure A2.3). The complex spectral changes and the lack of true isosbestic points suggest the appearance of more than one species during this time period. Further warming to room temperature produces the final product, a yellow solution (**4**•O_2PPh_2) with no remarkable absorption features in the visible spectrum.

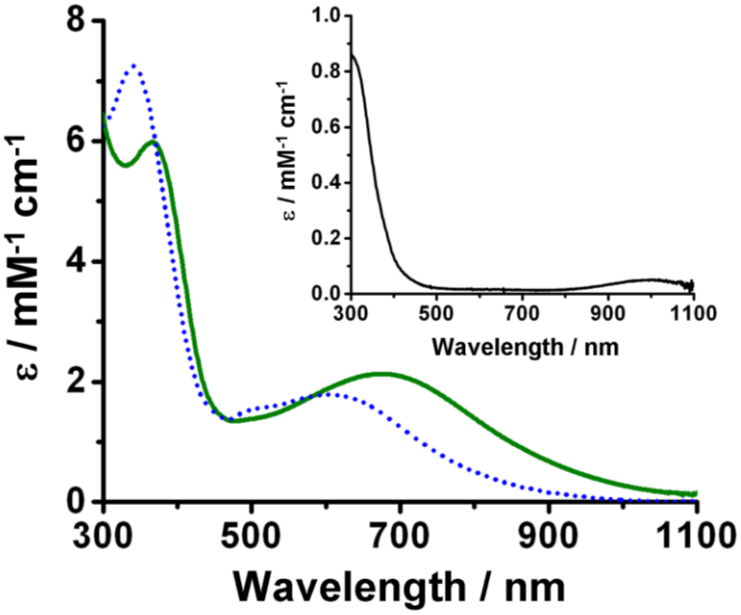

Figure 2.2. UV-Vis spectra of **1**•O_2PPh_2 (inset), **2**•O_2PPh_2 (solid green line) and mostly **3**•O_2PPh_2 (dotted blue line) in CH_2Cl_2.

Oxygenation of **1**•O_2PPh_2 in MeCN at -40 °C produces a green-blue solution (λ_{max} = 686 nm) with spectroscopic characteristics (Figure 2.3, solid green line) similar to those of **2**•O_2PPh_2 in CH_2Cl_2 at -80 °C. However, in contrast to complications observed when warming the latter, warming the MeCN solution to –30 °C and maintaining that temperature for 15 minutes results in clean conversion to a deep blue solution (**3**•O_2PPh_2) with a visible absorption maximum at 590 nm (Figure 2.3, dotted blue line), corresponding to the 588-nm peak observed upon oxygenation of **1**•O_2CPh.[40] Unlike the reaction in CH_2Cl_2, conversion from **2**•O_2PPh_2 to **3**•O_2PPh_2 in MeCN produces true isosbestic points at 363 and 618 nm (Figure A2.2). Warming to room temperature causes

3•O_2PPh_2 to decay to the final product, a yellow solution (**4**•O_2PPh_2) with no remarkable absorption features in the visible spectrum.

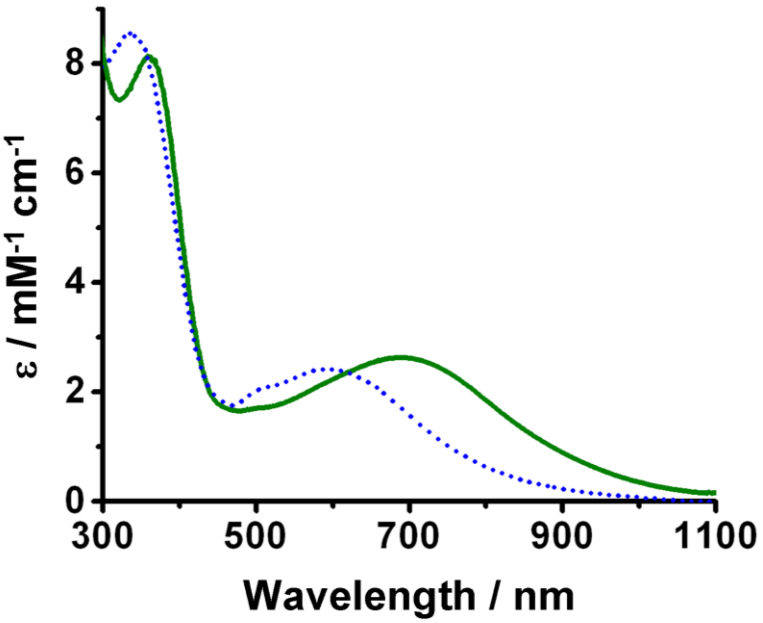

Figure 2.3. UV-Vis spectra recorded at -40 °C in MeCN for **2**•O_2PPh_2 (solid green) and **3**•O_2PPh_2 (dotted blue).

Oxygenation of **1**•O_2AsMe_2 in MeCN at -40 °C changes the almost colorless solution to a deep green-blue color with UV-Vis absorption maxima at 348 and 632 nm (Figure A2.5) associated with **2**•O_2AsMe_2. It exhibits UV-Vis absorption features analogous to those of **2**•O_2PPh_2, but the similarity ends there. Instead of converting to a different species when warmed to -30 °C, **2**•O_2AsMe_2 is stable for more than an hour, at which point observation was aborted. Warming this solution to 0 °C leads to slow decay with ~25% loss of intensity at 632 nm over a four-hour period. Gradual blue-shifting of the absorbance maxima in

conjunction with the presence of time traces that cannot be fit to first-order decay rates leads us to hypothesize that the system passes through an unobserved intermediate (**3**•O_2AsMe_2) comparable to **3**•O_2PPh_2 prior to complete decay to the yellow product (**4**•O_2AsMe_2).

2.3.3 Resonance Raman Spectroscopy

Resonance Raman (rR) spectroscopy is a particularly effective technique for examining vibrational transitions in complexes that have strong chromophores. In light of this fact, rR spectra of **2**•O_2AsMe_2, **2**•O_2PPh_2 and **3**•O_2PPh_2 were collected, analyzed and compared with spectra presented in earlier reports[4,24,29,51,53-56] in an attempt to gain insight into their individual molecular structures.

The rR spectrum of **2**•O_2PPh_2 in frozen CH_2Cl_2 using $^{16}O_2$ and 647.1 nm excitation shows two intense peaks at 845 and 853 cm^{-1} in addition to three peaks at 465, 475 and 490 cm^{-1} (Figure 2.4A, solid red line). These features suggest the presence of an iron(III)-peroxo chromophore. With the use of $^{18}O_2$ (Figure 2.4A, dotted blue line), the peaks at 845 and 853 cm^{-1} shift to a single peak at 807 cm^{-1}. This shift of 42 cm^{-1} is in agreement with the change predicted for an O-O oscillator by application of Hooke's law, thereby assigning the peaks at 845 and 853 cm^{-1} as a Fermi doublet of ν_{O-O}. Additionally, with use of $^{18}O_2$, the peaks at 465, 475 and 490 cm^{-1} are replaced with peaks at 455 and 484 cm^{-1}. Again, using Hooke's law, we can assign the peaks at 465 and 475 cm^{-1} to a Fermi doublet

representing ν_{Fe-O}, which collapses to a single peak at 455 cm^{-1} upon ^{18}O substitution. The peak at 490 cm^{-1} clearly shifts to lower energy in the ^{18}O isotopomer, but the change of only 6 cm^{-1} and the relative weakness of the signal lead us to suspect that this peak arises from a ligand vibration coupled to the Fe-O stretch.

Repeating this experiment using a mixture of $^{16}O_2$, $^{18}O_2$ and $^{16}O^{18}O$ (Figure 2.4A, dashed green line) allowed us to gain insight into the peroxo binding mode. While the ν_{Fe-O} region is not well resolved, the ν_{O-O} region clearly shows peaks at 806, 829, 845 and 853 cm^{-1}, corresponding to features arising from the ^{18}O-^{18}O, ^{16}O-^{18}O and ^{16}O-^{16}O isotopomers, respectively. The peak at 829 cm^{-1} is assigned to $\nu_{16O-18O}$ by comparison with the spectra obtained from the $^{16}O_2$ and $^{18}O_2$ isotopomers. The appearance of only a single peak between 806 and 845 cm^{-1} with a linewidth comparable to those of the $\nu_{16O-16O}$ and $\nu_{18O-18O}$ peaks indicates that the dioxygen moiety is symmetrically ligated. Three possible symmetric coordination modes are shown in Figure 2.5.

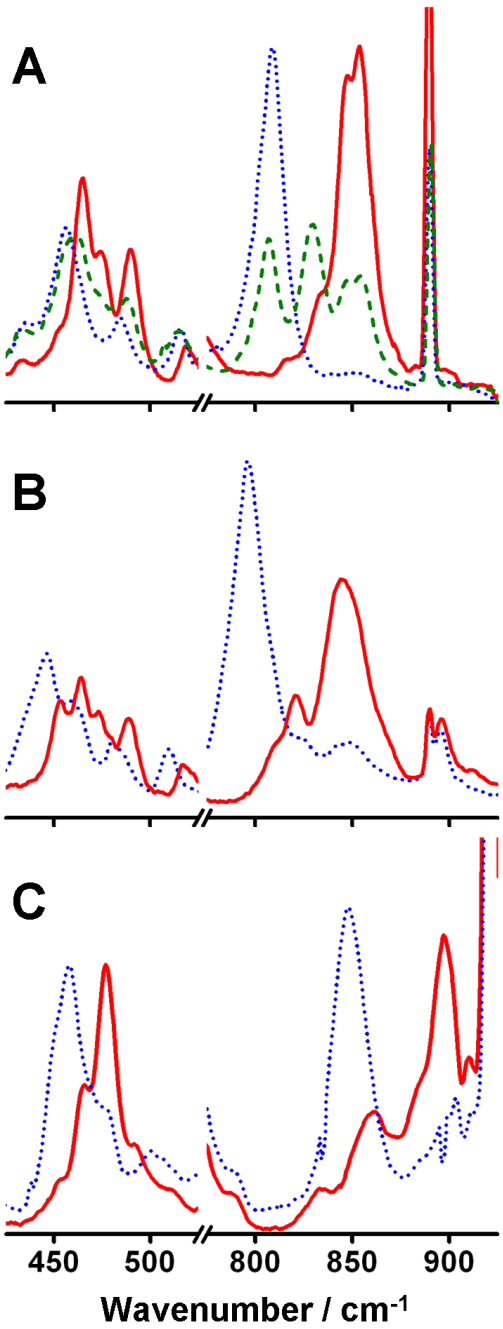

Figure 2.4. Resonance Raman spectra of frozen solutions of **2**•O_2PPh_2 in CH_2Cl_2 (A), **2**•O_2AsMe_2 in CH_2Cl_2 (B) and **3**•O_2PPh_2 in MeCN (C). Solid red = $^{16}O_2$. Dotted blue = $^{18}O_2$. Dashed green = Mixed O_2.

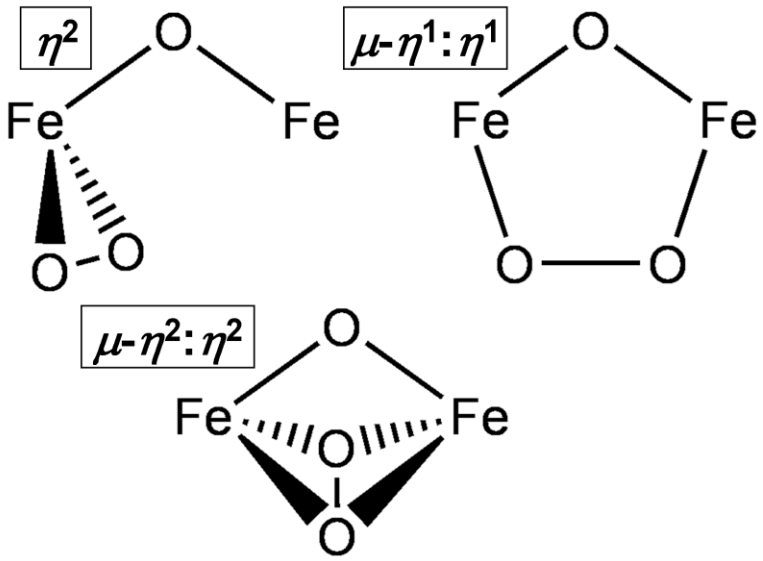

Figure 2.5. Possible O_2 coordination modes in Fe_2O_2-alkoxo core.

The rR spectrum of **3**•O_2PPh_2 generated by using $^{16}O_2$ in MeCN shows peaks at 477 and 897 cm^{-1} (Figure 2.4C, solid red line), corresponding to $\nu_{Fe\text{-}O}$ and $\nu_{O\text{-}O}$, respectively. Using $^{18}O_2$ to generate the sample respectively shifts these peaks to 458 and 848 cm^{-1} (Figure 2.4C, dotted blue line), confirming the assignments. Similar results are obtained for **3**•O_2PPh_2 generated in CH_2Cl_2 (Figure A2.6), but the samples were contaminated with residual **2**•O_2PPh_2 due to incomplete conversion, preventing precise assignment of $\nu_{Fe\text{-}O}$.

Raman spectra of **2**•O_2AsMe_2 (Figure 2.4B) generated in CH_2Cl_2 using either $^{16}O_2$ (solid red line) or $^{18}O_2$ (dotted blue line) reveal peaks assigned to $\nu_{O\text{-}O}$ at 845 and 796 cm^{-1}, respectively. The peak at 464 cm^{-1} in the $^{16}O_2$ spectrum shifts to 443 cm^{-1} upon $^{18}O_2$ substitution and is assigned to $\nu_{Fe\text{-}O}$.

From an examination of the rR data summarized in Table 2.3, we see that $\nu_{O\text{-}O}$ can be used to group the oxygenated intermediates into two categories. Raman shifts near 850 cm^{-1} are characteristic of the first category, which includes the **2**•O_2X species. The second category consists of complexes that exhibit $\nu_{O\text{-}O}$ near 900 cm^{-1} and includes the **3**•O_2X intermediates. In addition to segregating the intermediates, the $\nu_{O\text{-}O}$ values ranging from ~850-900 cm^{-1} demonstrate that all of the species in each group are peroxo complexes.

Table 2.3. Physical properties of **2**•O_2X and **3**•O_2X complexes.

Complex	Solvent	λ_{max} (nm) [ε] (M^{-1} cm^{-1})	$\nu_{O\text{-}O}$ (cm^{-1}) [$^{18}O_2$]	$\nu_{Fe\text{-}O}$ (cm^{-1}) [$^{18}O_2$]	J (cm^{-1})	δ (mm/s)	ΔE_Q (mm/s)	η[f]	Fe···Fe (Å)
2•O_2AsMe$_2$	MeCN	348, 632	845[a]	464[a]					3.27
		[7300, 2100]	[796]	[443]					
2•O_2PPh$_2$	CH_2Cl_2	368, 678	845, 853	465, 475	57 ± 7	0.56(1)	-1.26(2)	0.4	
		[6000, 2100]	[829][b] [807]	[455]					
2•O_2PPh$_2$	MeCN	358, 686	845, 853	465, 476	57 ± 7	0.56(1)	-1.26(2)	0.4	3.25
		[7400, 2200]	[807]	[455]					
2•O_2CPh	CH_2Cl_2	not observed							
3•O_2AsMe$_2$	MeCN	not observed							
3•O_2PPh$_2$[c]	CH_2Cl_2	344, 509, 621	898		60 ± 10	0.56(2)	0.86(5)	~0	
		[7200, 1600, 1800]	[845]			0.54(2)	-0.52(3)	~0	
3•O_2PPh$_2$[d]	MeCN	338, 509, 590	897	477	60 ± 10	0.53(2)	-1.03(4)	~1	3.47
		[8300, 2000, 2300]	[848]	[458]					
3•O_2CPh[e]	CH_2Cl_2	588	900	476					
		[1500]	[850]	[460]					

[a] Measured in CH_2Cl_2.
[b] $\nu_{O\text{-}O}$ from $^{16}O^{18}O$.
[c] Resonance Raman spectroscopy indicates incomplete conversion; some **2**•O_2PPh$_2$ remains, probably red-shifting the peroxo-to-metal charge transfer to 621 nm. In addition, an unknown amount of **3**•O_2PPh$_2$ has decayed to **4**•O_2PPh$_2$, reducing the measured extinction coefficients.
[d] Mössbauer values represent 80% of the total iron.
[e] Values from reference 51.
[f] $\eta = (V_{xx} - V_{yy})/V_{zz}$ is the asymmetry parameter of the electric field gradient tensor.

2.3.4 Mössbauer Spectroscopy

Using Mössbauer spectroscopy, we examined **2**•O_2PPh_2 and **3**•O_2PPh_2 in frozen CH_2Cl_2 and MeCN solutions. Unfortunately, the chlorine atoms of dichloromethane have a very high extinction coefficient at 14.4 KeV and one can therefore not study samples with a pathlength of more than 1 mm. However, freezing a 1-mm thick CH_2Cl_2 solution generates an intolerably uneven sample thickness due to meniscus formation. We found a simple solution to the problem by dripping ca. 80 μl of dichloromethane solution onto a stack of five Fisher-brand paper filter discs stacked into the one-cm-diameter Mössbauer cup. After freezing we obtained homogeneous and firmly packed samples.

Figure 2.6 shows 4.2 K Mössbauer spectra of **2**•O_2PPh_2 (A) and **3**•O_2PPh_2 (B) in CH_2Cl_2 (black hash marks) and MeCN (solid red lines). In both solvents **2**•O_2PPh_2 exhibits one doublet with quadrupole splitting ΔE_Q = 1.26 mm/s and isomer shift δ = 0.56 mm/s. The CH_2Cl_2 sample contains a high-spin iron(II) contaminant (~15%, arrow), most likely belonging to diiron(II) starting material.

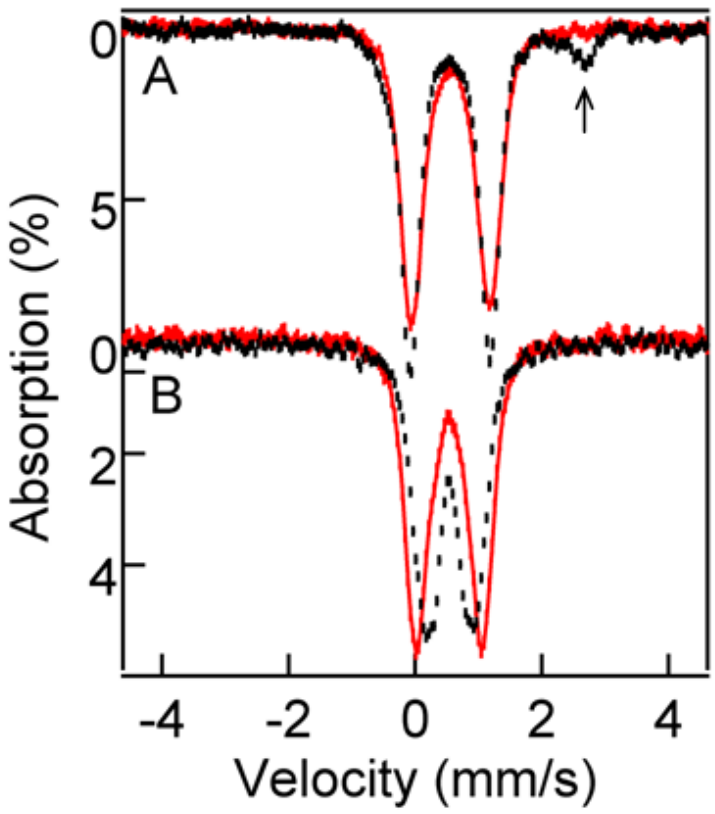

Figure 2.6. 4.2 K zero field spectra of **2**•O_2PPh_2 (panel A) in CH_2Cl_2 (black hash marks) and MeCN (solid red line), and **3**•O_2PPh_2 (panel B) in CH_2Cl_2 (black hash marks) and MeCN (solid red line). The high-energy line of a diiron(II) contaminant is marked by an arrow).

Figure 2.7 shows 8.0 T spectra of **2**•O_2PPh_2 recorded at 4.2 K (A) and 80 K (B,C). The 4.2 K spectrum reveals that the dinuclear complex, as expected, has a ground state with cluster spin S = 0. The variable temperature spectra, taken at 50 K (not shown) and 80 K were analyzed with a spin Hamiltonian appropriate for an exchange coupled dinuclear complex comprising two high-spin ($S_1 = S_2 =$ 5/2) iron(III) ions (Equation 2, where all symbols have their conventional

meanings). For the iron(III) sites considered here, the zero-field splitting parameters $D_{1,2}$ are generally on the order of 1 cm^{-1} and can be neglected.

$$\hat{H} = J\hat{S}_1 \cdot \hat{S}_2 + \sum_{i=1,2} \{\beta \hat{S}_i \cdot \hat{B} + A_o \hat{S}_i \cdot \hat{I}_i - g_n \beta_n \hat{B} \cdot \hat{I}_i + \hat{H}_{Q(i)}\}$$

Eq. (2)

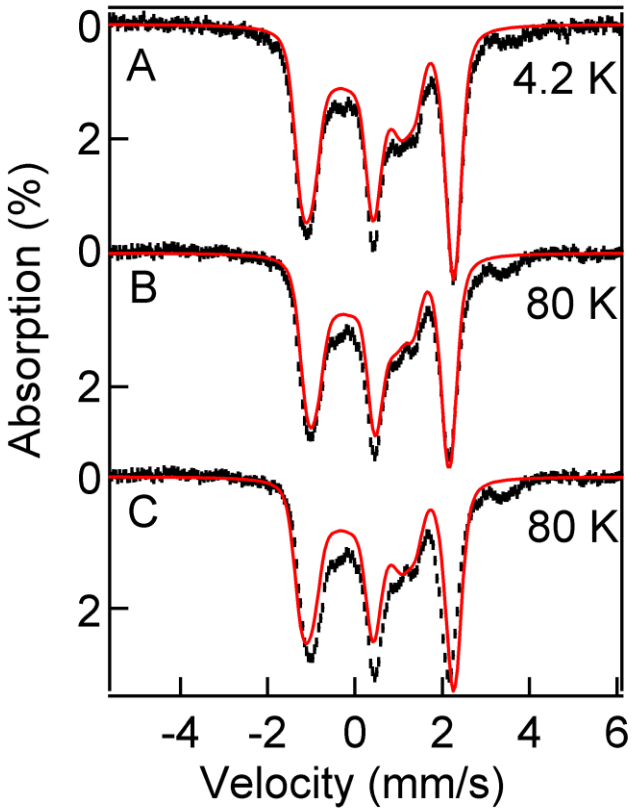

Figure 2.7. 8.0 T Mössbauer spectra of **2**•O_2PPh_2 in CH_2Cl_2 recorded at 4.2 K (A) and 80 K (B). The solid red lines are theoretical curves using the parameters listed in Table 2.3. The data in shown (C) are the same as in (B); the solid red line in (C) is a simulation obtained by assuming (wrongly) that only the S= 0 ground state is occupied at 80 K (2Spin simulation for J = 1000 cm^{-1}). The solid red line in (B) was obtained for J = 57 cm^{-1} (alternatively, one can simulate the spectrum by assuming a state with S = 0 and adjust the applied field to B = 7.35 T).

The determination of *J* by Mössbauer spectroscopy has been described in the literature.[57,58] For an external field B = 8.0 T, applied parallel to the observed γ-rays, one compares the effective field at the iron nuclei, $B_{eff}(i) = B + B_{int}(i)$, at 4.2 K and some higher temperature, say 80 K. At 4.2 K only the S = 0 ground state of the diiron(III) cluster is populated, and thus $B_{eff}(i) = B$. At 80 K higher excited states of the spin ladder can become populated (essentially the S = 1 manifold, $\mathbf{S}_1 + \mathbf{S}_2 = \mathbf{S}$), and in the limit of fast electronic transitions among the thermally populated spin levels, the two iron nuclei experience an internal magnetic field $B_{int}(i) = -\langle S_i \rangle_{th} A_o(i) / g_n \beta_n$, where $\langle S_i \rangle_{th}$ is the thermally averaged expectation value of the spin for site i. For non-heme octahedral sites with N/O coordination we can take $A_o(i) = -21$ T. The expression for B_{int} is quite simple, because zero-field splittings can be ignored and because the magnetic hyperfine interactions of iron(III) sites are generally isotropic. Figure 2.8 shows a plot of $\langle S_{1z} \rangle_{th} = \langle S_{2z} \rangle_{th}$ vs. *J* for B = 8.0 T evaluated at T = 8.0 T.

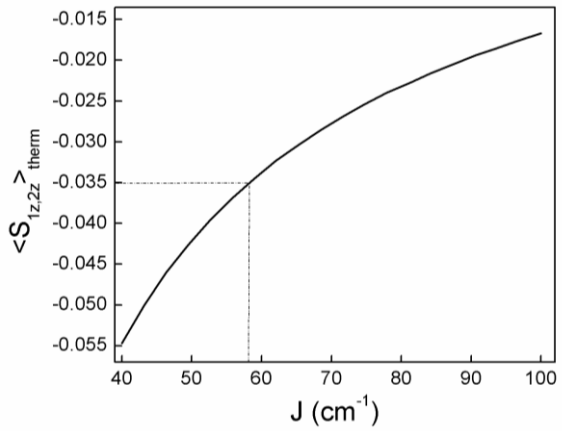

Figure 2.8. Thermally averaged spin expectation values, $\langle S_{1z}\rangle_{th} = \langle S_{2z}\rangle_{th}$, calculated at 80 K for an applied field B = 8.0 T, for an antiferromagnetically coupled dimer comprising two high-spin ($S_1 = S_2 = 5/2$) iron(III) ions for the Hamiltonian $\mathcal{H} = J\mathbf{S}_1\cdot\mathbf{S}_2 + 2\beta(\mathbf{S}_1 + \mathbf{S}_2)\cdot\mathbf{B}$. The zero-field splittings of the iron(III) sites are small and can be ignored.

The solid red line in the 4.2 K spectrum of Figure 2.7A is a simulation assuming that only the S = 0 ground state is populated. The solid red line drawn into the 80 K spectrum of (C) is the same curve as shown in (A). It can be seen that the experimental splitting at 80 K is smaller than expected for a strictly diamagnetic compound. At 80 K the diiron center is magnetically isotropic, and thus B_{int} is antiparallel ($B_{int} < 0$) to the applied field. Simulating the 8.0 T spectrum with an "applied" field of 7.35 T yields the solid red line of Figure 2.7B. Taking A_o = -21 T yields $\langle S_{i,z}\rangle_{th}$ = -0.035 and, thus from the graph of Figure 2.8, a *J*-value slightly smaller than 60 cm^{-1}. Our best simulations using the full Hamiltonian of Eq. 2 (the 2Spin option of WMOSS) yielded $J = (57 \pm 7)$ cm^{-1} for

2•O_2PPh_2, taking also into account an 8.0 T spectrum recorded at 50 K (not shown). The same *J*-value was obtained for **2**•O_2PPh_2 in MeCN**.**

The zero-field spectra of **3**•O_2PPh_2 depend on which solvent is used (Figure 2.6B). The CH_2Cl_2 spectrum is best represented by assuming two doublets of equal intensity with $\delta(1) = 0.56$ and $\delta(2) = 0.58$ mm/s and $\Delta E_Q(1) = 0.86$ and $\Delta E_Q(2) = -0.52$ mm/s. In contrast, the spectrum of the MeCN sample is best represented by one doublet with $\delta = 0.53$ mm/s and $\Delta E_Q = -1.03$ mm/s (representing ~80% of Fe); the remainder may belong to a doublet with $\Delta E_Q \sim -0.90$ mm/s or, alternatively, belong to a distribution of minority species. Analysis of the 8.0 T spectra of **3**•O_2PPh_2 in MeCN, shown in Figure A2.7, again suggests a *J*-value of ~ 60 cm^{-1}, as do the 8.0 T spectra in CH_2Cl_2 (Figure A2.8).

The Mössbauer parameters of each characterized complex are summarized in Table 2.3. We found that within error, the *J* values are almost equivalent across the permutations of species and solvents. The same is true of the isomer shifts. However, the quadrupole splitting values determined for this series of complexes range from -1.26 to 0.86 mm/s and in the case of **3**•O_2PPh_2 in CH_2Cl_2, the presence of two distinct doublets revealed that the two iron atoms in this complex exist in different environments, a property unique to this species/solvent combination.

2.3.5 X-ray Absorption Spectroscopy

To date, intermediates **2**•O_2PPh_2, **3**•O_2PPh_2 and **2**•O_2AsMe_2 have not yielded crystals of sufficient quality for X-ray diffraction characterization. To gain further insight into the structures of these complexes, we resorted to X-ray absorption spectroscopy (XAS), including X-ray absorption near-edge structure (XANES) and X-ray absorption fine structure (EXAFS) analyses. Figure 2.9 shows XANES of **2**•O_2AsMe_2, **2**•O_2PPh_2, and **3**•O_2PPh_2 with parameters shown in Table 2.4. Edge energies (E_0) assigned to the inflection points of these spectra are ~ 7126 eV, higher than the values typical of diiron(III) clusters containing an oxo bridge (~ 7123 – 7124 eV), including diiron(III) peroxo complexes reported by Fiedler *et al*.[29] Westre *et al.* reported that (μ-oxo)diiron(III) complexes have edge energies ~2 eV lower than those found for (μ-hydroxo)diiron(III) complexes.[59] Pre-edge peaks observed at ~ 7114 – 7115 eV in our complexes are typical of diiron(III) clusters.[29,59] It has been shown that an oxo bridge distorts the geometry of a diiron cluster, resulting in a more intense symmetry forbidden 1s $\rightarrow$ 3d transition.[60] Our measured pre-edge areas of ~ 15 – 16 units are smaller than the ~ 20 units (derived by the same standard method developed by Scarrow)[48] found for 6-coordinate (μ-oxo)(μ-peroxo)diiron(III) clusters.[29] It follows that the higher edge energies and smaller pre-edge areas observed in the XANES

parameters of **2**•O_2AsMe_2, **2**•O_2PPh_2, and **3**•O_2PPh_2 are indicative of 6-coordinate diiron(III) complexes without oxo bridges.

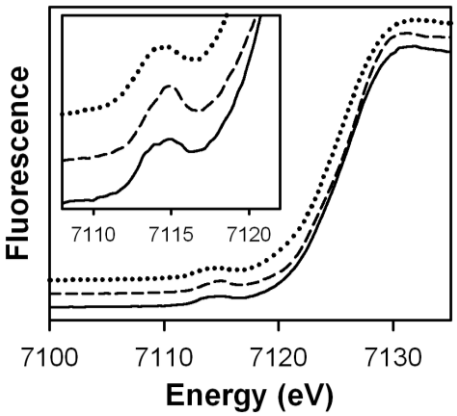

Figure 2.9. Fe K-edge X-ray absorption spectroscopy near edge structures (XANES, fluorescence excitation) of **2**•O_2PPh_2 (top), **2**•O_2AsMe_2 (middle), and **3**•O_2PPh_2 (bottom). Inset: Magnified pre-edge absorption peaks.

Table 2.4. XANES parameters for complexes **2**•O_2PPh_2, **2**•O_2AsMe_2 and **3**•O_2PPh_2.

Complex	**E_0 (eV)**	**$E_{pre\text{-}edge}$ (eV)**	**Pre-edge area**	**Pre-edge width**
2•O_2PPh_2	7126.2	7114.6	15.8(3)	3.84(6)
2•O_2AsMe_2	7125.9	7114.3	15.1(4)	3.66(8)
3•O_2PPh_2	7126.3	7114.7	16.1(2)	3.14(4)

The Fourier-filtered k^3-weighted EXAFS data of **2**•O_2AsMe_2, **2**•O_2PPh_2, and **3**•O_2PPh_2 and their corresponding Fourier transforms are presented in Figure 2.10. Features of **2**•O_2PPh_2 and **2**•O_2AsMe_2 are similar in the range of 2 to 8 $Å^{-1}$, where scattering from low Z atoms is dominant, but different from those of **3**•O_2PPh_2. This suggests that the first two complexes have similar ligand geometries that differ from that of **3**•O_2PPh_2. In the region beyond 8 $Å^{-1}$, EXAFS data of **2**•O_2AsMe_2 and **2**•O_2PPh_2 share similar oscillation phases, but **2**•O_2AsMe_2 exhibits a greater amplitude that most probably derives from a larger contribution from the higher Z arsenic scatterer. Consequently, the Fourier transforms of the **2**•O_2AsMe_2 and **2**•O_2PPh_2 data are very similar with inner shell peaks at r' = 1.6 and r' =2.0 Å and outer shell peaks at r' = 2.3 and r' = 2.8 Å, although the r' = 2.8 Å peak of the **2**•O_2AsMe_2 spectrum is, as expected, much more intense than the corresponding peak observed for **2**•O_2PPh_2.

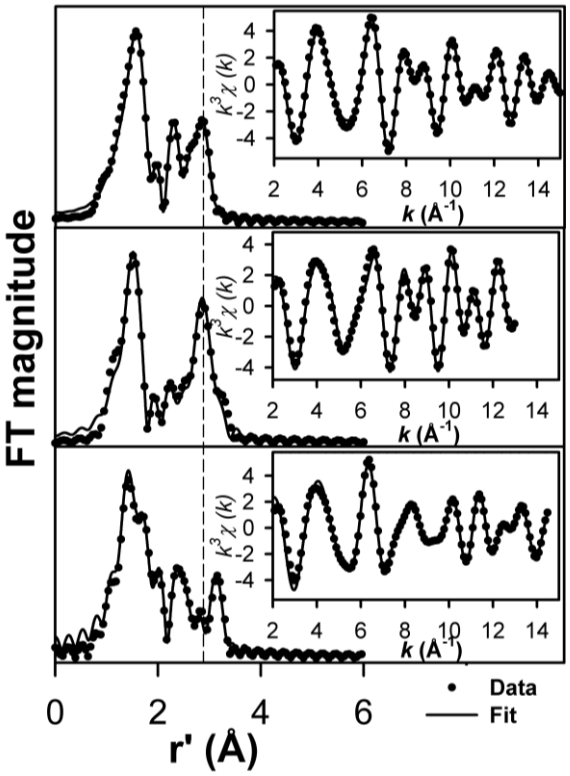

Figure 2.10. Fourier transforms of the Fourier-filtered Fe K-edge EXAFS data $k^3\chi(k)$ (inset) of **2**•O_2PPh_2 (top), **2**•O_2AsMe_2 (middle) and **3**•O_2PPh_2 (bottom). Experimental data displayed with solid circles (•) and fits with solid lines (–). Back-transformation range ~ 0.7 to 3 Å (**2**•O_2PPh_2) and 0.7 – 3.5 Å (**2**•O_2AsMe_2 and **3**•O_2PPh_2). Fourier transformed range, k = 2 to 15 Å^{-1} (**2**•O_2PPh_2), 2 to 13 Å^{-1} (**2**•O_2AsMe_2), and 2 to 14.8 Å^{-1} (**3**•O_2PPh_2). Fit parameters are provided in Tables 2.5 and A2.1 in bold italics.

In the region beyond 8 Å^{-1}, data from **3**•O_2PPh_2 have a different phase and a smaller amplitude than those from **2**•O_2AsMe_2 and **2**•O_2PPh_2. This difference suggests a dissimilar geometry about the iron atoms in **3**•O_2PPh_2 as well as a smaller contribution from high Z atoms. The Fourier transform of the **3**•O_2PPh_2

data shares the same general features as the other two complexes, but with a more complicated inner shell peak near r' = 1.6 Å and an outer shell peak at r' = 3.1 Å instead of a r' = 2.8 Å peak.

Table 2.5 shows some of the progressive fits for the three complexes with the best fits for each species shown in bold italics (see Table A2.1 for all of the fits including all scatterers). The inner shell features of the three complexes can best be fitted with a total coordination number of six with 4 to 5 ligands near 2.0 to 2.2 Å and one ligand near 2.3 Å, corresponding to the Fe-N_{amine} bond as observed in the crystal structures of **1**•O_2PPh_2, **1**•O_2AsMe_2 and $[Fe_2(N\text{-}EtHPTB)(O_2)(OPPh_3)_2]^{3+}$.[22] In **3**•$O_2PPh_2$, a short Fe-O distance of 1.88 Å can be resolved from other Fe-O/N distances and is assigned to the peroxo ligand.[22-24,29] Interestingly, introduction of a ligand at 2.5 Å to the fit of **2**•O_2PPh_2 data improves the fit quality significantly (Fit C, **2**•O_2PPh_2). This same addition does not improve fit qualities for **2**•O_2AsMe_2 and **3**•O_2PPh_2. The r' = 2.3 Å peaks of the three complexes correspond to 3 to 5 Fe···C paths near 2.95 Å, which arise from carbon atoms adjacent to the ligating nitrogen atoms of the benzimidazole rings of the N-EtHPTB ligand.

The r' = 2.8 Å feature of **2**•O_2PPh_2 can be well simulated with an Fe···Fe distance near 3.25 Å. Attempts to simulate this distance with a single Fe···P path or five Fe···C paths respectively resulted in a negative σ^2 value (Fit A, **2**•O_2PPh_2)

or a lower fit quality (Fit B, **2**•O_2PPh_2), indicating that these paths are not responsible for the r' = 2.8 Å peak. However, introducing an Fe···P path at 3.14 Å remarkably improved the fit quality (Fit D, **2**•O_2PPh_2), indicating that a phosphorus atom is present at this distance from the iron atoms in **2**•O_2PPh_2. Similarly, including an Fe···P path at 3.23 Å in addition to an Fe···Fe path at 3.30 Å remarkably improved the fits to the EXAFS data for $[Fe_2(O)(O_2P(OPh)_2)_2(HB(pz)_3)_2]$.[61] The 3.16 Å Fe···P distance found for **2**•O_2PPh_2 is slightly shorter than the average 3.25 Å Fe···P distance seen in the crystal structure of **1**•O_2PPh_2, an observation consistent with the different iron oxidation states of these two complexes.

The intense r' = 2.8 Å peak in **2**•O_2AsMe_2 can be simulated equally well with either a 3.27 Å Fe···Fe path or a 3.21 Å Fe···As path with relatively small σ^2 values (Fits D and E, **2**•O_2AsMe_2). An attempt to replace the Fe···Fe/As paths with six Fe···C paths yielded poor results (compare Fit C to Fits A and B, **2**•O_2AsMe_2). Including both the Fe···Fe and the Fe···As paths does not significantly improve the fit (Fits F and G, **2**•O_2AsMe_2). However, we favor the presence of both the 3.27 Å Fe···Fe and 3.21 Å Fe···As paths given the following reasons: *(i)* **2**•O_2AsMe_2 most likely contains one arsenic and two iron atoms; *(ii)* Fe···As distances of ~ 3.2 to 3.3 Å have been found in related (μ-alkoxo)(μ-1,3-dimethylarsinato)diiron(III) complexes by both X-ray crystallography and

EXAFS;[30,62,63] *(iii)* The phase shift and amplitude associated with iron and arsenic scatterers as simulated by FEFF are very similar in the k-range used for **2**•O_2AsMe_2; therefore, only one path with a small σ^2 value is sufficient to obtain a good simulation of the data (see Figures A2.9 and A2.10 in the appendix for a detailed description). The 3.21 Å Fe···As distance found for **2**•O_2AsMe_2 is slightly shorter than the average 3.28 Å Fe···As distance found in crystal structure of **1**•O_2AsMe_2. As is the case with the Fe···P distances in **1**•O_2PPh_2 and **2**•O_2PPh_2, this difference is consistent with differences in iron oxidation states. That the 3.21 Å Fe···As distance is slightly longer than the 3.16 Å Fe···P distance found for **2**•O_2PPh_2 comes as no surprise, given that arsenic has a greater atomic radius than phosphorus (respectively, 1.15 and 1.00 Å).[64]

The 3.1 Å feature of **3**•O_2PPh_2 is best fitted with an Fe···Fe path at 3.47 Å (Fit A, **3**•O_2PPh_2). Replacing this Fe···Fe path by either one Fe···P path (Fit B, **3**•O_2PPh_2) or five Fe···C paths (Fit C, **3**•O_2PPh_2) results in significantly lower fit quality. Thus, the r' = 3.1 Å feature is attributed to an Fe···Fe path at 3.47 Å. This distance is longer than the Fe···Fe distances found in **2**•O_2PPh_2 and **2**•O_2AsMe_2, consistent with the observed difference in phase shift and the lower amplitude in the k-range of 8 to 13 $Å^{-1}$ for **3**•O_2PPh_2 compared to the other two complexes. Adding half an Fe···P path to Fit A (**3**•O_2PPh_2) only increased fit quality by ~

20% (Fit D, **3**•O_2PPh_2). Therefore, our EXAFS analysis cannot unambiguously establish the presence of a phosphorus atom at this distance from the iron atom.

Table 2.5. Selected EXAFS fitting results for **2**•O_2PPh_2, **2**•O_2AsMe_2, and **3**•O_2PPh_2.[a]

		Fe-O/N			Fe-O/N			Fe-O/N			Fe···C			Fe···X				
Complex	**Fit**	**N**	**R (Å)**	**σ^2**	**N**	**R (Å)**	**σ^2**	**N**	**R (Å)**	**σ^2**	**N**	**R (Å)**	**σ^2**	**N**	**R (Å)**	**σ^2**	**F** [c]	**F'** [d]
2•O_2PPh_2	A	4	1.99	6.14	1	2.29	3.31				5	2.94	10.66	1P	3.12	-0.30	31	93
	B	4	2.00	6.54	1	2.31	3.64				5	2.99	2.19	5C	2.21	2.26	57	314
	C	4	2.00	6.69	1	2.31	2.71	1	2.54	0.58	5	2.99	3.55	1Fe	3.28	3.18	20	48
	D	***4***	***2.00***	***6.57***	***1***	***2.30***	***1.50***	***1***	***2.51***	***3.00***[b]	***5***	***2.96***	***7.95***	***1Fe***	***3.25***	***4.06***	***12***	***20***
														1P	***3.14***	***3.00***[b]		
2•O_2AsMe_2	A	5	1.97	10.82	1	2.25	2.19				3	2.93	3.86	1Fe	3.25	0.98	41	179
	B	5	1.97	10.95	1	2.26	2.85				3	2.90	7.46	1As	3.19	1.94	39	161
	C	5	1.97	10.66	1	2.25	1.03				3	2.95	1.63	6C	3.28	0.40	72	628
	D	***3***	***1.97***	***3.94***	***2***	***2.17***	***4.28***	***1***	***2.35***	***5.35***	***3***	***2.94***	***2.76***	***1Fe***	***3.27***	***1.24***	***16***	***31***
	E	***3***	***1.97***	***3.87***	***2***	***2.17***	***3.82***	***1***	***2.36***	***3.80***	***3***	***2.93***	***5.20***	***1As***	***3.21***	***2.24***	***15***	***31***
	F	3	1.97	3.85	2	2.17	3.89	1	2.35	4.24	3	2.92	3.34	1Fe	3.13	19.43	13	32
														1As	3.21	1.97		
	G	3	1.97	3.84	2	2.17	3.90	1	2.36	4.71	3	2.94	2.22	1Fe	3.27	1.02	13	32
														1As	3.45	12.71		
3•O_2PPh_2	***A***	***4***	***2.04***	***5.73***	***1***	***2.33***	***0.48***	***1***	***1.88***	***1.23***	***4***	***2.95***	***2.39***	***1Fe***	***3.47***	***4.59***	***17***	***25***
	B	4	2.04	5.74	1	2.33	0.52	1	1.88	1.28	4	2.95	2.30	1P	3.61	1.50	26	58
	C	4	2.03	5.73	1	2.33	0.67	1	1.88	1.24	4	2.95	2.63	5C	3.50	2.99	31	83
	D	4	2.04	5.58	1	2.33	0.80	1	1.88	1.12	4	2.95	2.43	1Fe	3.44	3.73	14	20
														0.5P	3.39	0.69		

[a] Resolution ~ 0.12 Å for **2**•O_2PPh_2 and **3**•O_2PPh_2 and ~ 0.14 Å for **2**•O_2AsMe_2; σ^2 = Debye-Waller factor in units of 10^{-3} Å^2.

[b] σ^2 value held fixed during optimization.

[c] F = goodness of fit calculated as $F = \sqrt{\sum k^6(\chi_{exp} - \chi_{cal})^2 / N}$, where N = the number of data points.[50]

[d] F' = F^2/ν, where $\nu = n_{idp} - n_{var}$, n_{idp} is the number of independent points in each data set and n_{var} is the number of variables used in each optimization step. F' is used to indicate the improvement of fit upon the introduction of a shell.[50]

All the peroxo intermediates we have characterized above decay upon warming to room temperature to yellow products **4**•O_2X, which were only characterized by UV-Vis spectroscopy. For these complexes, we suggest a generic formulation of $[Fe_4(N\text{-}EtHPTB)_2(O_2X)_2(\mu\text{-}O)_2]^{4+}$, by analogy to two tetranuclear iron(III) complexes whose crystal structures were reported in 1988.[65] These structures show two $[Fe^{III}_2(HPTB)(O_2CPh)]^{4+}$ units connected by two oxo groups that bridge between one iron(III) of one unit and the corresponding iron in the other unit. This tetranuclear form was also proposed by Feig *et al.* as the end products in their mechanistic studies of the reactions of O_2 with **1**•O_2CPh and two sister complexes.[66] In the absence of crystal structures, we cannot be sure that **4**•O_2PPh_2 and **4**•O_2AsMe_2 exist as tetra-iron species and leave open the possibility that either complex may in fact be dinuclear. We also note that the reported tetranuclear structures may form as a result of crystallization conditions and may not reflect the nature of **4**•O_2X in solution.

2.4 Discussion

A common step in dioxygen activation by biological diiron(II) systems is the formation of (μ-η^1:η^1-peroxo)diiron(III) moieties,[11-18] which are often stable enough to be trapped and characterized. Synthetic (μ-η^1:η^1-peroxo)diiron(III) complexes also exhibit enough stability to allow characterization,[20,27,29-31] and

some in fact have been crystallized.[21-24] For the purpose of examining the factors affecting the stability of this moiety, we synthesized diiron(II) complexes using the dinucleating ligand N-EtHPTB and diphenylphosphinate or dimethylarsinate in lieu of more frequently employed carboxylate bridges. Solutions of these complexes reacted with dioxygen, forming (μ-η^1:η^1-peroxo)diiron(III) moieties, which were examined spectroscopically.

Upon oxygenation, **1**•O_2AsMe_2 forms **2**•O_2AsMe_2, a meta-stable green-blue intermediate, before decaying to the yellow iron(III) end product. **1**•O_2PPh_2 also forms a green-blue intermediate (**2**•O_2PPh_2), but this species converts to a second intermediate (**3**•O_2PPh_2), a deep blue species, before decaying to the yellow end product. This second intermediate is reminiscent of **3**•O_2CPh, the (μ-η^1:η^1-peroxo)diiron(III) intermediate observed upon oxygenation of **1**•O_2CPh.[40] These results bring up three questions: *(i)* What is the nature of **2**•O_2X and **3**•O_2X? *(ii)* How does **2**•O_2X convert to **3**•O_2X? *(iii)* Why are **2**•O_2CPh and **3**•O_2AsMe_2 not observed?

We first address the identities of **2**•O_2PPh_2, **3**•O_2PPh_2 and **2**•O_2AsMe_2, determination of which rests on evidence gathered from a variety of spectroscopic techniques. Because each of these intermediates has a strong chromophore arising from a peroxo LMCT band, resonance Raman (rR) spectroscopy is a good place to start, as it serves as an excellent probe of O-O vibrations. The rR spectra

of these species exhibit features at ~850-900 cm^{-1} that are assigned to $\nu_{O\text{-}O}$ on the basis of isotopic substitution studies. Upon ^{18}O substitution, the frequency downshifts observed for peaks around 850 cm^{-1} in the rR spectra of both **2**•O_2PPh_2 and **2**•O_2AsMe_2 unequivocally indicate the presence of a ligated peroxide moiety. The rR spectrum produced by using an isotopic mixture of O_2 reveals that the peroxide in **2**•O_2PPh_2 is symmetrically ligated. Because its Mössbauer spectrum shows equivalent iron(III) atoms, the peroxide must be ligated to the diiron(III) center in either a μ-η^1:η^1 or a μ-η^2:η^2 configuration. No (μ-η^2:η^2-peroxo)diiron(III) complex has been reported to date, but there are examples of dicopper and heme-copper species containing (μ-η^2:η^2-peroxo)di-metal cores. Figure 2.11 shows a trend wherein the O-O stretch increases in frequency as the peroxide moiety moves from μ-η^2:η^2 to μ-η^1:η^2 to η^2 to μ-η^1:η^1 (Figure 2.11).[4,24,29,51,53-56] Comparing those frequencies to values observed for **2**•O_2PPh_2, **2**•O_2AsMe_2 and **3**•O_2PPh_2 leads us to conclude that the peroxide is ligated in a μ-η^1:η^1 mode in all three complexes, as found in the crystal structure of $[Fe_2(N\text{-}EtHPTB)(O_2)(OPPh_3)_2]^{3+}$.[22] However, the ~50 cm^{-1} disparity observed between the $\nu_{O\text{-}O}$ values of **2**•O_2X and **3**•O_2X raises the interesting question of why they are different.

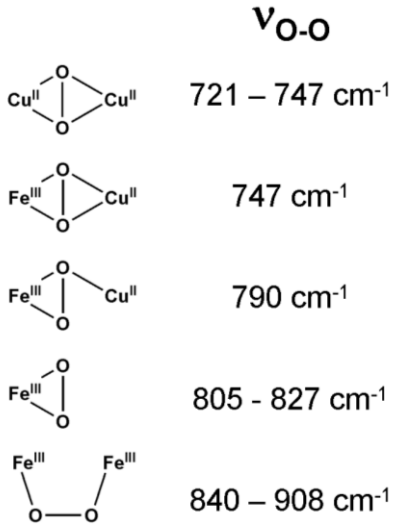

Figure 2.11. Peroxo O-O stretching ranges reported for various dicopper, copper-iron, monoiron and diiron complexes.

One possible explanation for the difference is a change in the Fe···Fe distance. Brunold *et al.* proposed a model for understanding (μ-η^1:η^1-peroxo)diiron(III) units wherein the stretching frequency of the peroxide bond increases due to increased mechanical coupling to the Fe-O stretch as the Fe-O-O angle opens from 90 degrees.[67] Based on this model, it stands to reason that, as the iron centers move apart, the Fe-O-O angle should increase, thus producing a higher frequency $\nu_{O\text{-}O}$.[68] This relationship between $\nu_{O\text{-}O}$ values and Fe···Fe distances is supported by a recent publication showing that an increase in the Fe···Fe distance can be directly correlated to the increase in the stretching frequency of the peroxide bond in a series of $Fe_2(\mu\text{-}\eta^1\text{:}\eta^1\text{-}O_2)(\mu\text{-OR})$ complexes.[29] Applying this correlation to the values of $\nu_{O\text{-}O}$ observed for **2**•O_2PPh_2,

2•O_2AsMe_2 and **3**•O_2PPh_2 generates respective Fe···Fe distances of 3.16, 3.13 and 3.40 Å, values in reasonable agreement with distances of 3.25, 3.27 and 3.47 Å determined from EXAFS analysis.

Based on this information, as well as Mössbauer evidence for equivalent iron atoms in **2**•O_2PPh_2 and the bidentate phosphinate bridge observed in the crystal structure of **1**•O_2PPh_2, we postulate that the diiron(III) center in **2**•O_2PPh_2 is bridged by three groups: the alkoxo oxygen of N-EtHPTB, the 1,2-peroxo moiety and the phosphinate ligand. The structure of **1**•O_2PPh_2 has one open coordination site on each iron atom, both of which are properly positioned to allow dioxygen to coordinate easily in the 1,2-peroxo bridging mode found in **2**•O_2PPh_2 (Scheme 2.1). The parallels observed in the UV-Vis, rR, Mössbauer and EXAFS spectra of **2**•O_2PPh_2 and **2**•O_2AsMe_2 indicate that the latter complex is also triply bridged, with the role of the arsinate moiety analogous to that of the phosphinate moiety in **2**•O_2PPh_2.

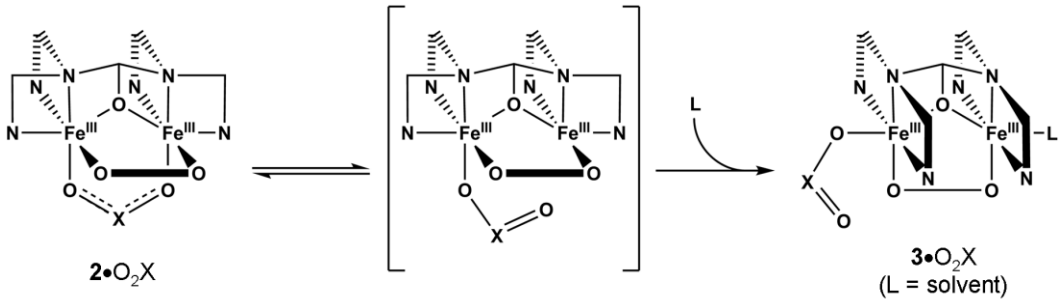

Scheme 2.1. Conversion of **2**•O_2X to **3**•O_2X.

2•O_2PPh_2 is observed to convert to **3**•O_2PPh_2 at temperatures above -40 °C. In this conversion, the phosphinate moiety is proposed to shift to a terminal position on one iron, resulting in the larger inter-iron distance revealed by EXAFS analysis and the increased ν_{O-O} seen in the rR spectrum of **3**•O_2PPh_2. On the basis of similar rR data and similar electronic transitions in the visible range, we propose that **3**•O_2PPh_2 and **3**•O_2CPh share the same basic dibridged structure (Scheme 2.1). A Hammett study of $[Fe_2(N\text{-}EtHPTB)(O_2)(O_2X)]^{2+}$ (O_2X = substituted benzoate) showed a correlation between σ-values of the benzoate substituent and the lifetimes of the peroxo intermediates, with electron withdrawing substituents increasing $t_{½}$.[22] This effect indicates that the benzoate remains coordinated to the diiron(III) unit in a MeCN solution of **3**•O_2CPh at -10 °C. Since this 1996 report, we have noted the similarity of the resonance Raman data from **3**•O_2CPh with those collected after adding $OPPh_3$,[29,51] and deduce that the benzoate moiety in **3**•O_2CPh must occupy a terminal position. While this conclusion is at odds with the bridging configuration proposed by the authors who originally characterized this peroxo complex,[40,51] they had the benefits of neither Brunold and Solomon's mechanical coupling model[67] nor a comparison of the ν_{O-O} values of **3**•O_2CPh and its $OPPh_3$ adduct.[29] The unchanged ν_{O-O} value recorded after $OPPh_3$ ligation indicates that the Fe···Fe distance is comparable in the two complexes. The inter-iron distance of 3.47 Å

measured in **3**•O_2PPh_2 closely matches the inter-iron distance of 3.462 Å reported[22] in the crystal structure of $[Fe_2(N\text{-}EtHPTB)(O_2)(OPPh_3)_2]^{3+}$, suggesting that in **3**•O_2PPh_2, the phosphinate becomes a terminal ligand on one iron, thereby opening up a coordination site on the other (Scheme 2.1). In acetonitrile this site is most likely occupied by solvent, making both iron centers 6-coordinate and indistinguishable by Mössbauer spectroscopy. However, in CH_2Cl_2, the available coordination site cannot be filled by the non-coordinating solvent or the BPh_4 counterion. This produces a complex in which one iron atom is six-coordinate and the other is five-coordinate, a condition reflected by the presence of two quadrupole doublets in the Mössbauer spectrum (Figure 2.6 and Table 2.3).

During conversion from **2**•O_2PPh_2 to **3**•O_2PPh_2 at -30 °C, the peroxo-to-iron(III) charge transfer band blue-shifts 96 nm in MeCN and 57 nm in CH_2Cl_2 (Table 2.3). It is not clear why such large blue-shifts occur. An obvious difference between the proposed structures of **2**•O_2X and **3**•O_2X (Scheme 2.1) is the binding site of the peroxide. In **2**•O_2X, it is *cis* to the N-EtHPTB amine nitrogen atoms, while in **3**•O_2X it is *trans* to those atoms. There is also a difference in the Fe-O-O angles due to different Fe···Fe distances in each intermediate. Because the degree of peroxide and iron orbital mixing affects the energy required for a LMCT, any changes in the iron coordination sphere, especially changes involving the peroxide, can produce changes in the visible

absorbance spectrum. The smaller shift observed in CH_2Cl_2 may be partially accounted for by incomplete conversion to **3**•O_2PPh_2, but we must also consider the presence of one five-coordinate iron center as another factor that can affect the λ_{max} (Scheme 2.1, **3**•O_2X).

The mechanism proposed in Scheme 2.1 would require the N3 ligand set on either end of the 2-hydroxypropane ligand backbone to rearrange from a facial to a meridional configuration during conversion from **2**•O_2PPh_2 to **3**•O_2PPh_2. Our hypothetical structure of **2**•O_2PPh_2 is based on the crystal structure of **1**•O_2PPh_2 (Figure 2.1), which clearly shows an open coordination site on each iron atom *cis* to its respective amine nitrogen. Dioxygen binding to these sites would be expected to be facile, and the resulting peroxo complex would have a geometry similar to that of the simplified cartoon representing **2**•O_2X shown in Scheme 2.1, with the N3 ligand sets configured facially. The proposed structure of **3**•O_2PPh_2 is based on the crystal structure of $[Fe_2(N\text{-}EtHPTB)(O_2)(OPPh_3)_2]^{3+}$, in which both N3 ligand sets of the dinucleating N-EtHPTB ligand adopt meridional configurations and both $OPPh_3$ ligands coordinate *trans* to the alkoxo bridge.[22] In addition to N-ligand rearrangement, conversion of **2**•O_2X to **3**•O_2X also requires the bridging oxyanion in the initial species to move to a terminal position in the second species. Shifting O_2X to a monodentate coordination mode

forms the unobserved species shown in the center of Scheme 2.1, which can revert to **2**•O_2X or irreversibly rearrange to form **3**•O_2X.

In both MeCN and CH_2Cl_2 at -30 °C, we observe significant conversion of **2**•O_2PPh_2 to **3**•O_2PPh_2, indicating that the latter is thermodynamically favored at this temperature. In contrast, no buildup of **3**•O_2AsMe_2 is observed at any temperature, so **2**•O_2AsMe_2 must be the more favored form. In the case of O_2X = benzoate however, the equilibrium shifts in the opposite direction and only **3**•O_2CPh has been reported, and **2**•O_2CPh has not been observed despite the fact that the reaction of **1**•O_2CPh with O_2 has been investigated in various solvents and solvent combinations at low temperatures,[40,51] including one study by stopped-flow methods in propionitrile at -75 °C.[69]

The distinct preferences of the different O_2X moieties for **2**•O_2X versus **3**•O_2X suggest that the nature of the O_2X bridge in **2**•O_2X affects the equilibrium associated with the conversion of **2**•O_2X to **3**•O_2X. Clearly, arsinate favors **2** and benzoate favors **3**, while phosphinate is intermediate between the two. A comparison of the pK_a values of the corresponding conjugate acids (HO_2AsMe_2, 6.27;[70,71] HO_2PPh_2, 2.32;[72] HO_2CPh, 4.19[73]) does not reveal a trend that matches our observations. However, an examination of the respective bite distances of the bridging oxyanions in each of the diiron(II) precursors shows that the lifetime of **2**•O_2X increases with a larger O···O distance (namely 2.23 Å for O_2CPh, 2.56 Å

for O_2PPh_2, and 2.80 Å for O_2AsMe_2, as deduced from the structures of the three **1**•O_2X complexes). We speculate that the bigger O···O bite distance imposes less strain on the bicyclic moiety (Figure 2.12) and results in the more stable, triply-bridged core of **2**•O_2AsMe_2. On the other hand, the smaller bite distance of the benzoate bridge makes it difficult to span an Fe···Fe distance of ca. 3.2 Å expected for **2**•O_2CPh and leads to facile conversion of the benzoate bridge to a terminal ligand and formation of **3**•O_2CPh.

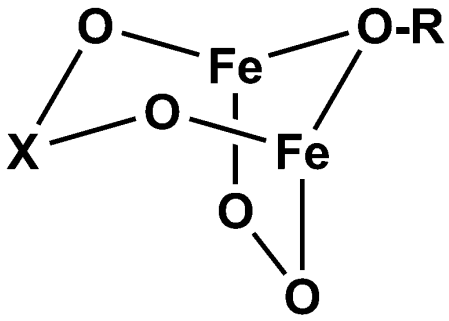

Figure 2.12. Generic representation of the bicyclic diiron core proposed for **2**•O_2X.

This movement of an O_2X ligand from a bridging to a terminal position corresponds to a phenomenon of some importance in diiron enzymes and is referred to as a carboxylate shift.[74] For soluble methane monooxygenase, toluene monooxygenase, and ribonucleotide reductase, one of the conserved glutamate residues (E234, E320, and E328, respectively) of the common diiron active site alternates between terminal and μ-1,1 or μ-1,3 coordination modes in the diiron(III) and diiron(II) forms.[75-79] These carboxylate shifts alter the inter-iron

distance in each active site and may affect the ability of each diiron site to activate O_2. When O_2 is activated, the iron-iron distance can change by as much as 1.5 Å from the diiron(II) starting point to the diiron(IV) state associated with methane oxidizing intermediate **Q**,[3] so the number and the nature of bridging ligands are of vital importance for controlling O_2 bond activation. While this current work does not directly address the question of how to facilitate O-O bond cleavage at a diiron center, it does shed light on the ability of O_2X ligands to tune inter-iron distances by changing coordination modes. We have demonstrated that moving an O_2X ligand from a μ-1,3 to a terminal coordination mode changes the inter-iron distance of an alkoxide-bridged (μ-η^1:η^1-peroxo)diiron(III) complex by ~0.2 Å. This means relatively minor ligand rearrangements can produce substantial changes in inter-iron distances, which in turn, affect the stability of the O-O bond.

In summary, we have synthesized two new diiron(II) complexes and investigated their reaction with oxygen, producing (μ-η^1:η^1-peroxo)diiron(III) species. By varying the central atom of a three-atom chain bridging the iron atoms, we were able to produce and stabilize a peroxo moiety previously unobserved when using N-EtHPTB as a ligand (Scheme 2.1). Under the right conditions, the diphenylphosphinate-bridged form of this peroxo moiety converts to a second peroxo-containing species, akin to other peroxo complexes previously formed using this ligand. Although (μ-η^1:η^1-peroxo)diiron(III) complexes of N-EtHPTB and other ligands have been studied for years, this conversion of one peroxo

species to another is reported here for the first time; we suspect that it takes place upon oxygenation of all previously reported, three-atom bridged, diiron(II) N-EtHPTB complexes, albeit often so rapidly that it has never been observed. We will address this issue in Chapter 3.

2.5 Acknowledgements

This work was supported by the National Institutes of Health through Grants GM-38767 (L.Q.) and EB-001475 (E.M.). We thank Dr. Victor Young, Jr., Benjamin Kucera and Dr. William Brennessel of the X-Ray Crystallographic Laboratory at the University of Minnesota for their invaluable assistance. Mössbauer spectroscopy was undertaken by Dr. Marlène Martinho in the lab of Professor Eckard Münck at Carnegie Mellon University. XAS data were collected and analyzed by Van Van Vu.

2.6 Appendix

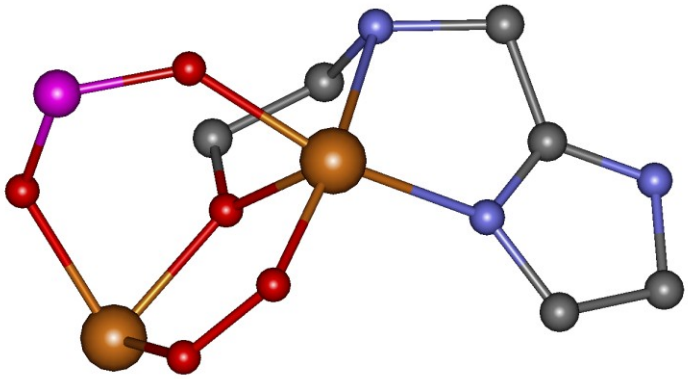

Figure A2.1. FEFF models for **2**•O_2PPh_2 and **2**•O_2AsMe_2, based on combination of crystal structures of **1**•O_2PPh_2, **1**•O_2AsMe_2 and $[Fe_2(N\text{-}EtHPTB)(O_2)(OPPh_3)_2]^{3+}$ (Dong *et al.*)[22] using Accelrys DS Visualizer 1.7 and ChemBio 3D Ultra 11.0. Black = C, Blue = N, Red = O, Brown = Fe, Pink = P/As.

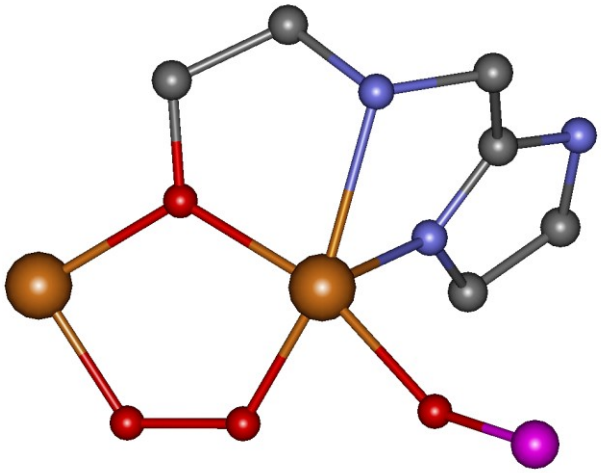

Figure A2.2. FEFF model for **3**•O_2PPh_2, based on crystal structures of $[Fe_2(N\text{-}EtHPTB)(O_2)(OPPh_3)_2]^{3+}$ (Dong *et al.*)[22] using Accelrys DS Visualizer 1.7 and ChemBio 3D Ultra 11.0. Black = C, Blue = N, Red = O, Brown = Fe, Pink = P.

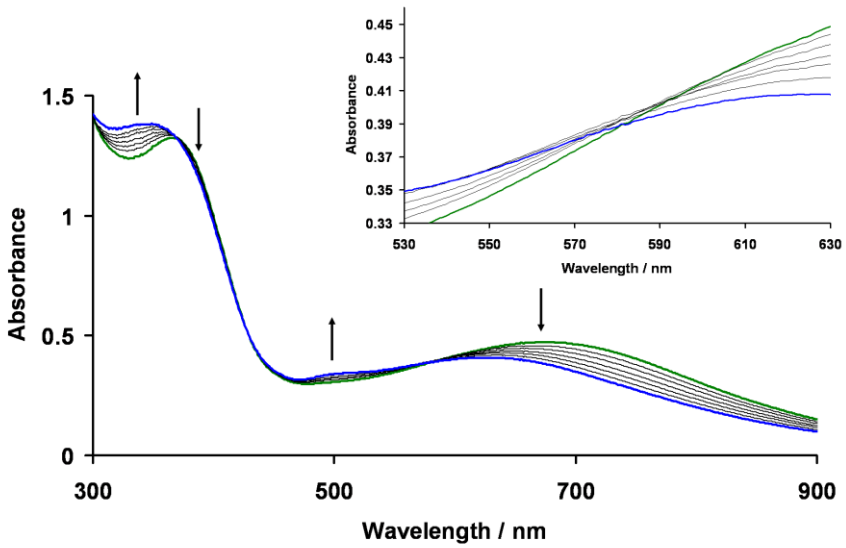

Figure A2.3. Partial conversion of a 0.5 mM solution of **2**•O_2PPh_2 to **3**•O_2PPh_2 in CH_2Cl_2 in a 0.5 cm cuvette at -30 °C. The inset reveals the pseudo-isosbestic point at ~580 nm.

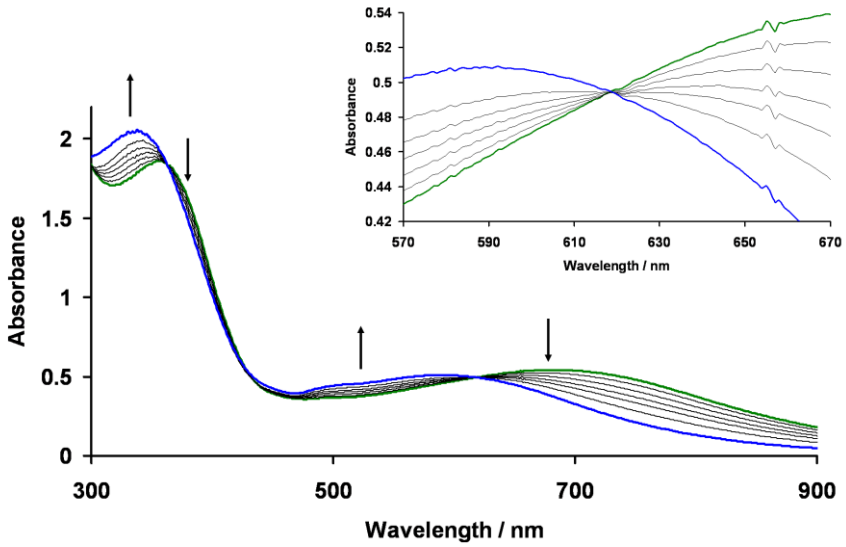

Figure A2.4. Conversion of a 0.5 mM solution of **2**•O_2PPh_2 to **3**•O_2PPh_2 in MeCN in a 0.5 cm cuvette at -30 °C. The inset reveals the isosbestic point at ~620 nm.

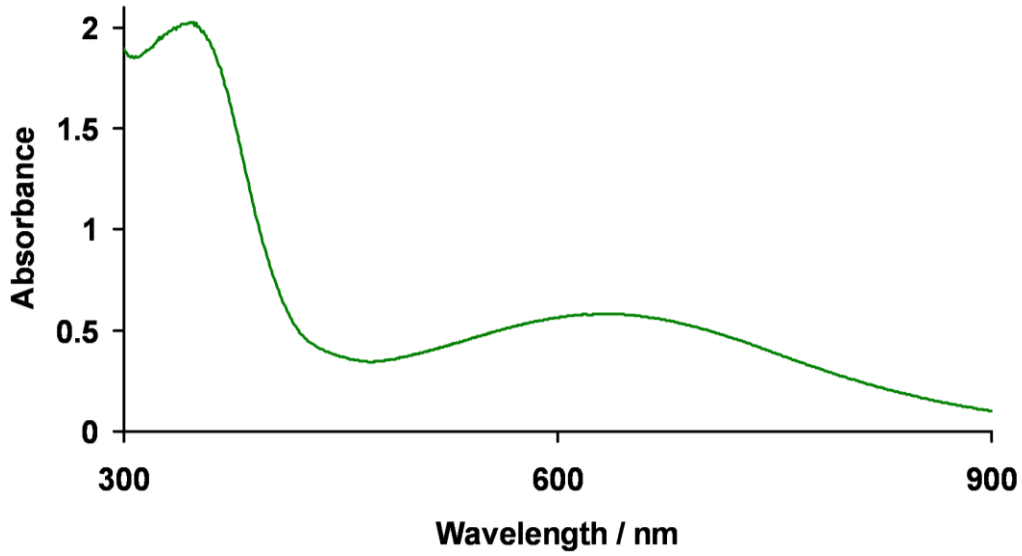

Figure A2.5. UV-Vis spectrum of a 0.5 mM solution of **2**•O_2AsMe_2 in MeCN in a 0.5 cm cuvette at -40 °C.

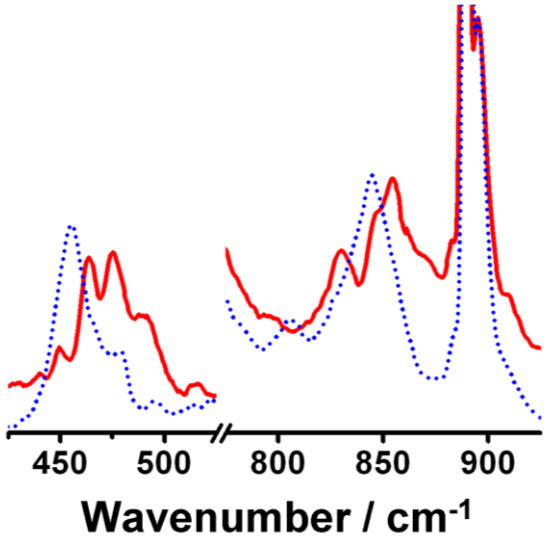

Figure A2.6. Resonance Raman spectra of frozen solutions of **3**•O_2PPh_2 in CH_2Cl_2. Samples are contaminated with **2**•O_2PPh_2. Solid-red = $^{16}O_2$. Dotted-blue = $^{18}O_2$.

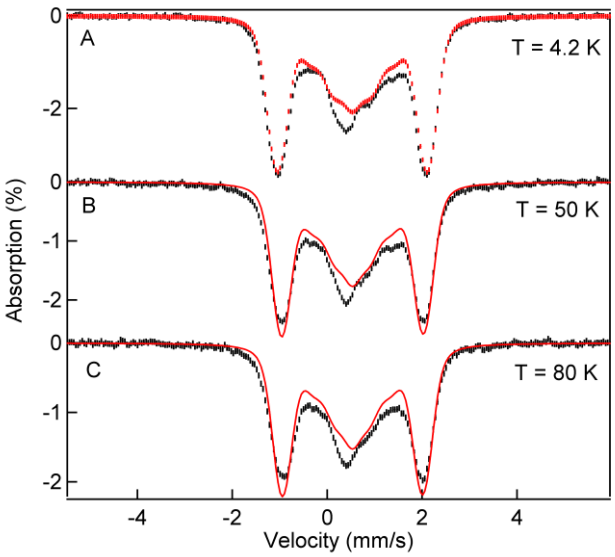

Figure A2.7. 8.0T Mössbauer spectra of **3**•O_2PPh_2 in MeCN recorded at 4.2 K (A) and 50 K (B) and 80 K (C). The solid lines are theoretical curves using the parameters listed in Table 2.3. The solid line in (B) was obtained for J = 60 cm^{-1}.

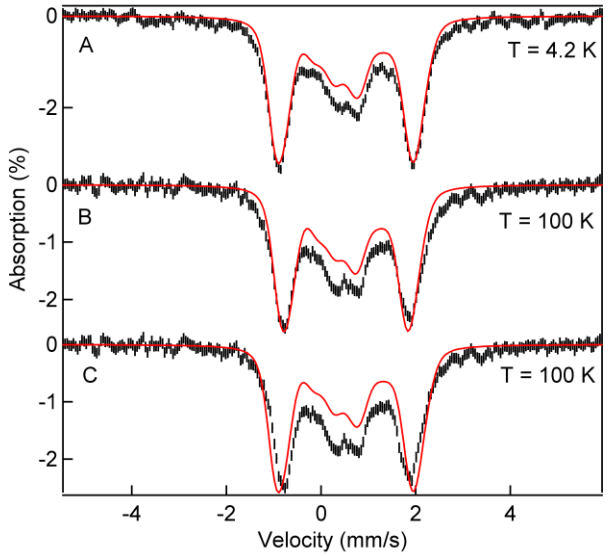

Figure A2.8. 8.0T Mössbauer spectra of **3**•O_2PPh_2 in CH_2Cl_2 recorded at 4.2 K (A) and 100 K (B). The solid lines are theoretical curves using the parameters listed in Table 2.3. The data in (C) are the same as in (B); the solid line in (C) is a simulation obtained by assuming that only the S = 0 ground state is occupied at 100 K, i. e. using J = 1000 cm^{-1}. The solid line in (B) was obtained for J = 60 cm^{-1}.

Table A2.1. EXAFS fitting results for **2**•O_2PPh_2, **2**•O_2AsMe_2, and **3**•O_2PPh_2.[a]

	Fe-O/N			Fe-O/N			Fe-O/N			Fe···C			Fe···X				
Fit	N	R	σ^2	N	R (Å)	σ^2	N	R (Å)	σ^2	N	R	σ^2	N	R (Å)	σ^2	F[c]	F'[d]
1	6	1.97	11.37													1.384	0.117
2	5	2.00	8.64	1	2.30	1.13										1.225	0.104
3	4	2.00	6.23	1	2.29	2.92				5	2.99	1.98				0.799	0.052
4	4	2.00	6.32	1	2.29	2.00				5	2.98	3.84	1Fe	3.27	3.59	0.601	0.035
5	4	1.99	6.14	1	2.29	3.31				5	2.94	10.66	1P	3.12	-0.30	0.488	0.023
6	4	2.00	6.54	1	2.31	3.64				5	2.99	2.19	5C	2.21	2.26	0.662	0.042
7	4	1.99	6.22	1	2.29	2.50				5	2.95	9.28	1Fe	3.24	9.60	0.430	0.022
													1P	3.12	0.00		
8	4	2.00	6.69	1	2.31	2.71	1	2.54	0.58	5	2.99	3.55	1Fe	3.28	3.18	0.392	0.018
9	***4***	***2.00***	***6.57***	***1***	***2.30***	***1.50***	***1***	***2.51***	***3.00***[b]	***5***	***2.96***	***7.95***	***1Fe***	***3.25***	***4.06***	***0.304***	***0.013***
													1P	***3.14***	***3.00***[b]		
																1.517	0.149
1	6	1.94	14.63							3	2.97	-1.00				1.368	0.140
2	5	1.97	10.13	1	2.26	1.35										1.091	0.104
3	5	1.99	10.86	1	2.25	0.12				3	2.93	3.86	1Fe	3.25	0.98	0.611	0.040
4	5	1.97	10.82	1	2.25	2.19				3	2.90	7.46	1As	3.19	1.94	0.595	0.038
5	5	1.97	10.95	1	2.26	2.85				3	2.95	1.63	6C	3.28	0.40	0.809	0.079
6	5	1.97	10.66	1	2.25	1.03											
7	***3***	***1.97***	***3.94***	***2***	***2.17***	***4.28***	***1***	***2.35***	***5.35***	***3***	***2.94***	***2.76***	***1Fe***	***3.27***	***1.24***	***0.381***	***0.018***
8	***3***	***1.97***	***3.87***	***2***	***2.17***	***3.82***	***1***	***2.36***	***3.80***	***3***	***2.93***	***5.20***	***1As***	***3.21***	***2.24***	***0.369***	***0.019***
9	3	1.97	3.85	2	2.17	3.89	1	2.35	4.24	3	2.92	3.34	1Fe	3.13	19.43	0.344	0.022
													1As	3.21	1.97		
10	3	1.97	3.84	2	2.17	3.90	1	2.36	4.71	3	2.94	2.22	1Fe	3.27	1.02	0.316	0.019
													1As	3.45	12.71		
1	6	1.98	14.22													1.200	0.081
2	5	2.00	7.84				1	1.84	1.30							1.143	0.083
3	5	2.00	11.17	1	2.34	0.34										0.976	0.061
4	4	2.03	5.68	1	2.34	1.01	1	1.87	1.16							0.914	0.061
5	4	2.03	5.64	1	2.34	0.42	1	1.88	1.14	4	2.96	2.20				0.568	0.028
6	***4***	***2.04***	***5.73***	***1***	***2.33***	***0.48***	***1***	***1.88***	***1.23***	***4***	***2.95***	***2.39***	***1Fe***	***3.47***	***4.59***	***0.366***	***0.012***
7	4	2.04	5.74	1	2.33	0.52	1	1.88	1.28	4	2.95	2.30	1P	3.61	1.50	0.452	0.018
8	4	2.03	5.73	1	2.33	0.67	1	1.88	1.24	4	2.95	2.63	5C	3.50	2.99	0.494	0.021
9	4	2.04	5.58	1	2.33	0.80	1	1.88	1.12	4	2.95	2.43	1Fe	3.44	3.73	0.332	0.011
													0.5P	3.39	0.69		

[a] Resolution ~ 0.12 Å for **2**•O_2PPh_2 and **3**•O_2PPh_2 and ~ 0.14 Å for **2**•O_2AsMe_2; σ^2 = respective Debye-Waller factor in units of 10^{-3} Å^2.

[b] σ^2 value held fixed during optimization.

[c] F = goodness of fit calculated as $F = \sqrt{\sum k^6(\chi_{exp} - \chi_{cal})^2 / N}$, where N = the number of data points.[50]

[d] F' = F^2/ν, where $\nu = n_{idp} - n_{var}$, n_{idp} is the number of independent points in each data set and n_{var} is the number of variables used in each optimization step. F' is used to indicate the improvement of fit upon the introduction of a shell.[50]

The σ^2 values of the Fe···Fe path (1.24) and the Fe···As path (2.24) in **2**•O_2AsMe_2 (Fits 7 and 8, respectively) are significantly smaller than the σ^2 value of 4.06 found for the Fe···Fe paths in **2**•O_2PPh_2 (Fit 9). Smaller σ^2 leads to larger calculated amplitudes of Fe···Fe or Fe···As peaks in **2**•O_2AsMe_2 as compared to the Fe···Fe path in **2**•O_2PPh_2 (Figure A2.9). In fact, two Fe···Fe/As paths can also lead a good simulation of data in the k-range of 8 to 13 $Å^{-1}$ (Figure A2.10).

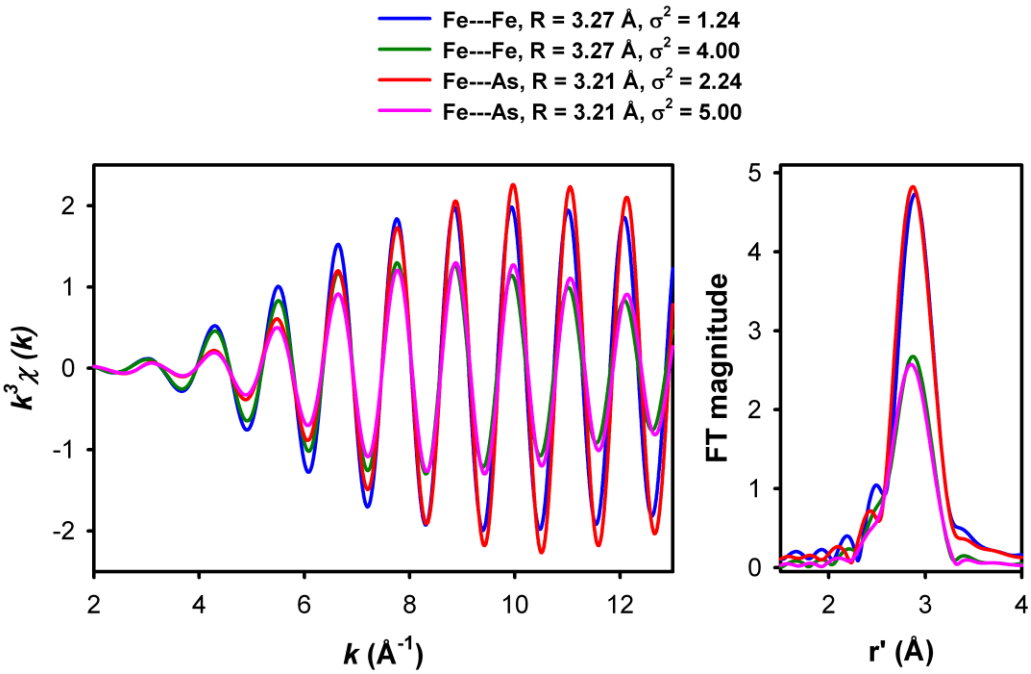

Figure A2.9. Theoretical EXAFS amplitudes and phases and FT amplitudes at different σ^2 values using FEFF84_87[80,81] and Artemis.[82]

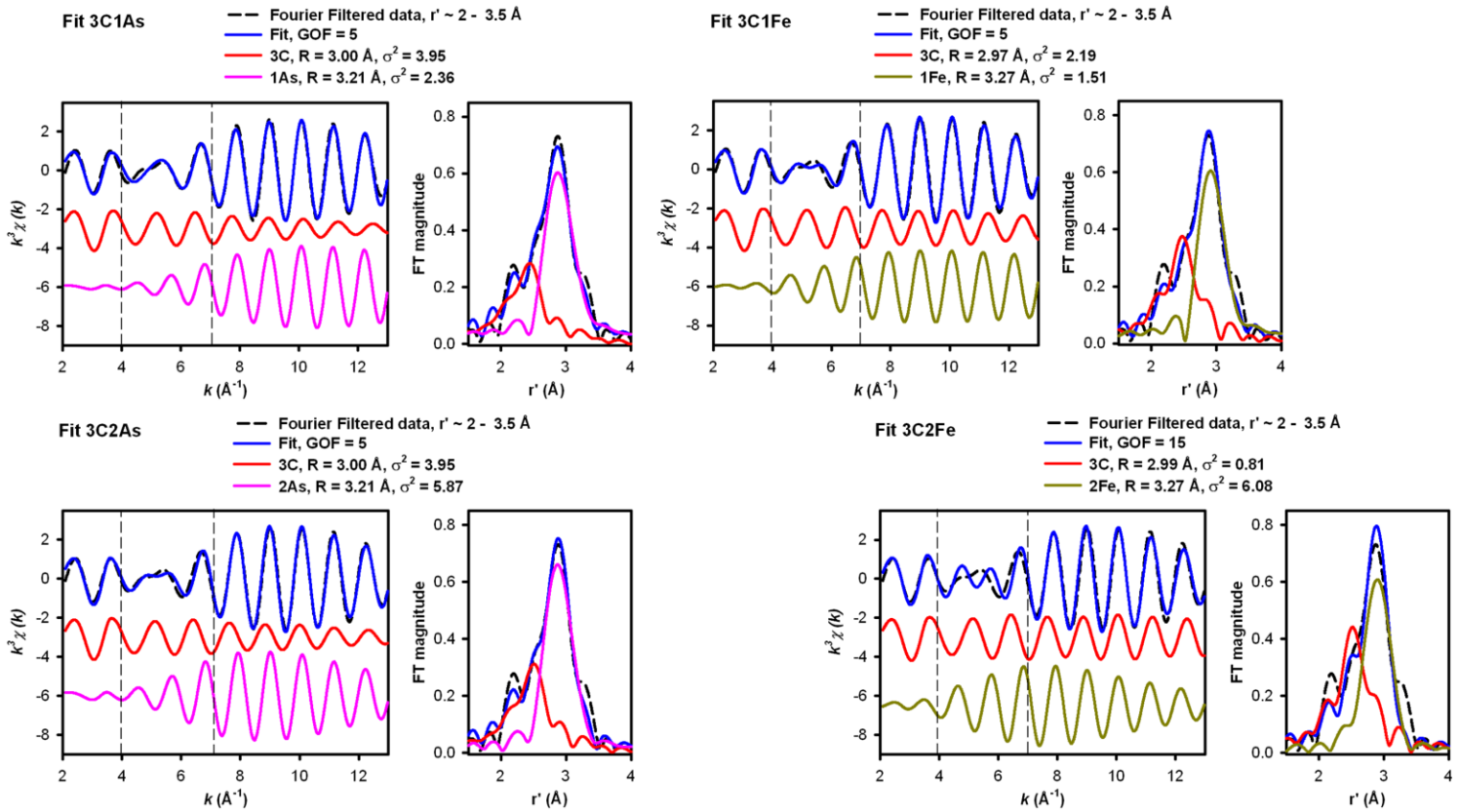

Figure A2.10. Fits to the outer shell with three Fe···C and one (3C1Fe, 3C1As) or two (3C2Fe, 3C2As) Fe···Fe/As paths. Fits 3C1Fe, 3C1As, and 3C2As are equally good. In fit 3C2Fe, the feature corresponding to the high Z scatterers is also well fitted. However, the destructive effect of two Fe···Fe paths on the 3 Fe···C paths in the range of 4 to 7 $Å^{-1}$ results in a lower quality of fit for 3C2Fe.

Chapter 3: Factors Influencing Conversion Kinetics of Triply-Bridged (μ-η^1:η^1-Peroxo)Diiron(III) Intermediates to Doubly-Bridged (μ-η^1:η^1-Peroxo)Diiron(III) Intermediates

3.1 Introduction

Nonheme diiron enzymes have attracted great interest because they perform a wide variety of reactions despite having very similar active sites.[1,3,5-10] For example, soluble methane monooxygenase inserts an oxygen atom into an alkane C-H bond, toluene and *o*-xylene monooxygenases, as well as phenol hydroxylase insert oxygen atoms into aromatic C-H bonds, the R2 subunit of class I ribonucleotide reductases extracts a hydrogen atom producing a stable radical and, as its name implies, stearoyl acyl carrier protein Δ^9-desaturase dehydrogenates a fatty acid hydrocarbon chain. In addition to having similar active site structures, these enzymes all share one other property. The putative catalytic cycles of these enzymes all contain peroxide-bridged diiron(III) complexes formed upon reduction of molecular oxygen. In some cases, these intermediates are stable enough to be trapped and characterized.[11-19] While peroxo-diiron(III) species are endemic in these enzymes, their precise role in catalysis is poorly understood, even though they have been well studied. Synthetic attempts to study peroxo-diiron(III) intermediates have resulted in a variety of biomimetic complexes.[20-29] These compounds often form peroxide-bridged diiron(III) intermediates, especially when stabilized by carboxylate bridges. They are commonly reported as having a (μ-η^1:η^1-peroxo)diiron(III) motif.

In the previous chapter, we discussed how replacing the carboxylate bridges commonly employed in synthesis of these biomimetic complexes affected the behavior of the peroxo intermediates formed. Using the ligand N-EtHPTB (anion of *N,N,N',N'*-tetrakis(2-benzimidazolylmethyl)-2-hydroxy-1,3-diaminopropane) combined with two equivalents of iron(II) and one equivalent of either benzoate, diphenylphosphinate or dimethylarsinate,[40] we demonstrated that two different (μ-η^1:η^1-peroxo)diiron(III) species were formed upon reduction of dioxygen. The benzoate-bridged complex produced a doubly-bridged peroxo intermediate, in contrast to the triply-bridged peroxo intermediate produced by the dimethylarsinate-bridged complex. The diphenylphosphinate-bridged complex was unique in that it formed a triply-bridged peroxo intermediate, which converted to a meta-stable doubly-bridged peroxo intermediate before decaying. We concluded that the nature of the oxyanion bridge (O_2X) strongly influenced the nature and stability of any (μ-η^1:η^1-peroxo)diiron(III) species formed, but we felt further work was required before the effects of bridge differences could be clearly understood. The work in this chapter is intended to address that issue.

This additional work focused on three effects: *(i)* those produced by O_2X O···O bite distance differences, *(ii)* those produced by O_2X electronic differences and *(iii)* those produced by O_2X steric differences. Examination required synthesis of several new diiron(II) complexes (**1**•O_2X) using N-EtHPTB and various O_2X ligands. We found that all of these new species reacted with O_2 in

solution to produce blue-green (μ-η^1:η^1-peroxo)diiron(III) intermediates (**2**•O_2X). With one exception, they then converted to deep-blue (μ-η^1:η^1-peroxo)diiron(III) species (**3**•O_2X) before decaying to yellow products (**4**•O_2X). In most cases, addition of $OPPh_3$ to solutions of **2**•O_2X led to conversion to purple-blue species (**3′**•O_2X) similar to **3**•O_2X. In this paper, we report crystallographic details of three diiron(II) complexes and spectroscopic characterization of a variety of (μ-η^1:η^1-peroxo)diiron(III) intermediates. Implications of O_2X bite distances as well as electronic and steric differences are discussed.

3.2 Experimental Section

3.2.1 Materials and Syntheses

All reagents and solvents were purchased from commercial sources and were used as received, unless noted otherwise. The ligand N-EtHPTB was synthesized using a published procedure.[41] Solvents were dried according to published procedures and distilled under Ar prior to use.[42] The $^{18}O_2$ (97%) used in resonance Raman experiments was purchased from Cambridge Isotope Laboratories, Inc., Andover, MA. Preparation and handling of air sensitive materials were carried out under an inert atmosphere by using either standard Schlenk and vacuum line techniques or a glovebox. Elemental analyses were performed by Atlantic Microlab, Inc., Norcross, GA.

1•O_2CPh, 1•O_2PPh$_2$ and 1•O_2AsMe$_2$ were synthesized using procedures outlined in the previous chapter.

1•O_2PMe$_2$. N-EtHPTB (157 mg, 0.217 mmol) was dissolved in MeOH (~10 mL) along with Et_3N (0.19 mL, 1.4 mmol). Dimethylphosphinic acid (21.6 mg, 0.230 mmol) was added and allowed to dissolve. $Fe(OTf)_2$•2MeCN[43] (189 mg, 0.434 mmol) was added, producing a yellow solution. After 5 minutes, $NaBPh_4$ (149 mg, 0.435 mmol) was added, resulting in immediate precipitation of a white powder. The solid was filtered and dried *in vacuo*. Recrystallization from MeCN and Et_2O produced colorless crystals, some suitable for X-ray diffraction structural analysis. Yield: 153 mg (80%). Anal. for [Fe_2(N-EtHPTB)(O_2PMe$_2$)](BPh_4)(OTf) and calcd for $C_{70}H_{75}BF_3Fe_2N_{10}O_6PS$: C, 60.27; H, 5.42; N, 10.04%. Found: C, 59.82; H, 5.49; N, 10.38%.

1•O_2P(OPh)$_2$. N-EtHPTB (176 mg, 0.243 mmol) was dissolved in MeOH (~10 mL) along with Et3N (0.19 mL, 1.4 mmol). Diphenylphosphoric acid (67.7 mg, 0.271 mmol) was added and allowed to dissolve. $Fe(OTf)_2$•2MeCN (222 mg, 0.509 mmol) was added, producing a yellow solution. After 5 minutes, $NaBPh_4$ (173 mg, 0.506 mmol) was added, resulting in immediate precipitation of a white powder. The solid was filtered and dried *in vacuo*. Recrystallization from MeCN and Et_2O produced milky crystals, some suitable for X-ray diffraction structural analysis. Yield: 331 mg (79%). Anal. for

$[Fe_2(N\text{-}EtHPTB)(O_2P(OPh)_2)](BPh_4)_2$ and calcd for $C_{103}H_{99}B_2Fe_2N_{10}O_5P$: C, 71.87; H, 5.80; N, 8.14%. Found: C, 71.77; H, 5.94; N, 8.41%.

1•O_2CCPh_3. N-EtHPTB (208 mg, 0.288 mmol) was dissolved in MeOH (~10 mL) along with Et3N (0.19 mL, 1.4 mmol). Triphenylacetic acid (83.3 mg, 0.289 mmol) was added and allowed to dissolve. $Fe(OTf)_2$•2MeCN (257 mg, 0.589 mmol) was added, producing a yellow solution. After 5 minutes, $NaBPh_4$ (205 mg, 0.598 mmol) was added, resulting in immediate precipitation of a white powder. The solid was filtered and dried *in vacuo*. Recrystallization from MeCN and Et_2O produced colorless crystals. Yield: 370 mg (73%). Anal. for $[Fe_2(N\text{-}EtHPTB)(O_2CCPh_3)](BPh_4)_2$ and calcd for $C_{111}H_{104}B_2Fe_2N_{10}O_3$: C, 75.78; H, 5.96; N, 7.96%. Found: C, 75.46; H, 5.95; N, 7.96%.

1•O_2CCMe_3. N-EtHPTB (153 mg, 0.212 mmol) was dissolved in MeOH (~10 mL) along with Et_3N (0.19 mL, 1.4 mmol). Trimethylacetic acid (21.7 mg, 0.212 mmol) was added and allowed to dissolve. $Fe(OTf)_2$•2MeCN (186 mg, 0.426 mmol) was added, producing a yellow solution. After 5 minutes, $NaBPh_4$ (152 mg, 0.443 mmol) was added, resulting in immediate precipitation of a white powder. The solid was filtered and dried *in vacuo*. Recrystallization from MeCN and Et_2O produced milky crystals. Yield: 130 mg (50%). Anal. for $[Fe_2(N\text{-}EtHPTB)(O_2CCMe_3)](OTf)_2$ and calcd for $C_{50}H_{58}F_6Fe_2N_{10}O_9S_2$: C, 48.71; H, 4.74; N, 11.36%. Found: C, 48.91; H, 4.77; N, 11.39%.

1•$O_2CC_6H_2$-3,4,5-$(OMe)_3$. N-EtHPTB (72.9 mg, 0.101 mmol) was dissolved in MeOH (~10 mL) along with Et_3N (0.077 mL, 0.56 mmol). 3,4,5-Trimethoxybenzoic acid (21.4 mg, 0.101 mmol) was added and allowed to dissolve. $Fe(OTf)_2$•2MeCN (94.2 mg, 0.216 mmol) was added, producing a yellow solution. After 5 minutes, $NaBPh_4$ (87.2 mg, 0.255 mmol) was added, resulting in immediate precipitation of a pale yellow powder. The solid was filtered and dried *in vacuo*. Recrystallization from MeCN and Et_2O produced yellow crystals, some suitable for X-ray diffraction structural analysis. Yield: 116 mg (74%). Anal. for $[Fe_2$(N-EtHPTB)$(O_2CCH_2$-3,4,5-$(OMe)_3)](BPh_4)(OTf)$ and calcd for $C_{78}H_{80}BF_3Fe_2N_{10}O_9S$: C, 61.92; H, 5.33; N, 9.26%. Found: C, 62.14; H, 5.55; N, 8.94%.

1•$O_2CC_6H_3$-3,4-$(OMe)_2$. N-EtHPTB (100.0 mg, 0.138 mmol) was dissolved in MeOH (~10 mL) along with Et_3N (0.097 mL, 0.69 mmol). 3,4-Dimethoxybenzoic acid (25.1 mg, 0.138 mmol) was added and allowed to dissolve. $Fe(OTf)_2$•2MeCN (120.3 mg, 0.276 mmol) was added, producing a yellow solution. After 5 minutes, $NaBPh_4$ (196.5 mg, 0.574 mmol) was added, resulting in immediate precipitation of a pale yellow powder. The solid was filtered and dried *in vacuo*. Recrystallization from MeCN and Et_2O produced milky crystals. Yield: 162 mg (89%). Anal. for $[Fe_2$(N-EtHPTB)($O_2CC_6H_3$-3,4-$(OMe)_2)](OTf)_2$ and calcd for $C_{54}H_{58}F_6Fe_2N_{10}O_{11}S_2$: C, 49.40; H, 4.45; N, 10.67%. Found: C, 49.65; H, 4.44; N, 10.39%.

1•$O_2CC_6H_3$-3,5-$(OMe)_2$. N-EtHPTB (146.1 mg, 0.202 mmol) was dissolved in MeOH (~10 mL) along with Et_3N (0.142 mL, 1.02 mmol). 3,5-Dimethoxybenzoic acid (37.0 mg, 0.203 mmol) was added and allowed to dissolve. $Fe(OTf)_2$•2MeCN (187.8 mg, 0.431 mmol) was added, producing a yellow solution. After 5 minutes, $NaBPh_4$ (190.6 mg, 0.557 mmol) was added, resulting in immediate precipitation of a pale green-yellow powder. The solid was filtered and dried *in vacuo*. Recrystallization from MeCN and Et_2O produced pale yellow crystals. Yield: 238.5 mg (80%). Anal. for [Fe_2(N-EtHPTB)($O_2CC_6H_3$-3,5-$(OMe)_2$)](BPh_4)$(OTf)_2$ and calcd for $C_{77}H_{78}BF_3Fe_2N_{10}O_8S$: C, 62.36; H, 5.30; N, 9.44%. Found: C, 62.56; H, 5.11; N, 9.33%.

1•$O_2CC_6H_4$-4-OMe. N-EtHPTB (149.2 mg, 0.206 mmol) was dissolved in MeOH (~10 mL) along with Et_3N (0.144 mL, 1.03 mmol). 4-Methoxybenzoic acid (31.3 mg, 0.206 mmol) was added and allowed to dissolve. $Fe(OTf)_2$•2MeCN (189.2 mg, 0.433 mmol) was added, producing a yellow solution. After 5 minutes, $NaBPh_4$ (205.4 mg, 0.600 mmol) was added, resulting in immediate precipitation of a pale green-yellow powder. The solid was filtered and dried *in vacuo*. Recrystallization from MeCN and Et_2O produced milky crystals. Yield: 245.4 mg (93%). Anal. for [Fe_2(N-EtHPTB)($O_2CC_6H_4$-4-OMe)]$(OTf)_2$ and calcd for $C_{53}H_{56}F_6Fe_2N_{10}O_{10}S_2$: C, 49.62; H, 4.40; N, 10.92%. Found: C, 49.41; H, 4.51; N, 11.08%.

3.2.2 Physical Methods

UV-Vis spectra were recorded on a Hewlett-Packard 8453 diode array spectrophotometer equipped with an Unisoku Scientific Instruments cryostat (Osaka, Japan). Resonance Raman spectra were collected on an ACTON AM-506M3 monochromator with a Princeton LN/CCD data collection system using a Spectra-Physics Model 2060 krypton laser. Low-temperature spectra of the peroxo intermediates in CH_2Cl_2 and MeCN were obtained at 77 K using a 135° backscattering geometry. Samples were frozen onto a gold-plated copper cold finger in thermal contact with a Dewar flask containing liquid nitrogen. Raman frequencies were referenced to the features of indene. Slits were set for a band-pass of 4 cm^{-1} for all spectra.

X-ray Crystallography. X-ray diffraction data were collected on a Bruker SMART platform CCD diffractometer at 173(2) K.[44] Preliminary sets of cell constants were calculated from reflections harvested from three sets of 20 frames. These initial sets of frames were oriented such that orthogonal wedges of reciprocal space were surveyed. The data collection was carried out using MoKα radiation (graphite monochromator). Randomly oriented regions of reciprocal space were surveyed to the extent of one sphere and to a resolution of 0.84 Å. The intensity data were corrected for absorption and decay using SADABS.[45] Final cell constants were calculated after integration with SAINT.[46] The structures were solved and refined using SHELXL-97.[47] The space groups $P2_1/c$,

$P2_1/n$ and P-1 were determined based on systematic absences and intensity statistics. Direct-methods solutions were calculated which provided most non-hydrogen atoms from the E-map. Full-matrix least squares / difference Fourier cycles were performed which located the remaining non-hydrogen atoms. All non-hydrogen atoms were refined with anisotropic displacement parameters. All hydrogen atoms were placed in ideal positions and refined as riding atoms with relative isotropic displacement parameters. The SQUEEZE function of the program PLATON[83] was used to remove 143 effective electrons in diffuse scattering from a volume of 1555.2 $Å^3$ per cell of **1**•$O_2P(OPh)_2(BPh_4)_2$•MeCN and 120 effective electrons in diffuse scattering from a volume of 1097.4 $Å^3$ per cell of (**1**•$O_2CC_6H_2$-3,4,5-$(OMe)_3)_2(BPh_4)_2(OTf)_2$•2MeCN. Brief crystal data and intensity collection parameters for the crystalline complexes are shown in Table 3.1.

3.3 Results

3.3.1 X-ray Crystallography

For this chapter, we synthesized diiron(II) complexes using a variety of O_2X ligands. We were able to crystallographically characterize three of these **1**•O_2X compounds (O_2X = O_2PMe_2, $O_2P(OPh)_2$ and $O_2CC_6H_2$-3,4,5-$(OMe)_3$) and compare the results with structural analysis from Chapter 2 (Table 3.2). Both the old and the new compounds contain two distorted trigonal-bipyramidal iron(II) centers, with amine nitrogen atoms and oxygen atoms from the bridging moiety in

the axial positions. The equatorial sites are occupied by two benzimidazole nitrogen atoms and the alkoxide oxygen atom (Figure 3.1). With few exceptions, the respective atoms in the first coordination sphere of each complex reflect approximately equal interatomic distances and angles. Differences of note include average τ values,[52] O_2X bite distances, O-X-O angles and interiron distances. The τ values can be grouped into two sets with $\tau_{ave} \sim 0.8$ (O_2X = O_2AsMe_2, O_2PPh_2 and O_2PMe_2) and $\tau_{ave} \sim 0.9$ (O_2X = $O_2P(OPh)_2$, $O_2CC_6H_2$-3,4,5-$(OMe)_3$ and O_2CPh). Comparing bite distances of all complexes, we see O···O distances of ~2.55 Å (X = P) and ~2.23 Å (X = C). The lone X = As complex is in a class of its own with a bite distance of ~2.80 Å. It is also apparent that the O-X-O angle varies with the identity of the X atom (X = As, 113.26 deg.; X = P, 115.17 to 119.47 deg.; X = C, 123.4 to 124.2 deg.). The O-X-O angle measurement correlates negatively with O_2X bite distance; the species with the longest O···O distance (**1**•O_2AsMe_2) has the sharpest O-X-O angle while the X = C complexes have the shortest bite distances and greatest O-X-O angles and the X = P compounds fall in between these extremes. This apparent discrepancy is explained by variations in X-O bond lengths (As-O_{ave} = 1.676 Å; P-O_{ave} = 1.501Å; C-O_{ave} = 1.261 Å). Even though the O-X-O angle decreases, concomitant lengthening of the X-O bonds results in a greater O···O distance.

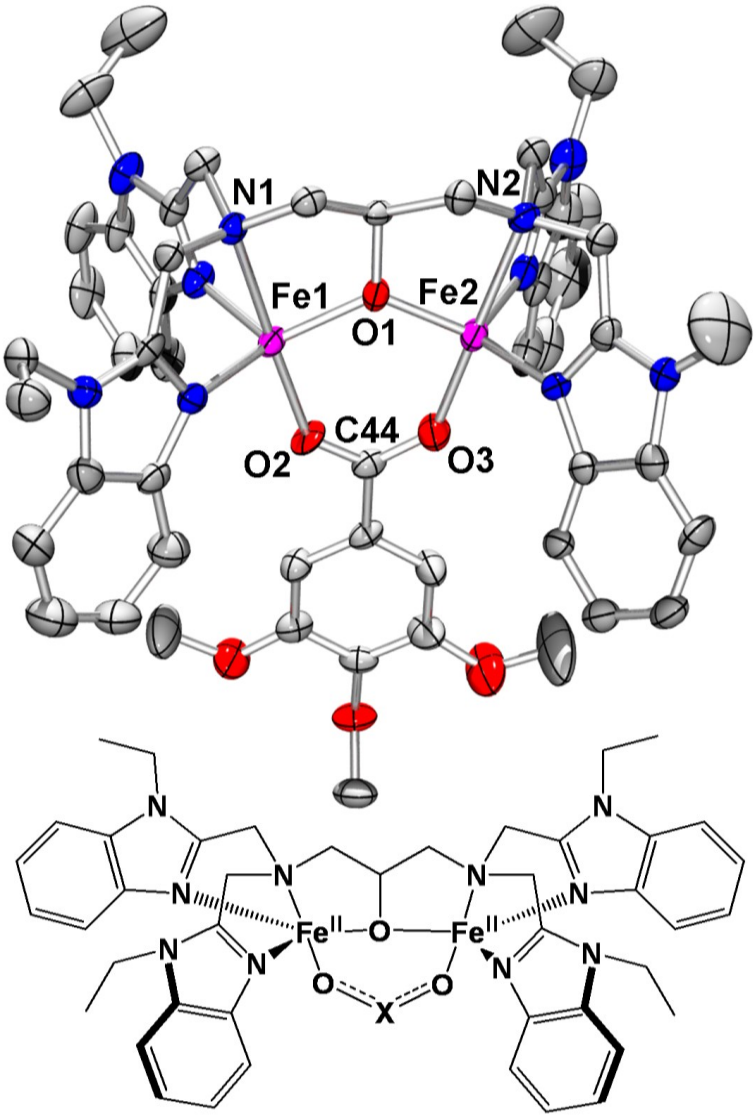

Figure 3.1. Crystal structure of the cation **1**•$O_2CC_6H_2$-3,4,5-$(OMe)_3$ (50% ellipsoids) with hydrogen atoms removed. Generic cartoon of **1**•O_2X: O_2X = O_2AsMe_2 (**1**•O_2AsMe_2), O_2PPh_2 (**1**•O_2PPh_2), O_2PMe_2 (**1**•O_2PMe_2), $O_2P(OPh)_2$ (**1**•$O_2P(OPh)_2$), $O_2CC_6H_2$-3,4,5-$(OMe)_3$ (**1**•$O_2CC_6H_2$-3,4,5-$(OMe)_3$), O_2CPh (**1**•O_2CPh).

For the most part, increasing the bite distance increases the Fe···Fe distance. However, there are two exceptions: *(i)* **1**•O_2AsMe_2 has an O···O distance ~0.24 Å longer than any other complex, although its interiron distance is within 0.01 Å of those found in both **1**•O_2PPh_2 and **1**•O_2PMe_2. *(ii)* **1**•$O_2P(OPh)_2$ has an O···O distance on par with **1**•O_2PPh_2 and **1**•O_2PMe_2, yet its interiron distance (3.6211 Å) is the greatest of all the compounds, exceeding the distances found in **1**•O_2AsMe_2 (3.5357 Å) and the two other X = P species (3.5405 and 3.5364 Å) by ~0.08 Å. This is greater than the ~0.06 Å difference observed between the Fe···Fe distances of the X = C complexes (3.4879 and 3.4749 Å) and those with Fe···Fe distances of ~3.54 Å. The unusually long Fe···Fe distance in **1**•$O_2P(OPh)_2$ is most likely not due to packing effects, because a similar interiron distance of 3.649 Å was reported when **1**•$O_2P(OPh)_2$ crystallized in a different space group (*P* -1) with different anions (ClO_4).[31]

There are two crystallographically interesting observations regarding the compounds we report here and those in the previous chapter. First, we note that [Fe_2(N-EtHPTB)(O_2PMe_2)](BPh_4)(OTf)(MeCN) and [Fe_2(N-EtHPTB)(O_2AsMe_2)](BPh_4)(OTf)(MeCN) are crystallographically isostructural. Both fall into space group $P2_1/c$ with $Z = 4$ and share virtually identical unit cells with respective values for *a*, *b* and *c* of 16.0709(9) vs. 16.1151(12), 15.6360(9) vs. 15.7370(12) and 28.4703(15) vs. 28.473(2) Å. The α and γ angles are exactly 90

degrees and the β angles are respectively 103.5800(10) and 103.4900(10) degrees. The respective cations, anions and solvent molecules in each unit cell lie in essentially the same positions with the same orientations. The minor variations in unit cell parameters and atom positions arise from differences around the X atom of the O_2X bridging moieties. Small angle changes around X as well as X-C and X-O bond length variations produce minor differences in the cations which slightly alter the position of every other atom in the unit cell due to packing effects. The second observation is that the unit cell containing the cation $[Fe_2(N\text{-}EtHPTB)(O_2CC_6H_2\text{-}3,4,5\text{-}(OMe)_3)]^{2+}$ also contains a pseudo-inversion center lying between cations (Figure 3.2). This effectively doubles the number of unique elements per unit cell, thus doubling the size of the unit cell. The cation "inversion" is reasonably true, but the anions are farther away from the pseudo-inversion center, resulting in greater distortion during "inversion". Because the differences between the cations are not significant, we chose to focus on one cation rather than redundantly discussing what essentially amounts to duplicate cations.

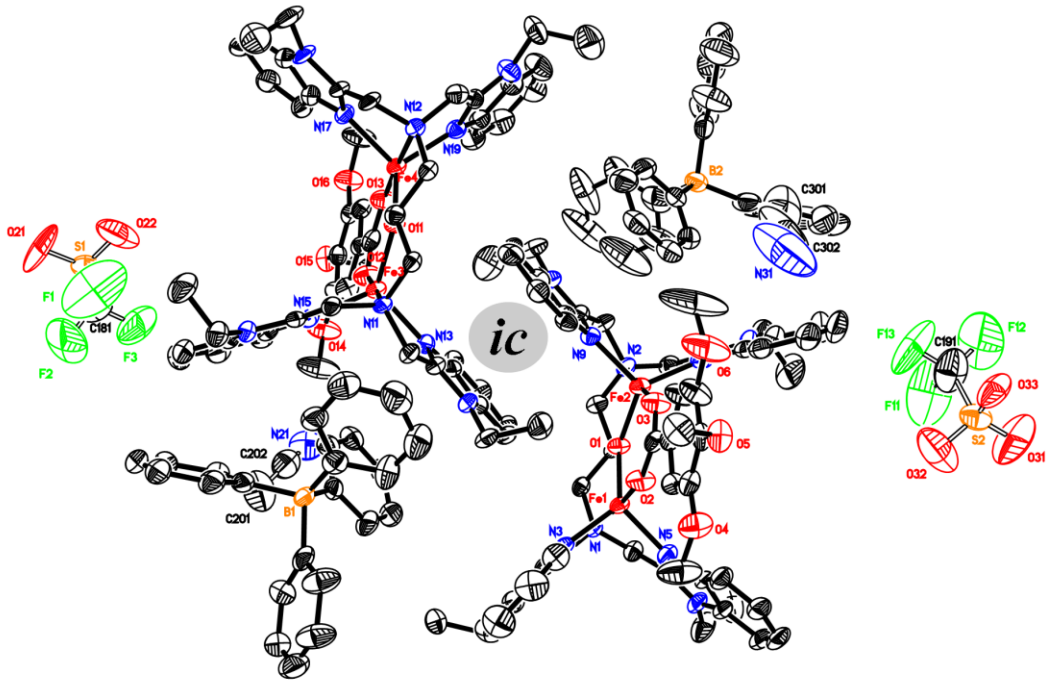

Figure 3.2. ORTEP diagram (50% ellipsoids) of the unit cell containing two molecules of $[Fe_2(N\text{-}EtHPTB)(O_2CC_6H_2\text{-}3,4,5\text{-}(OMe)_3)]^{2+}$ and accompanying anions and solvent molecules (hydrogen atoms removed for clarity). There is a pseudo-inversion center (*ic*) between the cations. Comparing the cations, we find that the "inversion" is almost true, whereas comparing the BPh_4 ions reveals differences in thermal ellipsoid size and minor differences in atom locations, indicating that the inversion center is not real.

Table 3.1. Crystal data and structure refinement for **1**•$O_2PMe_2(BPh_4)(OTf)$•MeCN, **1**•$O_2P(OPh)_2(BPh_4)_2$•MeCN, and (**1**•$O_2CC_6H_2$-3,4,5-$(OMe)_3)_2(BPh_4)_2(OTf)_2$•2MeCN.

	1•$O_2PMe_2(BPh_4)(OTf)$•MeCN	**1**•$O_2P(OPh)_2(BPh_4)_2$•MeCN	(**1**•$O_2CC_6H_2$-3,4,5-$(OMe)_3)_2(BPh_4)_2(OTf)_2$•2MeCN
empirical formula	$C_{72}H_{78}BF_3Fe_2N_{11}O_6PS$	$C_{105}H_{102}B_2Fe_2N_{11}O_5P$	$C_{160}H_{166}B_2F_6Fe_4N_{22}O_{18}S_2$
fw	1435.99	1762.27	3108.29
T (K)	173(2)	173(2)	173(2)
Mo Kα λ, Å	0.71073	0.71073	0.71073
space group	$P2_1/c$	$P2_1/n$	P -1
a (Å)	16.0709(9)	23.063(4)	12.576(4)
b (Å)	15.6360(9)	18.942(4)	19.153(7)
c (Å)	28.4703(15)	23.888(4)	36.053(12)
α (deg)	90	90	96.743(5)
β (deg)	103.5800(10)	99.205(3)	92.147(5)
γ (deg)	90	90	103.100(5)
V (Å^3)	6954.1(7)	10301(3)	8381(5)
Z	4	4	2
ρ (calc), Mg/m^3	1.372	1.136	1.232
abs coeff (mm^{-1})	0.539	0.352	0.437
R1[a]	0.0398	0.0446	0.0713
wR2[b]	0.0984	0.1271	0.1955

[a] $R1 = \Sigma||F_o|-|F_c|| / \Sigma|F_o|$. [b] $wR2 = [\Sigma[w(F_o^2-F_c^2)^2] / \Sigma [w(F_o^2)^2]]^{1/2}$.

Table 3.2. Selected interatom distances and bond angles for $[Fe_2(N\text{-}EtHPTB)(O_2X)]^{2+}$.

	1•O_2AsMe_2	**1**•O_2PPh_2	**1**•O_2PMe_2	**1**•$O_2P(OPh)_2$	**1**•$O_2CC_6H_2$-3,4,5-$(OMe)_3$ [a]	**1**•O_2CPh
τ_{ave}	0.81	0.77	0.82	0.91	0.89	0.93
Interatom distances (Å)						
Fe1-O1	2.0145(13)	2.004(2)	2.0184(18)	2.0057(16)	1.967(3)	1.976(5)
Fe2-O1	2.0037(14)	1.992(2)	1.9995(18)	2.0031(15)	1.970(3)	1.964(5)
Fe1-N1	2.3366(16)	2.294(3)	2.323(2)	2.3141(18)	2.328(4)	2.316(6)
Fe2-N2	2.3892(16)	2.352(3)	2.372(2)	2.309(2)	2.314(4)	2.280(7)
Fe1-O2	1.9825(14)	2.008(2)	2.0037(19)	2.0562(16)	2.036(3)	2.057(5)
Fe2-O3	1.9863(14)	2.021(2)	2.0123(18)	2.0506(16)	2.025(3)	2.019(6)
Fe1-N3	2.1372(17)	2.086(3)	2.105(2)	2.0668(19)	2.045(4)	2.064(6)
Fe1-N5	2.1023(18)	2.115(3)	2.127(2)	2.0732(19)	2.046(4)	2.069(6)
Fe2-N7	2.1088(17)	2.075(3)	2.098(2)	2.0551(19)	2.063(4)	2.080(6)
Fe2-N9	2.0759(17)	2.098(3)	2.080(2)	2.075(2)	2.044(4)	2.064(6)
As1/P1/C44-O2	1.6740(15)	1.514(2)	1.509(2)	1.4762(17)	1.254(5)	1.264(9)
As1/P1/C44-O3	1.6776(14)	1.512(2)	1.517(2)	1.4784(18)	1.273(5)	1.253(9)
Fe1···Fe2	3.5357(5)	3.5405(10)	3.5364(6)	3.6211(7)	3.4879(13)	3.4749(31)
O2···O3	2.7991(21)	2.5600(32)	2.5545(28)	2.5520(24)	2.2253(46)	2.2251(74)
Bond angles (degrees)						
Fe1-O1-Fe2	123.27(6)	124.76(11)	123.32(9)	129.19(8)	124.73(15)	123.8(2)
O1-Fe1-O2	105.77(6)	105.55(9)	102.50(8)	98.99(6)	98.27(13)	98.6(2)
O1-Fe2-O3	107.92(6)	99.44(9)	103.98(8)	98.93(7)	100.51(13)	101.5(2)
Fe1-O2-As1/P1/C44	127.24(8)	132.01(14)	131.47(12)	133.92(11)	138.1(3)	136.4(5)
Fe2-O3-As1/P1/C44	128.15(8)	138.88(15)	132.54(12)	133.24(10)	134.7(3)	133.9(5)
O2-As1/P1/C44-O3	113.26(7)	115.59(13)	115.17(12)	119.47(10)	123.4(4)	124.2(7)

[a] The unit cell of this compound contains virtual twins of **1**•$O_2CC_6H_2$-3,4,5-$(OMe)_3$ produced through a pseudo-inversion center. As there is no substantive difference between the two cations, values listed here are taken from a single cation.

3.3.2 UV-Vis Spectroscopy

Upon reaction with O_2, the virtually colorless solutions of **1**•O_2X produce blue-green peroxo intermediates (**2**•O_2X). In most cases, **2**•O_2X converts to a second, deep blue peroxo intermediate (**3**•O_2X) before decaying to the final product, a yellow species (**4**•O_2X). The peroxide LMCT bands of **2**•O_2X and **3**•O_2X lie in two distinct regions of the visible spectrum with λ_{max} of **2**•O_2X red-shifted ~50-100 nm from that of **3**•O_2X, which are all between 590 and 600 nm. These spectral differences make UV-Vis absorption spectroscopy an excellent tool for following the transition from the first peroxo complex to the second. Dichloromethane solutions of **1**•O_2X were reacted with O_2 via the simple expedient of bubbling cooled gas through an aliquot. The subsequent formation of blue-green **2**•O_2X and conversion to deep blue **3**•O_2X were recorded at temperatures as low as -90 °C (Figures A3.1-A3.4), showing that carboxylate bridged complexes do indeed form two peroxo intermediates, as can be clearly seen in the spectra produced upon oxygenation of **1**•O_2CCPh$_3$ (Figure 3.3). Spectra recorded at this low temperature revealed that the reaction with oxygen of the well-studied complex **1**•O_2CPh[40,51,69] (Figure 3.4) also produces two peroxo species, although they are not as spectroscopically distinct as those of **2**•O_2CCPh$_3$ and **3**•O_2CCPh$_3$. Spectral changes (Table 3.3) were used to calculate first-order rate constants (Table 3.4) for conversion of **2**•O_2X to **3**•O_2X. At -90 °C,

conversion of **2**•O_2PPh_2 to **3**•O_2PPh_2 does not occur. For this reason, we raised the temperature to -40 °C, although even at this temperature, we never observed clean conversion to **3**•O_2PPh_2 in CH_2Cl_2. As we noted in the previous chapter, **2**•O_2AsMe_2 does not produce appreciable concentrations of **3**•O_2AsMe_2 at any temperature.[84] In this study, we found the same to be true of **2**•O_2PMe_2.

Table 3.3. UV-Vis spectroscopic characteristics of **2**•O_2X, **3**•O_2X and **3′**•O_2X.

O_2X	λ_{max} (nm), [ε] (M^{-1} cm^{-1})		
	2•O_2X	**3**•O_2X	**3′**•O_2X
O_2AsMe_2	632 [2100]	-- [b]	-- [c]
O_2PMe_2	--	-- [b]	616 [2400]
O_2PPh_2	678 [2100]	621 [1800]	592 [2600]
$O_2P(OPh)_2$	680 [2800]	576 [3100]	594 [3600]
O_2CCPh_3	708 [2500]	630 [2200]	595 [3300]
O_2CCMe_3	706 [--] [d]	580 [3100]	577 [3800]
O_2CPh	704 [--] [d]	588 [1500] [e]	592 [2300]
$O_2CC_6H_2$-3,4,5-$(OMe)_3$	707 [2600]	590 [3200]	592 [4300]
$O_2CC_6H_3$-3,4-$(OMe)_2$	704 [--] [d]	578 [6200]	590 [5300]
$O_2CC_6H_3$-3,5-$(OMe)_2$	706 [--] [d]	588 [5400]	592 [5600]
$O_2CC_6H_4$-4-OMe	705 [--] [d]	580 [3000]	590 [4000]

[a] In MeCN.
[b] Conversion to **3**•O_2X did not take place at any temperature.
[c] Conversion to **3′**•O_2X did not take place at any temperature even with addition of 100 equivalents of $OPPh_3$.
[d] **2**•O_2X begins converting to **3**•O_2X before complete formation of **2**•O_2X, so ε was not determined.
[e] Values from ref. 51.

Table 3.4. pK_a values for HO_2X and first order k_{obs} values for conversion of **2**•O_2X to **3**•O_2X and **2**•O_2X to **3′**•O_2X.

O_2X	pK_a of HO_2X	**2 to 3** [a] k_{obs} (s^{-1})	**2 to 3′** [b] k_{obs} (s^{-1})
O_2AsMe_2	6.27	-- [c]	-- [d]
O_2PMe_2	3.08 [e]	-- [c]	1.8(4)E-4 [f]
O_2PPh_2	2.32 [e]	3.1E-4 [g]	4.3(4)E-3 [f]
$O_2P(OPh)_2$	1.85 [e]	1.2(1)E-4	3.1(1)E-2
O_2CCPh_3	3.96	1.7(2)E-3	0.026(3)
O_2CCMe_3	5.03	1.8(1)E-2	0.080(3)
O_2CPh	4.19	5.3(1)E-2	-- [h]
$O_2CC_6H_2$-3,4,5-$(OMe)_3$	4.24	4.2(6)E-4	0.13(5)
$O_2CC_6H_3$-3,4-$(OMe)_2$	4.36	6.6(9)E-4	0.12(1)
$O_2CC_6H_3$-3,5-$(OMe)_2$	3.97	4.8(2)E-3	0.20(1)
$O_2CC_6H_4$-4-OMe	4.50	4.7(4)E-3	0.12(1)

[a] All rates measured at -90 °C in CH_2Cl_2 except for O_2AsMe_2 (not observed)[c], O_2PMe_2 (not observed)[c] and O_2PPh_2 (-40 °C).[f]

[b] All rates measured after addition of 20 equivalents of $OPPh_3$ at -90 °C in CH_2Cl_2 except for O_2AsMe_2 (not observed)[d], O_2PMe_2 (-40 °C)[f] and O_2PPh_2 (-40 °C).[f]

[c] Conversion to **3**•O_2X did not take place at any temperature.

[d] Conversion to **3′**•O_2X did not take place at any temperature even with addition of 100 equivalents of $OPPh_3$.

[e] Value determined in 7% ethanol solution (Ref. 72).

[f] $OPPh_3$ added (20 eq.) at -40 °C.

[g] Calculated from $OPPh_3$ concentration dependence study (Figure A3.5).

[h] By the time enough **2**•O_2CPh had formed to allow for addition of $OPPh_3$, significant quantities of **3**•O_2CPh were already present in solution, preventing accurate rate determination for the conversion of **2**•O_2CPh to **3′**•O_2CPh.

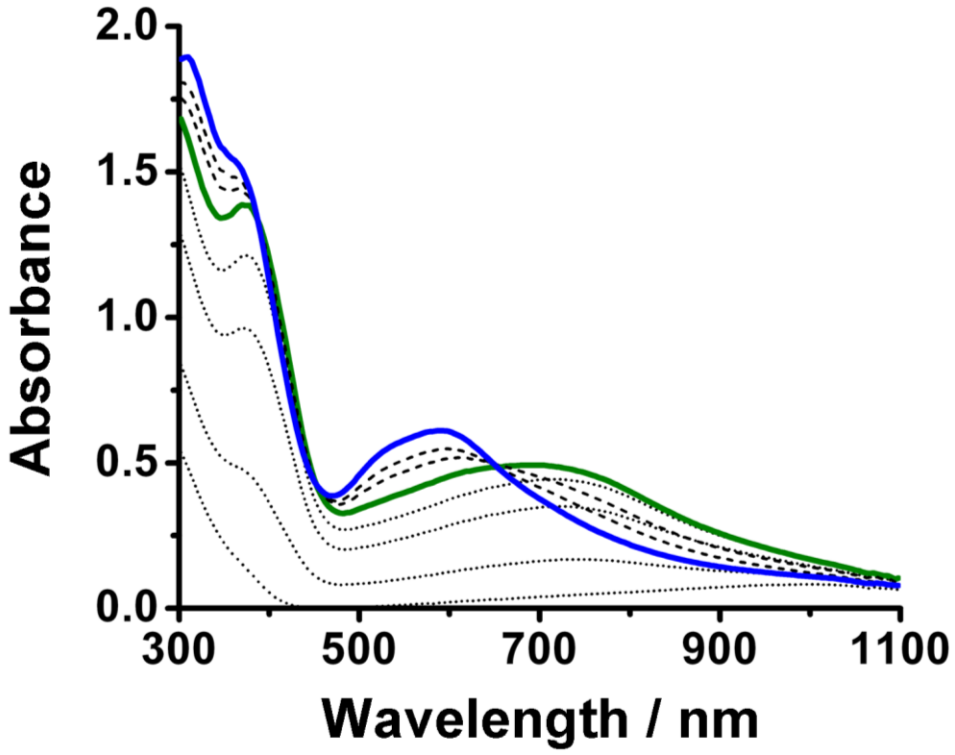

Figure 3.3. Selected UV-Vis spectra showing formation of **2**•O_2CCPh_3 (solid green line) and subsequent conversion to **3**•O_2CCPh_3 (solid blue line). Dotted lines indicate appearance of **2**•O_2CCPh_3, dashed lines indicate conversion to **3**•O_2CCPh_3.

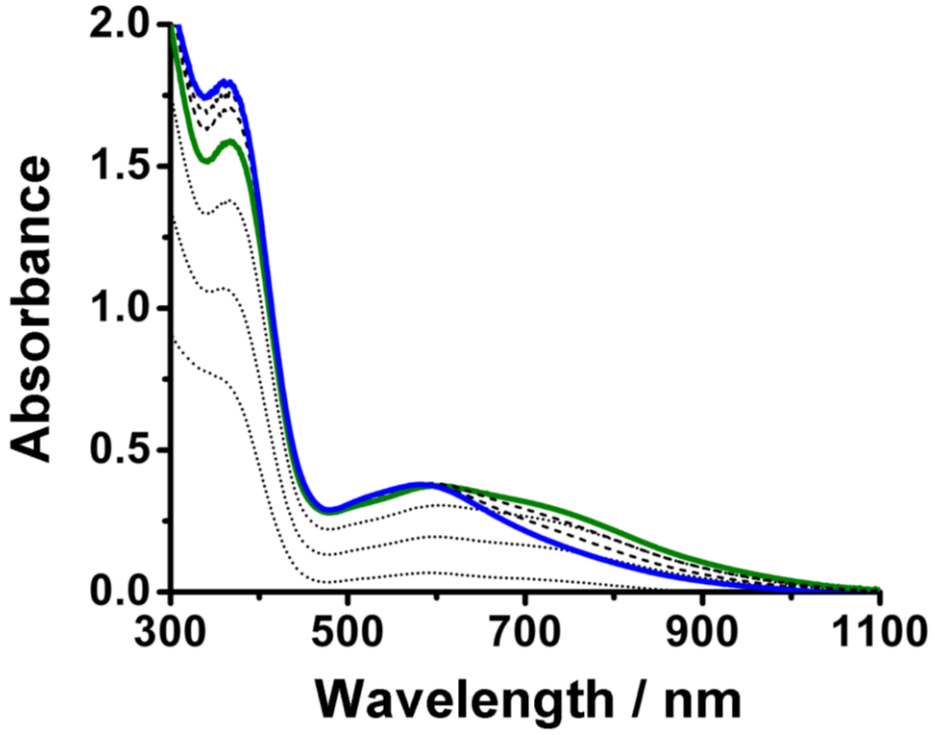

Figure 3.4. Selected UV-Vis spectra showing formation of **2**•O_2CPh (solid green line) and subsequent conversion to **3**•O_2CPh (solid blue line). Dotted lines indicate appearance of **2**•O_2CPh, dashed lines indicate conversion to **3**•O_2CPh.

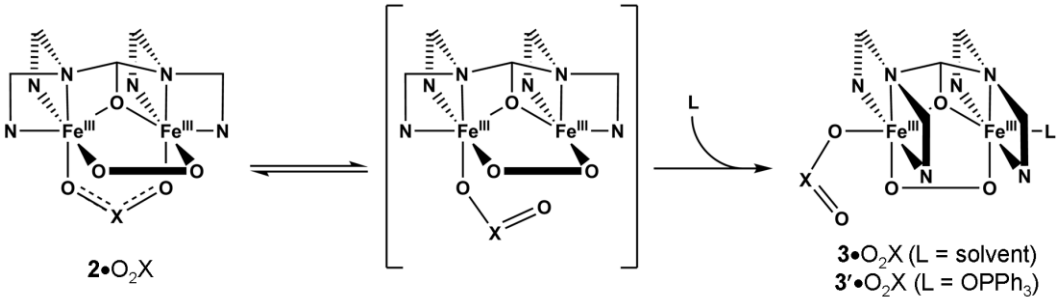

Scheme 3.1. Conversion of **2**•O_2X to **3**•O_2X or **3′**•O_2X.

In the last chapter, we postulated that the conversion of **2**•O_2X to **3**•O_2X in acetonitrile involves a change in O_2X binding mode from bridging to terminal

and coordination of a solvent molecule in position L (Scheme 3.1). For this work we added $OPPh_3$ to solutions of **2**•O_2X in hopes of substituting it into the L position. Upon $OPPh_3$ addition, purple-blue species (**3′**•O_2X) indeed form that exhibit λ_{max} at wavelengths near each respective **3**•O_2X, although the extinction coefficients of the new intermediates are higher than those observed for each respective **3**•O_2X (Table 3.3) with the exception of the $O_2CC_6H_3$-3,4-$(OMe)_2$-based species. While facile conversion to **3′**•O_2X from most **2**•O_2X intermediates was accomplished by adding 20 equivalents of $OPPh_3$ at -90 °C, **2**•O_2PMe_2 and **2**•O_2PPh_2 had to be warmed to -40 °C to attain reasonable rates of conversion. In contrast, **2**•O_2AsMe_2 appears to be unaffected by addition of up to 100 equivalents of $OPPh_3$, even at temperatures as high as 20 °C.

3.3.3 Resonance Raman Spectroscopy

All of the **2**•O_2X and **3**•O_2X intermediates have strong chromophores. For this reason, we opted to examine them using resonance Raman (rR) spectroscopy. However, due to the inherent instability of some **2**•O_2X species, we were unable to trap every intermediate, so rR spectra of only **2**•O_2PMe_2, **2**•$O_2P(OPh)_2$ and **2**•O_2CCPh_3 are presented here (Figures 3.5 and A3.6). Even though **2**•O_2CCPh_3 has a shorter half-life than either **2**•$O_2CC_6H_2$-3,4,5-$(OMe)_3$ or **2**•$O_2CC_6H_3$-3,4-$(OMe)_2$, attempts to obtain spectra of the latter two species were unsuccessful. During the freezing process, a color change was observed.

Respective rR spectra of these samples are comparable to spectra of **3**•$O_2CC_6H_2$-3,4,5-$(OMe)_3$ and **3**•$O_2CC_6H_3$-3,4-$(OMe)_2$, indicating conversion likely takes place during the phase change (Figure A3.7). On the other hand, the stability of the **3**•O_2X intermediates allowed us to collect spectra of every one (Figures 3.5 and A3.7), with the exception of **3**•O_2PMe_2, which we noted earlier does not form in quantities sufficient for characterization. The rR spectrum of **3′**•O_2PPh_2 (Figure 3.6) was also acquired. As it was nearly identical to the spectrum of **3′**•O_2CPh,[29] we did carry out the experiment with other **3′**•O_2X intermediates.

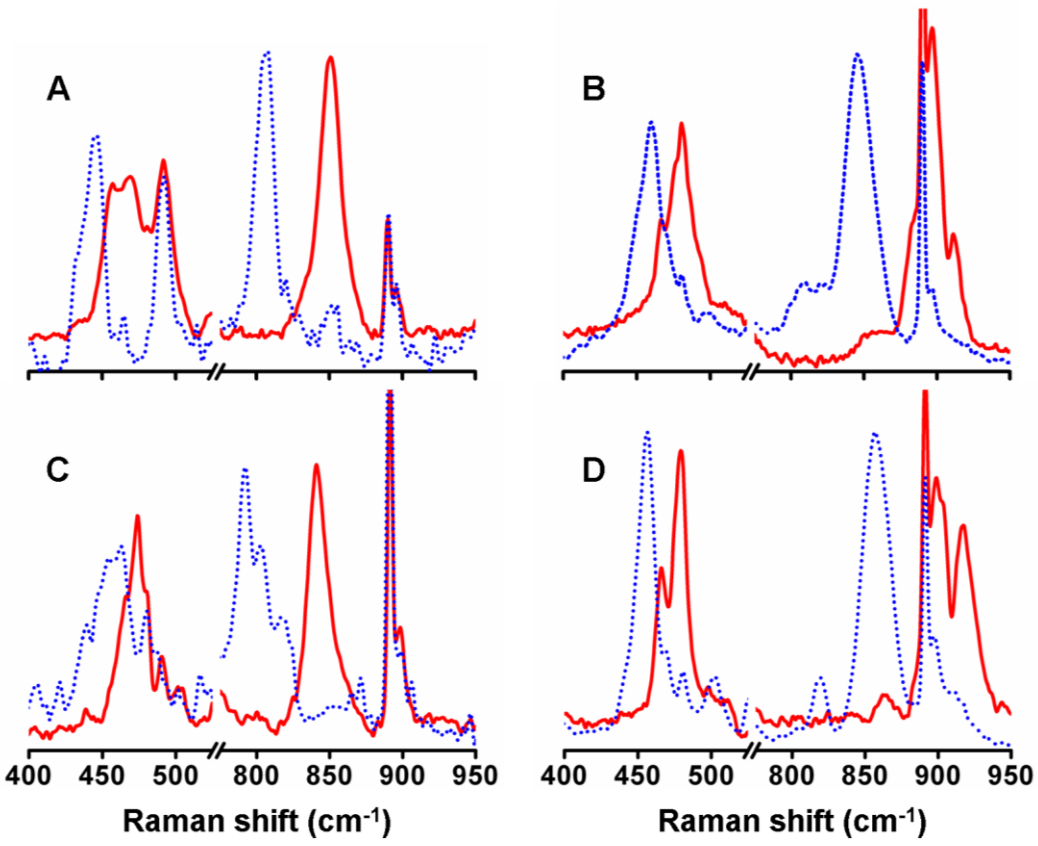

Figure 3.5. Resonance Raman spectra of **2**•$O_2P(OPh)_2$ (**A**), **3**•$O_2P(OPh)_2$ (**B**), **2**•O_2CCPh_3 (**C**) and **3**•O_2CCPh_3 (**D**). Solid red lines ($^{16}O_2$) and dotted blue lines ($^{18}O_2$).

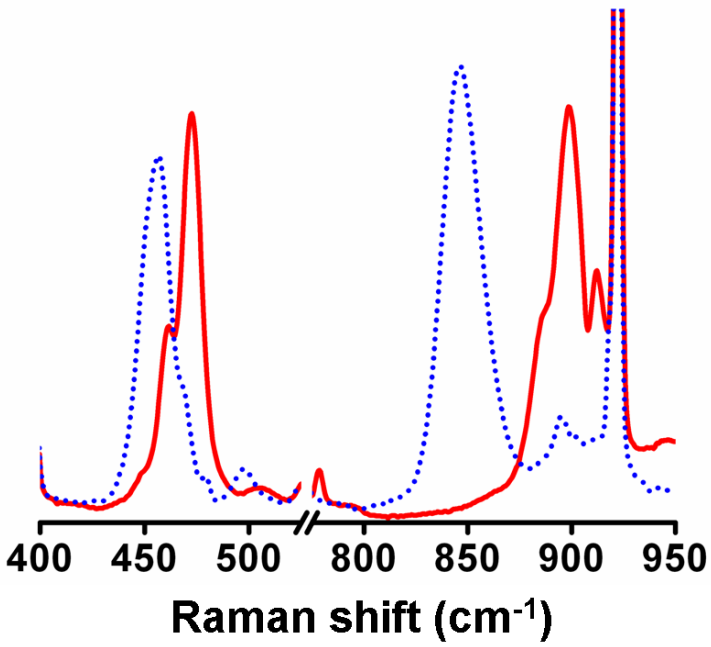

Figure 3.6. Resonance Raman spectra of **3′**•O_2PPh_2 ($^{16}O_2$ = solid red line, $^{18}O_2$ = dotted blue line).

A comparison of these spectra to those in the preceding chapter and others previously published[51,84] allowed us to sort them into two groups. Studies using $^{16}O_2$ and $^{18}O_2$ reveal two clusters of peroxo stretching frequencies (Table 3.5). The **2**•O_2X cluster has $\nu_{O\text{-}O}$ values ranging from 839 to 851 cm^{-1} that shift to 791-807 cm^{-1} upon $^{18}O_2$ substitution. The **3**•O_2X cluster has $\nu_{O\text{-}O}$ values ranging from 897 to ~910 cm^{-1} that shift to a range of 845 to 857 cm^{-1} upon $^{18}O_2$ substitution. The $\nu_{Fe\text{-}O}$ values range from 457 to 479 cm^{-1} (Table 3.5). In most cases, the spectra reveal two isotope-sensitive peaks, which were assigned as the symmetric and asymmetric Fe-O stretches. There is no systematic difference between the $\nu_{Fe\text{-}O}$ values of the **2**•O_2X complexes and those found for the **3**•O_2X complexes.

Table 3.5. Fe-O and O-O stretching frequencies of **2**•O_2X and **3**•O_2X complexes determined using resonance Raman spectroscopy.

O_2X	**2**•O_2X		**3**•O_2X	
	$\nu_{Fe\text{-}O}$ (cm^{-1}) [^{18}O]	$\nu_{O\text{-}O}$ (cm^{-1}) [$^{18}O_2$]	$\nu_{Fe\text{-}O}$ (cm^{-1}) [^{18}O]	$\nu_{O\text{-}O}$ (cm^{-1}) [$^{18}O_2$]
O_2AsMe_2	464 [433]	845 [796]	--	--
O_2PMe_2	467, 479 [449, 460]	839 [791]	--	--
O_2PPh_2	465, 476 [455]	845, 853 [807]	477 [458]	897 [848]
$O_2P(OPh)_2$	457, 469 [436, 446]	851 [806]	479 [460]	897 [845]
O_2CCPh_3	466, 474 [447, 454]	841 [792]	466, 479 [448, 456]	903, 917 [857] [a]
O_2CCMe_3	--	--	466, 475 [447, 457]	897, 912 [b] [846, 860]
O_2CPh [c]	--	--	476 [460]	900 [850]
$O_2CC_6H_2$-3,4,5-$(OMe)_3$	--	--	465, 476 [449, 457]	900, 914 [853]
$O_2CC_6H_3$-3,4-$(OMe)_2$	--	--	466, 474 [449, 456]	898, 912 [847]
$O_2CC_6H_3$-3,5-$(OMe)_2$	--	--	465, 476 [449, 458]	899, 913 [848]
$O_2CC_6H_4$-4-OMe	--	--	466, 474 [448, 457]	899, 913 [847]

[a] The peak at 857 cm^{-1} may also be fit as two peaks at 853 and 862 cm^{-1}, indicating a possible mixture of two peroxo species.
[b] Small peaks at 912 ($^{16}O_2$) and 860 ($^{18}O_2$) cm^{-1} may represent a minority peroxo species.
[c] Values from ref. 51.

3.4 Discussion

One step in the catalytic activation of dioxygen by biological diiron(II) systems often produces (μ-η^1:η^1-peroxo) diiron(III) moieties. Some of these intermediates exhibit a level of stability that allows for them to be trapped and characterized.[11-18] The same is true for many synthetic (μ-η^1:η^1-peroxo) diiron(III) complexes,[20,27,29-31] some of which are so stable they have been cystallographically characterized.[21-24] In the previous chapter, we used the dinucleating ligand N-EtHPTB and three different oxyanions (O_2X) to synthesize dioxygen reducing diiron(II) complexes (**1**•O_2X). Our efforts revealed that the (μ-η^1:η^1-peroxo) diiron(III) intermediates produced upon oxygenation of the diiron(II) precursors come in two forms, green-blue **2**•O_2X and deep blue **3**•O_2X (Scheme 3.1). In the initial form, the oxyanion acts as a three-atom bridge between the iron centers. In some cases, this intermediate converts to a second form, wherein the O_2X ligand has moved to a terminal position, possibly allowing for rearrangement of the N-EtHPTB ligand. We reported that the stability of **2**•O_2X is influenced by the identity of O_2X. We examined three variations (O_2X = O_2AsMe_2, O_2PPh_2 and O_2CPh) and concluded that the dominant factor governing **2**•O_2X stability is the bite distance (O···O) of the O_2X moiety in **1**•O_2X as determined by X-ray crystallography. Greater bite distances produced more stable **2**•O_2X intermediates; in one case, the intermediate was so stable that the

2•O_2X complex did not convert to observable amounts of **3**•O_2X prior to decomposition.

For this work, we synthesized a variety of **1**•O_2X complexes, including two new species with X = P and six new species with X = C. By monitoring the reactions of these diiron(II) complexes with O_2 in solution and characterizing the peroxo intermediates produced, we explored other factors affecting the stability of **2**•O_2X. Specifically, we were interested in examining effects produced by electronic and steric changes in O_2X and how those results relate to effects produced by differences in O_2X bite distances. In addition, we investigated how $OPPh_3$ could be used to destabilize some **2**•O_2X intermediates.

These experiments were designed to examine our proposed mechanism detailing the conversion of **2**•O_2X to **3**•O_2X, in which irreversible conversion to **3**•O_2X is preceded by movement of the O_2X moiety from a bridging to a terminal position (Scheme 3.1). We postulated that the O_2X ligand could rapidly exchange between bridging and terminal coordination modes in **2**•O_2X while the N-EtHPTB ligand remained with the benzimidazole arms *cis* to each other. Only after the arms moved *trans* to each other, would the irreversible conversion to **3**•O_2X be complete. We felt that coordinating molecules, O_2X steric properties and O_2X electronic properties would each affect this transformation in one of three ways: *(i)* We deemed it likely that a coordinating molecule might fill the

position vacated by the O_2X ligand during a shift to the terminal coordination mode. This would prevent the O_2X ligand from returning to a bridging coordination mode, allowing the peroxide to move *trans* to the amine nitrogen atoms, which would in turn allow the benzimidazole arms to move *trans* to each other, thus completing the irreversible conversion to **3**•O_2X. While investigating this hypothesis, we found in every case (with the exception of **2**•O_2AsMe_2) that addition of $OPPh_3$ to **2**•O_2X led to similar changes in the UV-Vis absorption spectra. Spectra initially characteristic of **2**•O_2X changed to spectra characteristic of a new, deep blue species (**3′**•O_2X) with features similar to those of **3**•O_2X, but with more intense LMCT band absorbances. Based on the crystal structure of $[Fe_2(N\text{-}EtHPTB)(O_2)(OPPh_3)_2]^{3+}$ published by Dong et al.,[22] we propose that $OPPh_3$ coordinates in the L position (Scheme 3.1). *(ii)* The benzimidazole arms of the N-EtHPTB ligand are proposed to move from positions *cis* to each other to positions *trans* to each other while the O_2X ligands and peroxo ligands are also changing positions. Because this three-part rearrangement would require O_2X and a benzimidazole arm to squeeze past each other, we proposed that increasing the steric bulk of O_2X would slow down conversion of **2**•O_2X to **3**•O_2X. *(iii)* Conversion to **3**•O_2X requires O_2X to move from a bridging coordination mode to a terminal coordination mode. Because O_2X ligands with greater basicity would presumably coordinate more strongly to the iron, the equilibrium between

bridging and terminal modes would favor the former, slowing down conversion to **3**•O_2X.

3.4.1 Steric and Electronic Effects

Sorting out electronic and steric effects involved the use of various oxyanions with different pK_a values (Table 3.4) and steric bulk. Enhancing the stability of **2**•O_2X by altering the steric properties of the oxyanion can most easily be observed with X = C bridges. Intermediate **2**•O_2CCPh_3 is more stable than **2**•O_2CCMe_3 (k_{obs} = 1.7(2) x 10^{-3} and 1.8(1) x 10^{-2} s^{-1}, respectively), which is in turn more stable than **2**•O_2CPh (k_{obs} = 5.3(1) x 10^{-2} s^{-1}). Both of the substituted acetate bridges have more steric bulk around the carbon atom next to the X atom than does benzoate. HO_2CCMe_3 has a higher pK_a (5.03)[73] than benzoic acid (pK_a = 4.19)[73] which may partially account for the extended lifetime of **2**•O_2CCMe_3. However, **2**•O_2CCPh_3 has an oxyanion bridge that is slightly less basic (protonated pK_a = 3.96)[85] than O_2CPh, although **2**•O_2CCPh_3 is 30-fold more stable than **2**•O_2CPh. It is clear that O_2X steric factors are influencing stabilities of **2**•O_2X species, although we cannot rule out small electronic effects.

We measured rates for disappearance of **2**•O_2X species produced using substituted benzoate bridges and compared those rates with each other and disappearance rates of **2**•O_2X species produced using substituted acetate bridges. Comparing k_{obs} for the conversion of **2**•$O_2CC_6H_2$-3,4,5-$(OMe)_3$ and **2**•O_2CPh to

their respective forms of **3**•O_2X, we find that the former has a value (k_{obs} = 4.2(6) x 10^{-4} s^{-1}) approximately two orders of magnitude smaller than that of the latter (k_{obs} = 5.3(1) x 10^{-2} s^{-1}). Given that their bridges are virtually electronic twins (pK_a = 4.24 and 4.19, respectively),[73,86] the considerable difference between the stabilities of **2**•$O_2CC_6H_2$-3,4,5-$(OMe)_3$ and **2**•O_2CPh (Table 3.4) is probably due to steric considerations. Experiments using other methoxy-substituted benzoates as O_2X lend credence to this interpretation. The stabilizing effect is most pronounced when the oxyanion is $O_2CC_6H_2$-3,4,5-$(OMe)_3$, although every methoxy-substituted benzoate moiety we employed as the bridging oxyanion produced **2**•O_2X species more stable than **2**•O_2CPh (Table 3.4). In general, decreasing the number of methoxy units on the aromatic ring increases the rate at which **2**•O_2X disappears, but the positions of the methoxy substituents also influence stability. While neither **2**•$O_2CC_6H_3$-3,4-$(OMe)_2$ nor **2**•$O_2CC_6H_3$-3,5-$(OMe)_2$ exhibit the stability of **2**•$O_2CC_6H_2$-3,4,5-$(OMe)_3$, they are far from equivalent with respective k_{obs} of 6.6(9) x 10^{-4} and 4.8(2) x 10^{-3} s^{-1}. Data collected during the disappearance of **2**•$O_2CC_6H_4$-4-(OMe) (k_{obs} = 4.7(4) x10^{-3} s^{-1}) show that one methoxy group in the *para* position has the same stabilizing capability as two methoxy groups in the *meta* positions. It should be noted that this similarity is probably due to electronic differences. The oxyanion bridge in **2**•$O_2CC_6H_4$-4-(OMe) is more basic than that in **2**•$O_2CC_6H_3$-3,5-$(OMe)_2$ (pK_a =

4.50 and 3.97, respectively)[86] and the rates of disappearance for each species are the same within error despite the steric differences. From this, it appears that additional steric bulk in the *meta* and/or *para* positions of benzoate-based oxyanions is the primary stabilizer of the resultant **2**•O_2X moieties, although greater O_2X basicity produces the same effect to a lesser degree.

Effects produced by steric changes in X = P bridges were harder to separate from electronic effects. We examined complexes using O_2PMe_2, O_2PPh_2 and $O_2P(OPh)_2$ as oxyanions. Each has significantly different steric properties as well as varying pK_a values (3.08, 2.32 and 1.85, respectively).[72] By far, **2**•O_2PMe_2 is the most stable of the **2**•O_2X (X = P) intermediates. At -90 °C, **2**•O_2PMe_2 is indefinitely stable, as is **2**•O_2PPh_2. However, in contrast to **2**•O_2PMe_2, when warmed to -40 °C, **2**•O_2PPh_2 converts to **3**•O_2PPh_2. The putative conversion of **2**•O_2PMe_2 to **3**•O_2PMe_2 is presumably so slow that it was not observed in solution at any temperature, instead appearing to convert directly to the yellow decay product (**4**•O_2PMe_2). Of the three X = P complexes, only **2**•$O_2P(OPh)_2$ undergoes conversion to its **3**•O_2X analogue at -90 °C, making it the least stable intermediate, although with k_{obs} = 1.2(1) x 10^{-4} s^{-1} for that reaction, it is still more stable than any of the initial X = C intermediates. The lack of stability displayed by **2**•$O_2P(OPh)_2$ relative to the other O_2X (X = P) intermediates is in line with our steric and electronic arguments.

Diphenylphosphate is the weakest base of the three as well as the bridge with the least steric bulk near the central bridging atom. However, the stability of **2**•O_2PMe_2 relative to that of **2**•O_2PPh_2 is more difficult to square with our model. **2**•O_2PMe_2 is clearly more stable than **2**•O_2PPh_2 in spite of the fact that it arguably has less steric bulk near its phosphorus atom. We note that **1**•O_2AsMe_2 is structurally quite similar to **1**•O_2PMe_2 and its resultant peroxo intermediate (**2**•O_2AsMe_2) is the most stable of all that we examined, not producing measurable amounts of **3**•O_2AsMe_2 nor converting to **3′**•O_2AsMe_2 even when reacted with 100 equivalents of $OPPh_3$ at room temperature. Cacodylic acid has pK_a = 6.27,[70,71] making O_2AsMe_2 the most basic oxyanion we examined. Part of the extra stability exhibited by **2**•O_2AsMe_2 may be due to higher bridge basicity, but it seems likely there are other factors enhancing its durability and also that of **2**•O_2PMe_2. Future computational work may shed light on this issue.

For the most part, the steric and electronic stabilizing effects observed during conversion from **2**•O_2X to **3**•O_2X (X =C) are not noticeable in the presence of 20 equivalents of $OPPh_3$, indicating a change in the rate determining step. When $OPPh_3$ was added to solutions of **2**•O_2X at -90 °C, conversion to **3′**•O_2X was equally rapid, regardless of steric and electronic differences with one exception, **2**•O_2CCPh_3 (Table 3.4). While all other k_{obs} values for the conversion of **2**•O_2X to **3′**•O_2X (X = C) fall within experimental error of each other, that of

2•O_2CCPh_3 is small enough to lie just outside that range. This may be due to the fact that O_2CCPh_3 has significantly more steric bulk around the central X atom than any of the other O_2X (X = C) bridges, meaning the rate determining step is still a rearrangement involving the bridge. The presence of $OPPh_3$ does destabilize **2**•O_2CCPh_3 to some degree as indicated by the different first order rate constants for conversion of **2**•O_2CCPh_3 to either **3**•O_2CCPh_3 or **3′**•O_2CCPh_3 (k_{obs} = 0.018(1) and 0.080(3), respectively). The middle ground of stability occupied by **2**•$O_2P(OPh)_2$ is also evident when examining its reaction with $OPPh_3$ in solution. Conversion to **3′**•$O_2P(OPh)_2$ takes place with k_{obs} = 3.1(1) x 10^{-2} s^{-1}, making **2**•$O_2P(OPh)_2$ more resistant to change than any of the **2**•O_2X (X = C) intermediates. On the other hand, even at -40 °C, both **2**•O_2PMe_2 and **2**•O_2PPh_2 react more slowly with $OPPh_3$ (respective k_{obs} = 1.8(4) x 10^{-4} and 4.3(4) x 10^{-3} s^{-1}) than **2**•$O_2P(OPh)_2$ does at -90 °C.

3.4.2 Bite Distance Effects

In Chapter 2, we noted a correlation between the oxyanion O···O distance measured in **1**•O_2X and the stability of **2**•O_2X. In that study, we compared the effects of only three bridges. To examine this in more detail, we were able to crystallographically characterize three more complexes and compare the newly measured distances with those of previously characterized complexes (Table 3.2). An appraisal of those interatom distances and the stabilities of the **2**•O_2X

intermediates produced upon oxygenation reveals a noticeable trend, in line with our earlier observations. The bite distances can be lumped into three categories (X = As, 2.80 Å; X = P, 2.55 Å; X = C, 2.23 Å). Each X atom produces **2**•O_2X intermediates within a stability range. The X = C bridges are the least stable, with the longest lived **2**•O_2X species being less stable than the shortest lived of the **2**•O_2X (X = P) intermediates. Further expanding the O···O distance using X = As produces a **2**•O_2X species that is more stable than the longest lived **2**•O_2X (X = P) intermediates. This trend clearly indicates that a short oxyanion bite distance destabilizes the resultant **2**•O_2X intermediate. As we indicated previously, we expect this short distance imposes strain on the six-member ring formed by the three atoms of the oxyanion bridge, the two iron atoms and the alkoxide oxygen on the N-EtHPTB ligand. Expanding the bite distance relieves some of that strain, making it less susceptible to opening, which leads to conversion to **3**•O_2X.

3.4.3 Summary and Conclusion

We have synthesized several new diiron(II) complexes and reacted them with dioxygen in solution producing triply-bridged (μ-η^1:η^1-peroxo)diiron(III) intermediates. Previously published diiron(II) complexes[31,40] were also examined and determined for the first time to produce analogous peroxo intermediates upon oxidation. In all cases except for two, these triply-bridged species convert to doubly-bridged (μ-η^1:η^1-peroxo)diiron(III) intermediates via the simple expedient

of rearrangement of an oxyanion. This conversion was observable using UV-Vis spectroscopy. When possible, samples were characterized using resonance Raman spectroscopy. This revealed that the triply-bridged peroxo intermediates have ν_{O-O} values approximately 50 cm^{-1} lower than their doubly-bridged counterparts. All but one of the triply-bridged peroxo intermediates reacted with $OPPh_3$ to produce a second type of doubly-bridged peroxo intermediate. Discounting minor differences in absorption intensity, the UV-Vis spectra of these intermediates were comparable to those of their respective other doubly-bridged species. Resonance Raman spectra of species produced upon addition of $OPPh_3$ revealed no measurable vibrational energy differences between the two types of doubly-bridged intermediates. The stability of the triply-bridged species is heavily influenced by the bite distance of the oxyanion bridge. Steric and electronic differences in these bridges also affect the stability, albeit to a lesser degree. Our work indicates that there are probably other factors influencing the stability. Computational methods may be the best means for investigating this question.

3.5 Acknowledgements

This work was supported by the National Institutes of Health through Grant GM-38767. We thank Dr. Victor Young, Jr. of the X-ray Crystallographic Laboratory at the University of Minnesota for his invaluable assistance.

3.6 Appendix

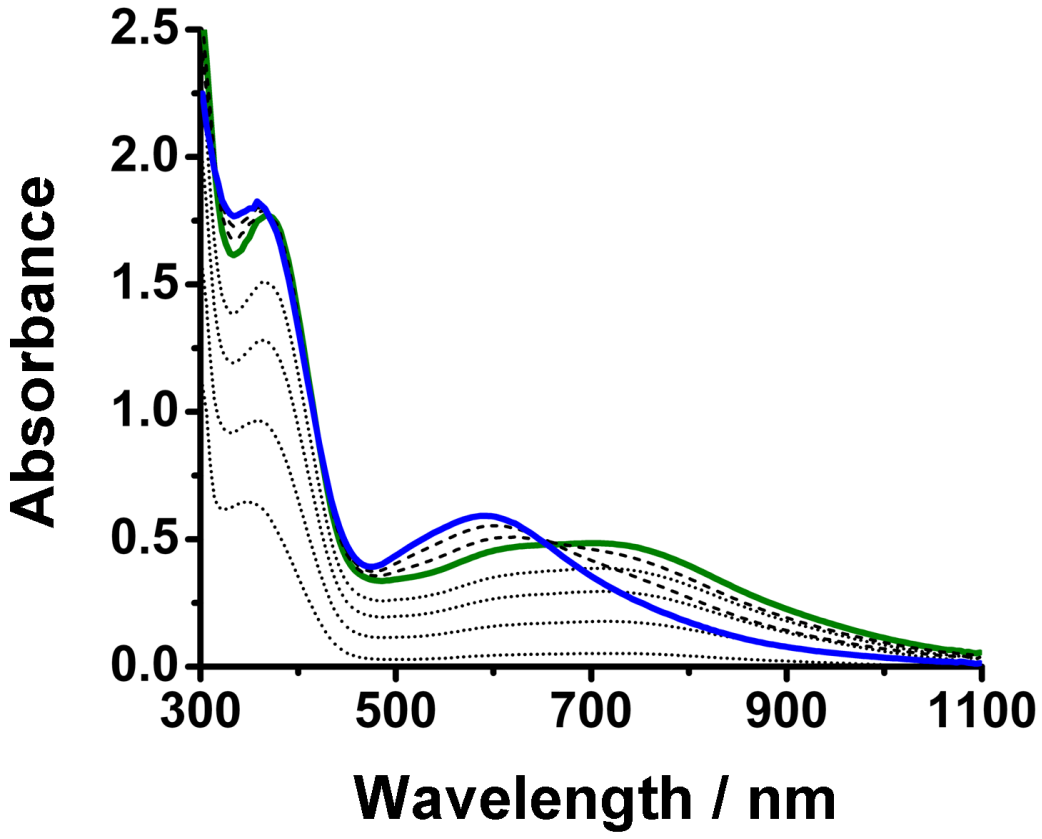

Figure A3.1. Selected UV-Vis spectra showing formation of **2**•$O_2CC_6H_2$-3,4,5-$(OMe)_3$ (solid green line) and subsequent conversion to **3**•$O_2CC_6H_2$-3,4,5-$(OMe)_3$ (solid blue line). Dotted lines indicate appearance of **2**•$O_2CC_6H_2$-3,4,5-$(OMe)_3$, dashed lines indicate conversion to **3**•$O_2CC_6H_2$-3,4,5-$(OMe)_3$.

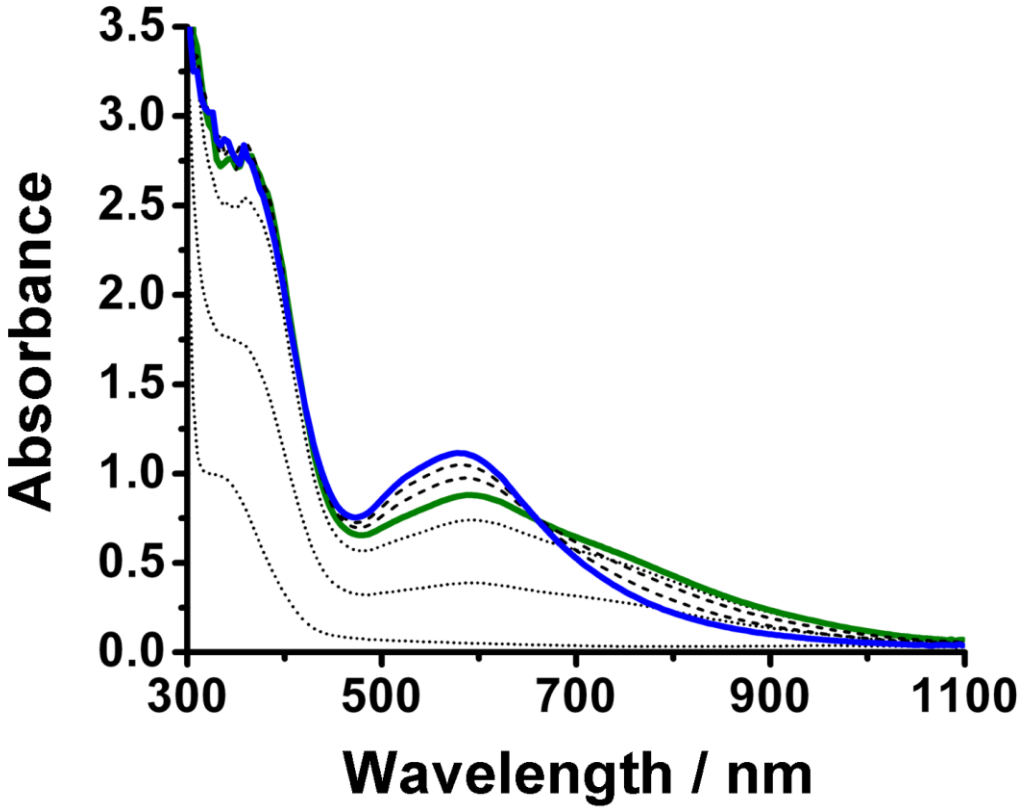

Figure A3.2. Selected UV-Vis spectra showing formation of **2**•$O_2CC_6H_3$-3,4-$(OMe)_2$ (solid green line) and subsequent conversion to **3**•$O_2CC_6H_3$-3,4-$(OMe)_2$ (solid blue line). Dotted lines indicate appearance of **2**•$O_2CC_6H_3$-3,4-$(OMe)_2$, dashed lines indicate conversion to **3**•$O_2CC_6H_3$-3,4-$(OMe)_2$.

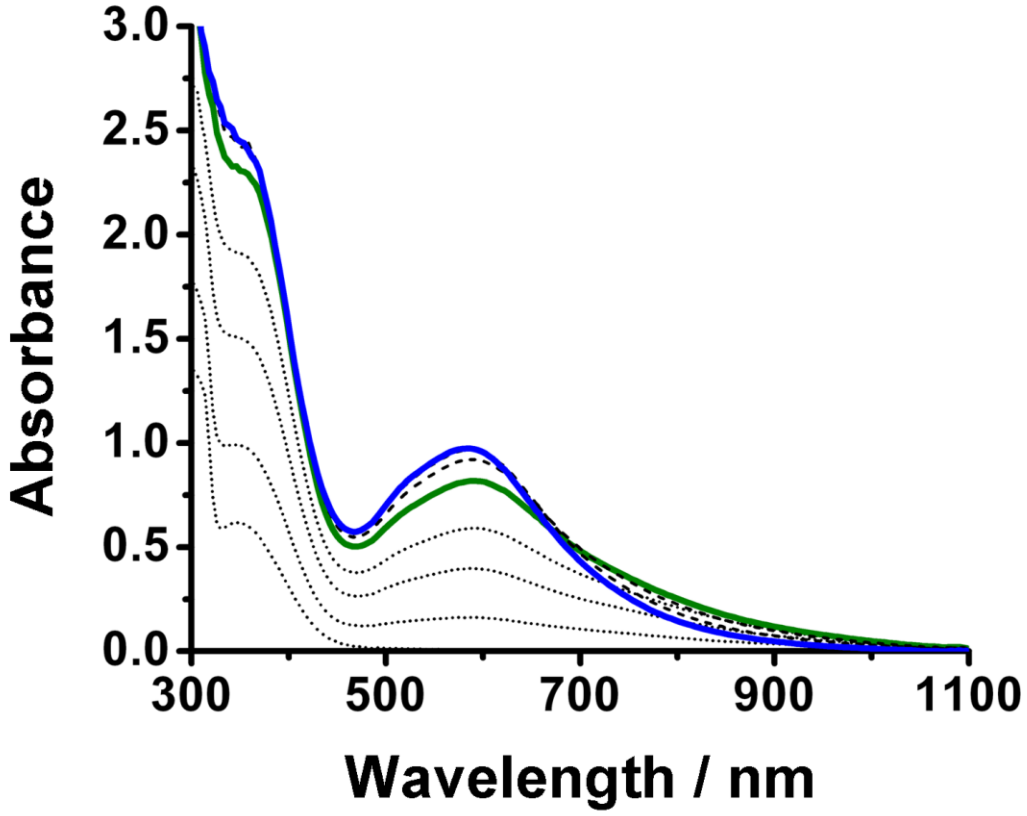

Figure A3.3. Selected UV-Vis spectra showing formation of **2**•$O_2CC_6H_3$-3,5-$(OMe)_2$ (solid green line) and subsequent conversion to **3**•$O_2CC_6H_3$-3,5-$(OMe)_2$ (solid blue line). Dotted lines indicate appearance of **2**•$O_2CC_6H_3$-3,5-$(OMe)_2$, dashed lines indicate conversion to **3**•$O_2CC_6H_3$-3,5-$(OMe)_2$.

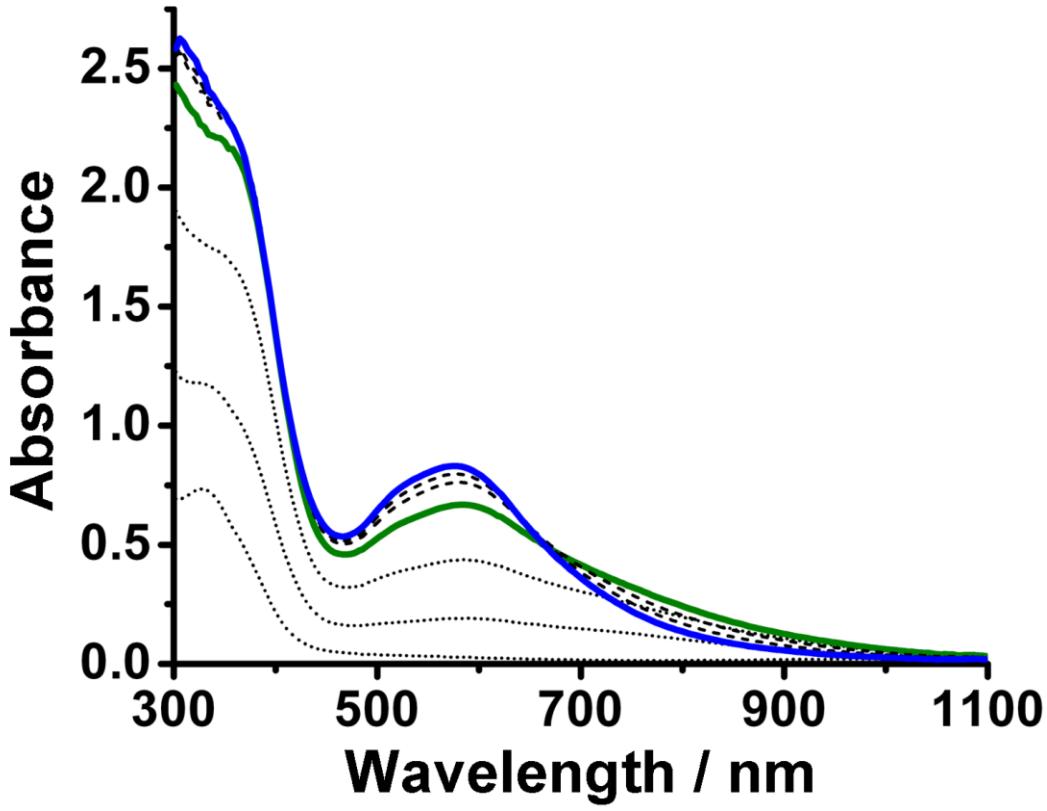

Figure A3.4. Selected UV-Vis spectra showing formation of **2**•$O_2CC_6H_4$-4-OMe (solid green line) and subsequent conversion to **3**•$O_2CC_6H_4$-4-OMe (solid blue line). Dotted lines indicate appearance of **2**•$O_2CC_6H_4$-4-OMe, dashed lines indicate conversion to **3**•$O_2CC_6H_4$-4-OMe.

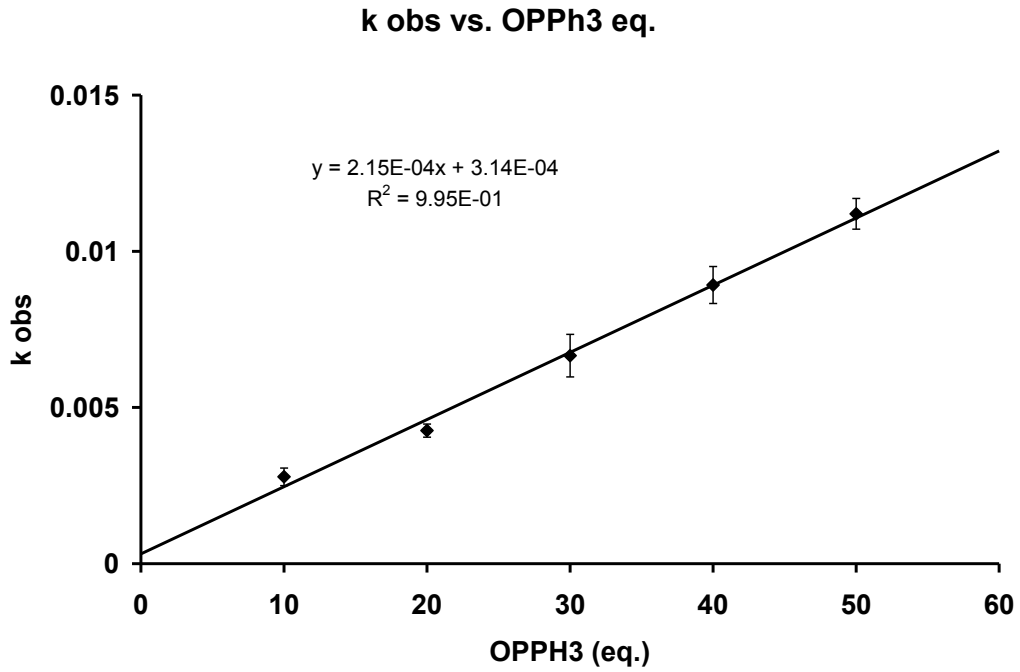

Figure A3.5. k_{obs} for the conversion of **2**•O_2PPh_2 to **3**•O_2PPh_2 in CH_2Cl_2 at -40 °C was determined by finding the y-intercept produced by finding k_{obs} for the conversion induced by addition of varying equivalents of $OPPh_3$.

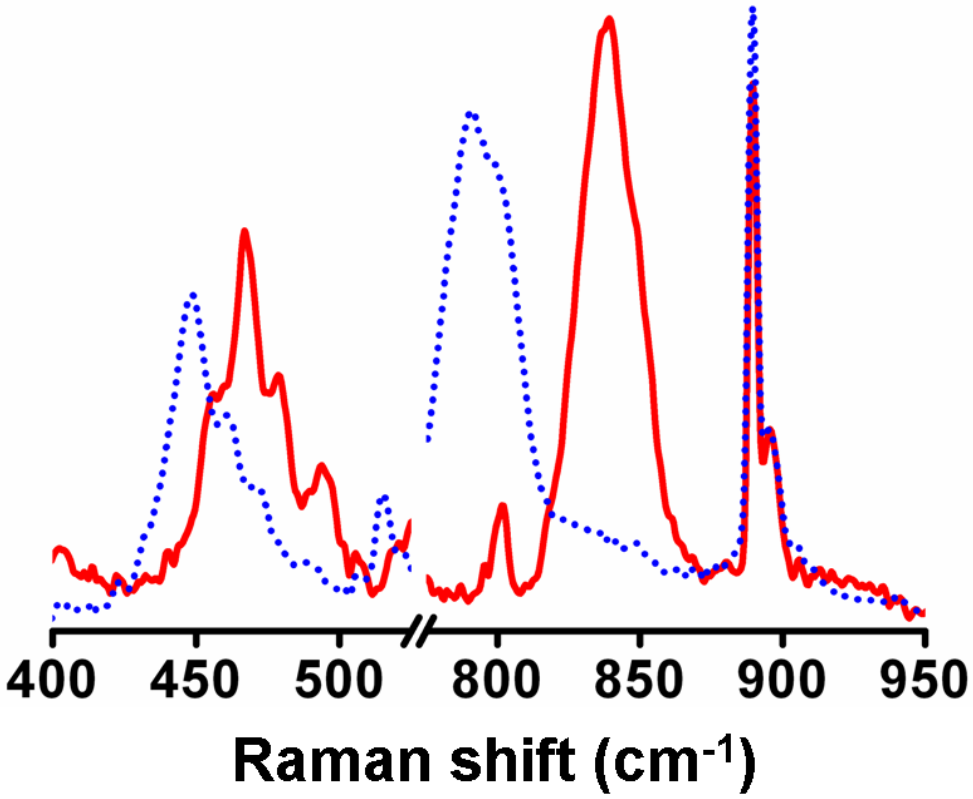

Figure A3.6. Resonance Raman spectra of **2**•O_2PMe_2 (solid red line = $^{16}O_2$, dotted blue line = $^{18}O_2$).

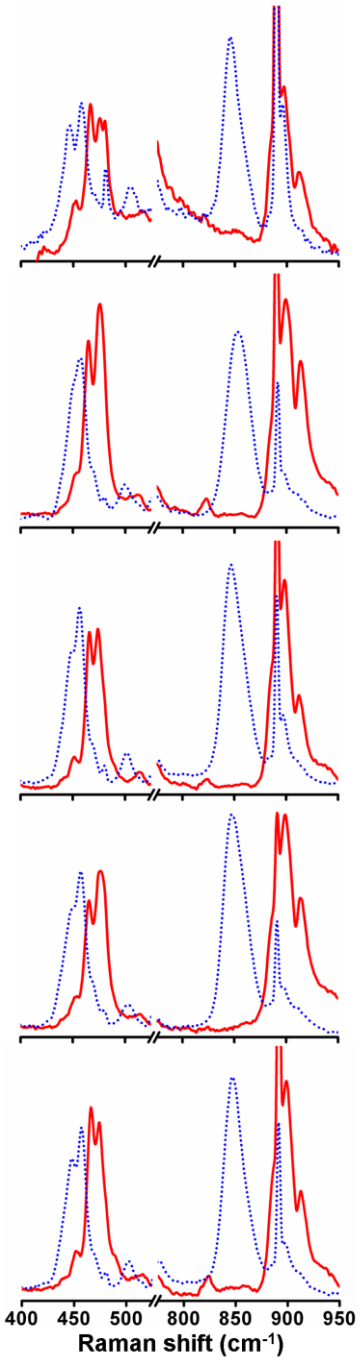

Figure A3.7. From top to bottom, resonance Raman spectra of **3**•O_2CCMe_3, **3**•$O_2CC_6H_2$-3,4,5-$(OMe)_3$, **3**•$O_2CC_6H_3$-3,4-$(OMe)_2$, **3**•$O_2CC_6H_3$-3,5-$(OMe)_2$, and **3**•$O_2CC_6H_4$-4-OMe (solid red line = $^{16}O_2$, dotted blue line = $^{18}O_2$).

Chapter 4: X-ray Crystallographic Examination of Tetrairon(III) Complexes

4.1 Introduction

As more oxygen-activating diiron enzymes became known and studied,[1,3,5-10] the difficulties inherent in trapping and characterizing biological intermediates became more of a problem. While in some cases, catalytically important species were trapped and characterized,[11-19] often it was not possible. To counter these difficulties, researchers turned to synthetic analogues. Reactions of these synthetic diiron(II) complexes with various oxidants are studied as models to provide insight into the reaction mechanisms of a variety of enzymes which contain diiron centers.[20-29] A class of these models is formed using ligands that fit into a basic structural pattern which includes an *N,N,N',N'*-tetrasubstituted 1,3-diaminopropan-2-ol backbone. In a subgroup of this class, the amine substituents contain nitrogen, resulting in ligands that can bind two metal atoms, with each atom in a 3N1O binding motif. In addition to this subgroup, there are also a few molecules in which one of the amine substituents is ligated through an atom other than nitrogen, or in some cases, not ligated at all, resulting in binding motifs different than 3N1O on one of the metal centers. Finally, a bridging anionic molecule is usually needed between the metal centers, producing a complex containing two five-coordinate iron atoms (Figure 4.1). This bridge is often some form of carboxylate, although other molecules have been used.

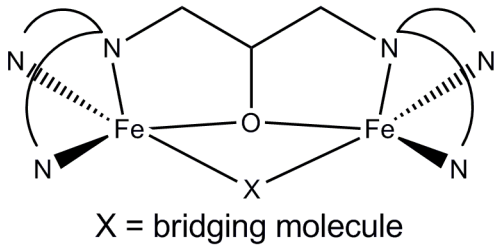

Figure 4.1. A representation of a generic diiron(II) complex formed using the 1,3-diaminopropan-2-ol backbone with a bridging molecule X. This picture clearly shows the 3N1O1X ligand binding motif on each iron center.

In cases where the metal centers are iron(II) atoms, the complexes may be reacted with oxidants (often dioxygen) in attempts to observe reaction sequences yielding information about the mechanisms of analogous biological systems. All too often, the intermediates of these reactions are ephemeral and thus poorly characterized. However, upon reaction with an oxidant, these substances almost inevitably form diiron(III) complexes, which often ultimately dimerize into tetranuclear iron(III) clusters. In addition to the 3N1O motif typically apparent, each iron atom is ligated to two bridging units, resulting in coordinatively saturated iron centers. These tetranuclear complexes can be broken into three main types where: *(i)* the bridging molecules rearrange to bridge the halves of the dimer, *(ii)* the bridging molecules are replaced by something else and are no longer part of the dimer, and *(iii)* the bridging molecules retain their original positions between the iron centers (Figure 4.2).

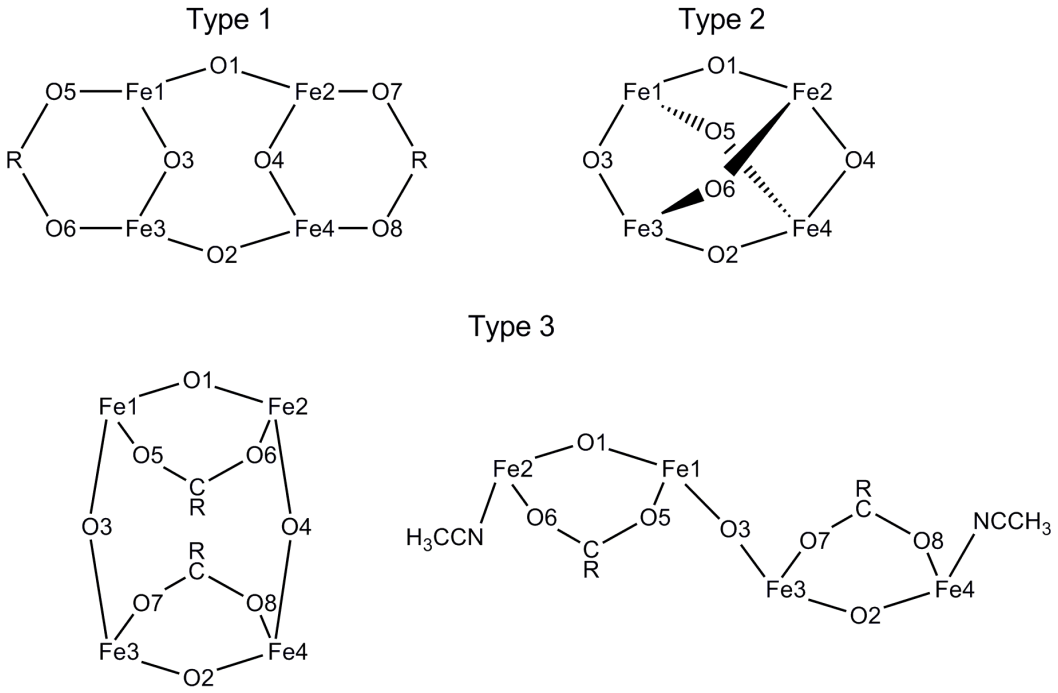

Figure 4.2. For all Types, O1 and O2 represent the ligand alkoxides and O3 and O4 represent bridging oxides. For Type 2, O5 and O6 represent bridging hydroxides, otherwise O5, O6, O7 and O8 represent oxygen atoms of bridging anions. Not shown: the three additional nitrogen atoms ligated to each iron atom.

In this chapter we will discuss possible reasons for these structural differences and how these variations might reveal information regarding the character of the intermediates between the diiron(II) and tetranuclear iron(III) species. For purposes of comparison, several previously published crystal structures will be discussed here. They will be referred to using the six-letter codes assigned by the Cambridge Crystallographic Data Centre.

4.2 Experimental Section

All reagents and solvents were purchased from commercial sources and were used as received, unless noted otherwise. The ligand HPTP **(1)** was synthesized using a published procedure.[51,87] Solvents were dried according to published procedures and distilled under Ar prior to use.[42] Preparation and handling of air sensitive materials were carried out under an inert atmosphere by using either standard Schlenk and vacuum line techniques or a glovebox. Elemental analyses were performed by Atlantic Microlab, Inc., Norcross, GA. *Caution:* Perchlorate salts are potentially explosive and should be handled with extreme care and prepared in small quantities.

$[Fe^{II}_2(HPTP)(O_2CPh)_2](BPh_4)$. (2)$(BPh_4)$

This complex was synthesized using a published procedure.[88] Anal. for **2**(BPh_4)•MeCN•$0.5H_2O$ and calcd for $C_{67}H_{63}BFe_2N_7O_{5.5}$: C, 68.38; H, 5.40; N, 8.33%. Found: C, 68.31; H, 5.42; N, 8.56%.

$[Fe^{II}_2(HPTP)(O_2CCH_3)](BPh_4)_2$. (3)$(BPh_4)_2$

1 (194 mg, 0.227 mmol) was dissolved in MeOH (~10 mL) along with Et_3N (0.17 mL, 1.3 mmol). Sodium acetate (18.9 mg, 0.230 mmol) was added and allowed to dissolve. $Fe(OTf)_2$•2MeCN[43] (203 mg, 0.466 mmol) was added, producing a yellow solution. After 5 minutes, $NaBPh_4$ (171 mg, 0.499 mmol) was added, resulting in immediate precipitation of a white powder. The solid was filtered and dried *in vacuo*. Recrystallization from MeCN and Et_2O produced

colorless crystals. Yield: 201 mg (70%). Anal. for **3**$(BPh_4)_2$ and calcd for $C_{77}H_{72}B_2Fe_2N_6O_3$: C, 73.24; H, 5.75; N, 6.66%. Found: C, 73.01; H, 5.59; N, 6.96%. NMR(300 MHz, CD_3CN): δ 205.2 (s, 1H, CH), 150.6 (s, 2H, CH_2), 111.4 (s, 2H, α), 90.8 (s, 2H, α'), 74.6 (s, 2H, CH_2), 61.1 (s, 2H, CH_2), 45.3 (s, 2H, CH_2), 43.7 (s, 2H, β), 43.4 (s, 2H, β), 41.9 (s, 4H, β'), 40.8 (s, 2H, CH_2), 20.2 (s, 3H, CH_3), 11.8 (s, 2H, CH_2), -2.6 (s, 2H, γ), -4.0 (s, 2H, γ').

$[Fe_4(HPTP)_2(O)_2(NO_3)_2](ClO_4)_4$·6MeCN. (4)$(ClO_4)_4$·6MeCN

1 (267.1 mg, 0.312 mmol) was dissolved in EtOH (30 mL). Triethylamine (157.9 mg, 1.56 mmol) was added and solution was stirred until all solid was dissolved. $Fe(NO_3)_3$·$9H_2O$ (253.0 mg, 0.626 mmol) was added, resulting in a murky green-brown mixture. Filtration yielded a clear, yellow liquid and pea-green paste. The solid was rinsed with cold EtOH and dried in vacuo. Green crystals suitable for x-ray analysis were grown by Et_2O vapor diffusion into a MeCN solution of the solid. Yield: 108 mg (41%). Anal. for **4**$(ClO_4)_4$ and calcd for $C_{54}H_{58}Cl_4Fe_4N_{14}O_{26}$: C, 38.51; H, 3.47; N, 11.64%. Found: C, 38.82; H, 3.49; N, 11.83%.

$[Fe^{III}_4(HPTP)_2(O_2CC_6H_5)_4(O)_2](BPh_4)_2$. (5)$(BPh_4)_2$

A solution of **2**(BPh_4) in CH_2Cl_2 was exposed to air until the solution turned a brown color. The resulting solution was crystallized by vapor diffusion of ether. The complex formed as green crystals suitable for x-ray analysis. Anal.

for **5**$(BPh_4)_2$•CH_2Cl_2 and calcd for $C_{131}H_{120}B_2Fe_4N_{12}O_{12}Cl_2$: C, 66.39; H, 5.10; N, 7.09%. Found: C, 66.22; H, 5.20; N, 6.73%.

$[Fe^{III}_4(HPTP)_2(OH)_2(O)_2](ClO_4)_3(NO_3)$·MeCN. (6)$(ClO_4)_3(NO_3)$·MeCN

1 (195.6 mg, 0.229 mmol) was dissolved in EtOH (10 mL). Triethylamine (127.5 mg, 1.26 mmol) was added and solution was stirred until all solid was dissolved. $Fe(NO_3)_3·9H_2O$ (262.2 mg, 0.649 mmol) was added, resulting in a yellow-brown mixture. Filtration yielded a red-brown precipitate which was rinsed with cold EtOH and dried in vacuo. Blocky, red-brown crystals suitable for x-ray analysis were grown by Et_2O vapor diffusion into a MeCN solution of the solid. Yield: 120 mg (66%). Anal. for **6**$(ClO_4)_3(NO_3)$ and calcd for $C_{54}H_{60}Cl_3Fe_4N_{13}O_{21}$: C, 41.66; H, 3.88; N, 11.70%. Found: C, 41.44; H, 4.21; N, 11.38%.

$[Fe^{II}_2Fe^{III}_2(HPTP)_2(O_2CCH_3)_2O](BPh_4)_4$. (7)$(BPh_4)_4$

A concentrated solution of **3**$(BPh_4)_2$ in acetonitrile was exposed to the atmosphere in a NMR tube. Ether was then layered over this solution and the NMR tube was capped and allowed to sit for two weeks. More ether was applied again to compensate for evaporation and the solution was allowed to sit for another two weeks. The complex formed as small, red crystals suitable for x-ray analysis. The initial yield was miniscule and repeated attempts to produce the amount of complex necessary for elemental analysis were unsuccessful.

4.3 Results

Brief crystal data and intensity collection parameters for the crystalline complexes are shown in Table 4.1, selected bond lengths and interatom distances are shown in Table 4.2 and Table 4.3 summarizes the average lengths of various Fe-O bond types found in each of the crystal types shown in Figure 4.2.

4$(ClO_4)_4 \cdot 6MeCN$

A crystal (approximate dimensions 0.20 x 0.10 x 0.10 mm^3) was placed onto the tip of a 0.1 mm diameter glass capillary and mounted on a Siemens SMART Platform CCD diffractometer for a data collection at 173(2) K.[44] A preliminary set of cell constants was calculated from reflections harvested from three sets of 20 frames. These initial sets of frames were oriented such that orthogonal wedges of reciprocal space were surveyed. This produced initial orientation matrices determined from 61 reflections. The data collection was carried out using MoKα radiation (graphite monochromator) with a frame time of 60 seconds and a detector distance of 4.906 cm. A randomly oriented region of space was surveyed to the extent of 1.5 hemispheres and to a resolution of 0.80 Å. Three major sections of frames were collected with 0.30° steps in ω at three different φ settings and a detector position of -28° in 2θ. The intensity data were corrected for absorption and decay using SADABS.[45] Final cell constants were calculated from the xyz centroids of 3119 strong reflections from the actual data collection after integration using SAINT.[46]

The structure was solved and refined using SHELXL-97.[47] The space group P-1 was determined based on systematic absences and intensity statistics. A direct-methods solution was calculated which provided most non-hydrogen atoms from the E-map. Full-matrix least squares/difference Fourier cycles were performed which located the remaining non-hydrogen atoms. All non-hydrogen atoms were refined with anisotropic displacement parameters. All hydrogen atoms were placed in ideal positions and refined as riding atoms with relative isotropic displacement parameters. The final full matrix least squares refinement converged to $R1 = 0.0620$ and $wR2 = 0.1605$ (F^2, all data).

Two perchlorate anions are disordered over two positions each (89:11 and 52:48). One solvent molecule is also disordered over two positions (70:30). The remaining solvent molecules were restrained to give fixed bond lengths (C-C, 1.470(5) and C-N, 1.136(5)) and linearity. An ORTEP illustration of **4** is shown in Figure 4.3.

5$(BPh_4)_2$

A crystal (approximate dimensions 0.21 x 0.19 x 0.14 mm^3) was placed onto the tip of a 0.1 mm diameter glass capillary and mounted on a Bruker SMART Platform CCD diffractometer for a data collection at 173(2) K.[44] A preliminary set of cell constants was calculated from reflections harvested from three sets of 20 frames. These initial sets of frames were oriented such that orthogonal wedges of reciprocal space were surveyed. This produced initial

orientation matrices determined from 30 reflections. The data collection was carried out using MoKα radiation (graphite monochromator) with a frame time of 60 seconds and a detector distance of 4.891 cm. A randomly oriented region of space was surveyed to the extent of 1.5 hemispheres and to a resolution of 0.84 Å. Three major sections of frames were collected with 0.30° steps in ω at three different φ settings and a detector position of -28° in 2θ. The intensity data were corrected for absorption and decay using SADABS.[45] Final cell constants were calculated from the xyz centroids of 2332 strong reflections from the actual data collection after integration using SAINT.[46]

The structure was solved using SIR97[89] and refined using SHELXL-97.[47] The space group $P2_1/c$ was determined based on systematic absences and intensity statistics. A direct-methods solution was calculated which provided most non-hydrogen atoms from the E-map. Full-matrix least squares/difference Fourier cycles were performed which located the remaining non-hydrogen atoms. All non-hydrogen atoms were refined with anisotropic displacement parameters. All hydrogen atoms were placed in ideal positions and refined as riding atoms with relative isotropic displacement parameters. Disordered solvent was present which could not be refined appropriately. The reflection file was altered using the SQUEEZE function of the program PLATON,[83,90] which determined that there were 186 electrons in 1574 $Å^3$ (approximately four CH_2Cl_2 molecules in a space much larger than required, although the presence of additional water molecules

cannot be ruled out) which could not be resolved. Because of this uncertainty in the composition and number of solvent molecules, some values in Table 4.2 may not be accurate. A very large number of constraints were applied in the refinement of this structure, the majority of them associated with tetraphenylborate counterions. The final full matrix least squares refinement converged to $R1 = 0.0701$ and $wR2 = 0.1931$ (F^2, all data).

One carboxylate group is disordered over two positions (74:26). One pyridine group is also disordered over two positions (74:26). The alkoxy-carbon environment is disordered over two positions (48:52). One tetraphenylborate ion is disordered over three positions (48:21:31). Application of heavy restraints prevents accurate determination of the nitrogen position in the disordered pyridine group relative to the β′ carbon atom in the same aromatic system. Figures 4.4 and 4.5 show ORTEP illustrations of respectively, **5** and the tetranuclear center of **5** including only the iron and bridging atoms.

6$(ClO_4)_3(NO_3)$·MeCN

A crystal (approximate dimensions 0.35 x 0.35 x 0.35 mm^3) was placed onto the tip of a 0.1 mm diameter glass capillary and mounted on a Bruker SMART Platform CCD diffractometer for a data collection at 173(2) K.[44] A preliminary set of cell constants was calculated from reflections harvested from three sets of 20 frames. These initial sets of frames were oriented such that orthogonal wedges of reciprocal space were surveyed. This produced initial

orientation matrices determined from reflections. The data collection was carried out using MoKα radiation (graphite monochromator) with a frame time of 30 seconds and a detector distance of 4.900 cm. A randomly oriented region of reciprocal space was surveyed to the extent of one sphere and to a resolution of 0.84 Å. Four major sections of frames were collected with 0.30º steps in ω at four different ϕ settings and a detector position of -28º in 2θ. The intensity data were corrected for absorption and decay using SADABS.[45] Final cell constants were calculated from the xyz centroids of 6257 strong reflections from the actual data collection after integration using SAINT.[46]

The structure was solved and refined using SHELXL-97 (Sheldrick, 1997).[47] The space group I4(1)/acd was determined based on systematic absences and intensity statistics. A direct-methods solution was calculated which provided most non-hydrogen atoms from the E-map. Full-matrix least squares / difference Fourier cycles were performed which located the remaining non-hydrogen atoms. All non-hydrogen atoms were refined with anisotropic displacement parameters. All hydrogen atoms were placed in ideal positions and refined as riding atoms with relative isotropic displacement parameters. The final full matrix least squares refinement converged to $R1 = 0.0867$ and $wR2 = 0.2689$ (F^2, all data).

Due to the extremely high symmetry found in space group I4(1)/acd, several of the ions lie on symmetry positions. Two of the three perchlorate anions are located on special positions, as is the cation. In the case of the cation, the O-H

bonds of the bridging hydroxides are directly on a screw axis. The nitrate also lies on a symmetry position, but the size of the thermal ellipses associated with it, indicate a significant measure of disorder. This special position appears to be partially occupied by a perchlorate ion, but attempts to model it as such proved unsuccessful. The final perchlorate is the only ion not on a symmetry position and it is disordered over two locations (55:45). The disorder produced by the substitution of perchlorate and nitrate ions on a symmetry position influences the positions of the HPTP pyridyl ring nearest that location. Because of this, some disorder of one pyridylmethyl arm in the cation is apparent (Figure 4.6), although the thermal ellipsoids denoting the iron and oxygen atoms making up the tetranuclear center are well defined (Figure 4.7).

7$(BPh_4)_4$

A crystal (approximate dimensions 0.42 x 0.35 x 0.21 mm^3) was placed onto the tip of a 0.1 mm diameter glass capillary and mounted on a Bruker SMART Platform system for a data collection at 173(2) K.[44] A preliminary set of cell constants was calculated from reflections harvested from three sets of 20 frames. These initial sets of frames were oriented such that orthogonal wedges of reciprocal space were surveyed. This produced initial orientation matrices determined from 120 reflections. The data collection was carried out using MoKα radiation (graphite monochromator) with a frame time of 60 seconds and a detector distance of 4.9 cm. A randomly oriented region of space was surveyed to

the extent of 1.5 hemispheres and to a resolution of 0.84 Å. Three major sections of frames were collected with 0.30° steps in ω at three different φ settings and a detector position of -28° in 2θ. The intensity data were corrected for absorption and decay SADABS.[45] Final cell constants were calculated from the xyz centroids of 3348 strong reflections from the actual data collection after integration using SAINT.[46]

The structure was solved and refined using SHELXL-97.[47] The space group $P2_1$ was determined based on systematic absences and intensity statistics. A direct-methods solution was calculated which provided most non-hydrogen atoms from the E-map. Full-matrix least squares/difference Fourier cycles were performed which located the remaining non-hydrogen atoms. All non-hydrogen atoms were refined with anisotropic displacement parameters. All hydrogen atoms were placed in ideal positions and refined as riding atoms with relative isotropic displacement parameters. The final full matrix least squares refinement converged to $R1 = 0.0471$ and $wR2 = 0.1393$ (F^2, all data).

Application of PLATON/SQUEEZE[83,90] found a void of 451 $Å^3$ out of a unit cell volume of 6960.5 $Å^3$, or 6.5%. The analysis of diffuse scattering placed 88 electrons within this void due to disordered solvent. Eight molecules of MeCN fit within this space, but this could also be a mixture of diethylether as well. Because of this uncertainty in the composition and number of solvent molecules, some values in Table 4.2 may not be accurate. SQUEEZE corrected data were

used for the final stages of refinement. An ORTEP illustration of **7** is shown in Figure 4.8.

Table 4.1. Crystal data and structure refinement for **4**, **5**, **6**, and **7**.

	4	**5**	**6**	**7**
empirical formula	$C_{66}H_{76}Cl_4Fe_4N_{20}O_{26}$	$C_{130}H_{118}B_2Fe_4N_{12}O_{12}$	$C_{28}H_{31.5}Cl_{1.5}Fe_2N_7O_{10.5}$	$C_{158}H_{150}B_4Fe_4N_{14}O_7$
fw	1930.67	2285.38	798.98	2623.56
T (K)	173(2)	173(2)	173(2)	173(2)
Mo K α λ, Å	0.71073	0.71073	0.71073	0.71073
space group	P-1	$P2_1/c$	$I4_1/acd$	$P2_1$
a (Å)	13.2289	14.833	24.0749	15.9303
b (Å)	15.1629	24.98	24.0749	23.8896
c (Å)	22.7357	17.837	48.606	18.2968
α (deg)	73.801	90	90	90
β (deg)	84.235	99.939	90	91.591
γ (deg)	71.898	90	90	90
V (Å^3)	4162.2	6510	28172	6960.5
Z	2	2	32	2
ρ (calc), Mg/m^3	1.54	1.166	1.507	1.252
abs coeff (mm^{-1})	0.899	0.497	1.002	0.471
R1[a]	0.062	0.0701	0.0867	0.0471
wR2[b]	0.1116	0.1236	0.2529	0.0748

[a] $R1 = \Sigma||F_o|-|F_c|| / \Sigma|F_o|$. [b] $wR2 = [\Sigma[w(F_o^2-F_c^2)^2] / \Sigma [w(F_o^2)^2]]^{1/2}$.

Table 4.2. Fe-O bond lengths and Fe···Fe interatom distances (Å). Atom labeling schemes from Figure 4.2.

	Type 1					Type 2		Type 3		
	JUJMAC	**QOLJUW**	**GUNDUO**	**4**	**5**	**LAXNIH**	**6**	**GIJDUY**	**GIJFAG**	**7**
Ligand	N-MeHP3BMe	HP3PPhO	HP3PH	HPTP	HPTP	HPDTACN	HPTP	HPTB	N-EtHPTB	HPTP
Fe1–O1	1.958	2.061	2.030	2.056	1.992	1.989	2.026	1.995	2.023	2.023
Fe2–O1	2.026	2.018	2.000	2.057	1.992	2.070	1.989	2.018	1.987	2.008
Fe3–O2	2.026	2.024	2.019	2.010	1.992	2.039	2.000	2.018	1.987	2.023
Fe4–O2	1.958	2.043	2.022	2.012	1.992	2.051	2.025	1.995	2.023	2.008
Fe1–O3	1.772	1.815	1.786	1.789	1.778	1.796	1.804	1.789	1.796	1.804
Fe2–O4	1.810	1.776	1.796	1.780	1.793	1.811	1.796	1.798	1.791	--
Fe3–O3	1.810	1.797	1.790	1.807	1.793	1.770	1.806	1.798	1.791	1.804
Fe4–O4	1.772	1.819	1.795	1.806	1.778	1.828	1.816	1.789	1.796	--
Fe1–O5	1.978	2.053	2.024	2.038	2.074	1.987	1.981	2.209	1.995	2.016
Fe2–O7	2.085	2.048	2.020	2.056	2.073	--	--	--	--	--
Fe2–O6	--	--	--	--	--	1.971	2.070	2.014	1.964	2.097
Fe3–O6	2.085	2.024	2.031	1.992	2.073	2.026	2.057	--	--	--
Fe3–O7	--	--	--	--	--	--	--	2.014	1.964	2.016
Fe4–O5	--	--	--	--	--	1.988	1.983	--	--	--
Fe4–O8	1.978	2.043	2.020	1.993	2.074	--	--	2.029	1.995	2.097
Fe1--Fe2	3.532	3.693	3.662	3.808	3.510	3.510	3.517	3.539	3.488	3.621
Fe3--Fe4	3.532	3.674	3.701	3.672	3.510	3.513	3.531	3.539	3.488	3.621
Fe1--Fe3	3.224	3.168	3.192	3.286	3.108	3.369	3.385	3.580	3.586	3.612
Fe2--Fe4	3.224	3.146	3.195	3.266	3.108	3.350	3.390	3.580	3.586	10.751
Fe1--Fe4	4.501	4.795	4.879	4.904	4.683	3.524	3.447	5.202	4.943	7.156
Fe2--Fe3	5.048	4.733	4.698	5.037	4.693	3.517	3.569	4.859	5.062	7.156

Table 4.3. Average Fe-O bond lengths with standard deviations (Å) determined from all tetranuclear structures shown in Table 4.2.

	Type 1	Type 2	Type 3
Alkoxide avg.	2.014	2.024	2.009
Alkoxide stdev.	0.029	0.030	0.014
Oxide avg.	1.793	1.803	1.796
Oxide stdev.	0.015	0.017	0.006
Carboxylate avg.	2.038		2.034
Carboxylate stdev.	0.031		0.069
Hydroxide avg.		2.008	
Hydroxide stdev.		0.038	

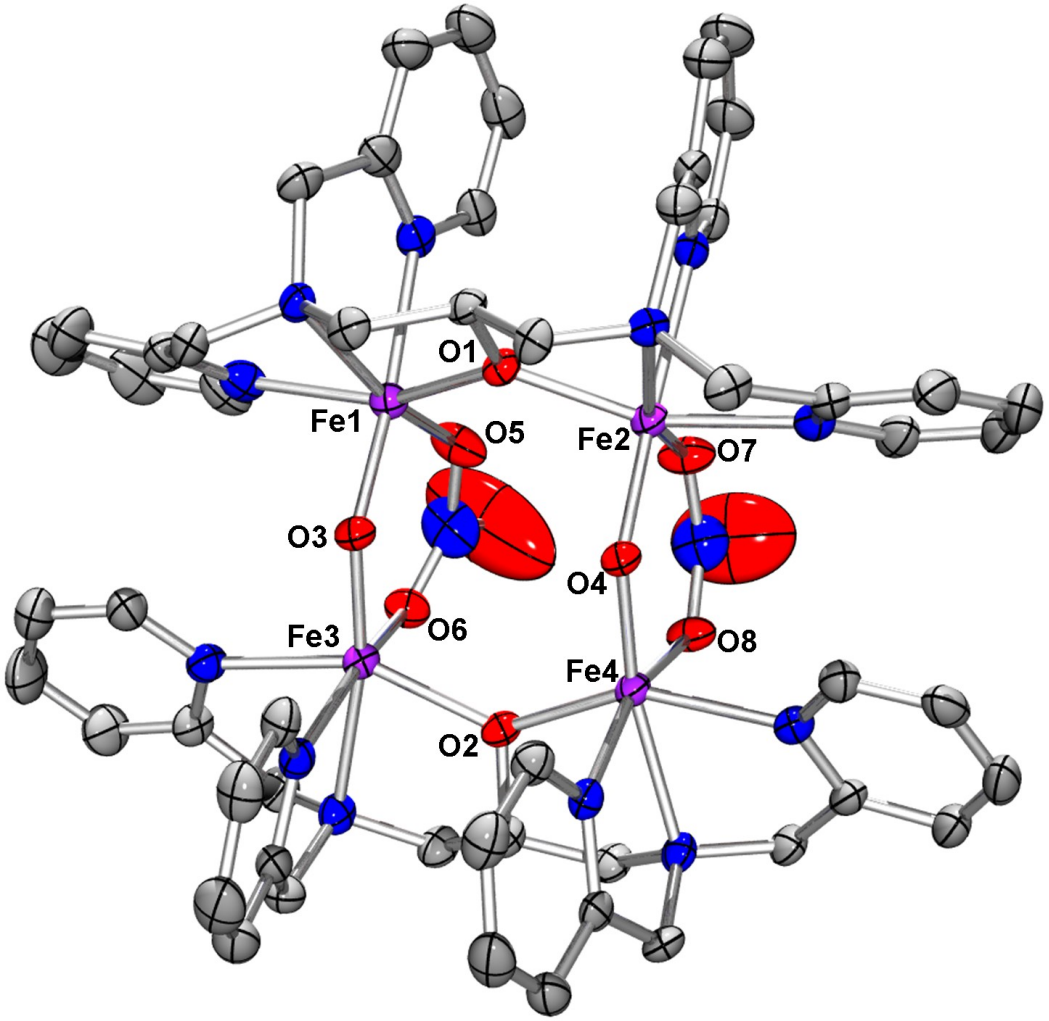

Figure 4.3. ORTEP representation of **4** with selected atoms labeled and hydrogen atoms removed for clarity.

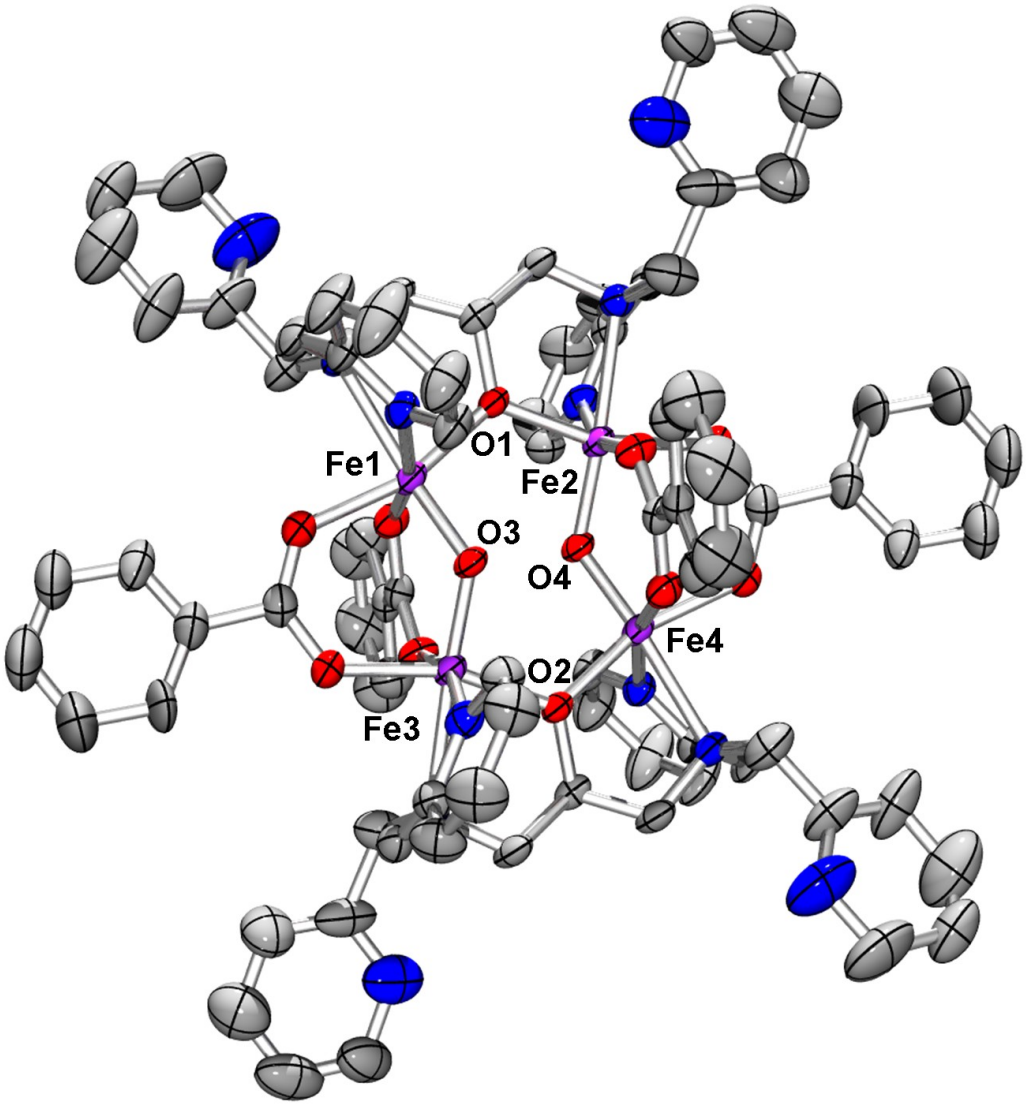

Figure 4.4. ORTEP representation of **5** with selected atoms labeled and hydrogen atoms removed for clarity.

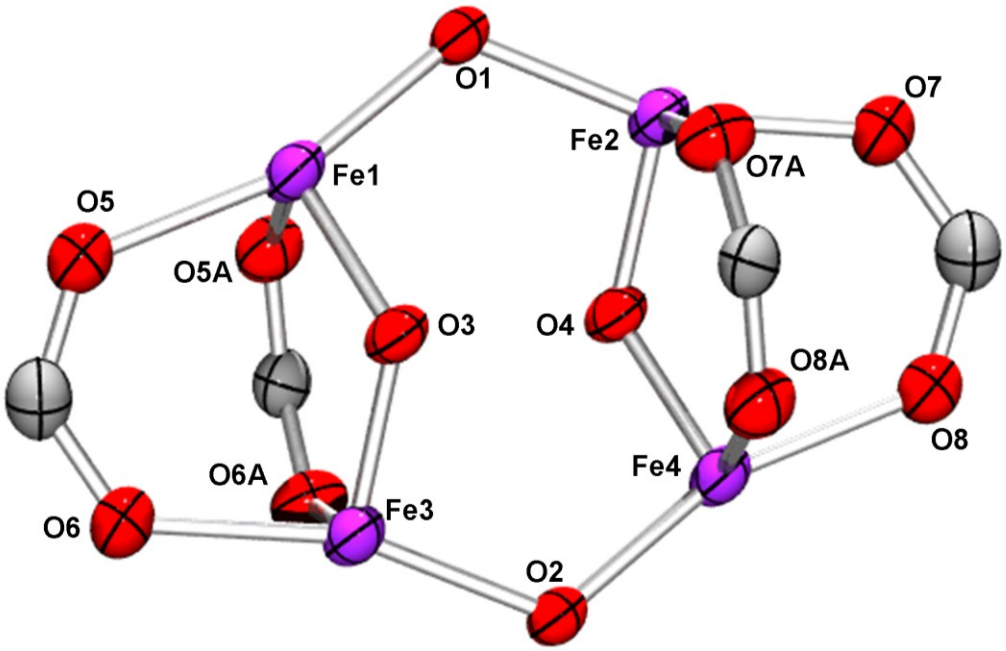

Figure 4.5. ORTEP representation of the tetranuclear center of **5** including only the iron and bridging atoms.

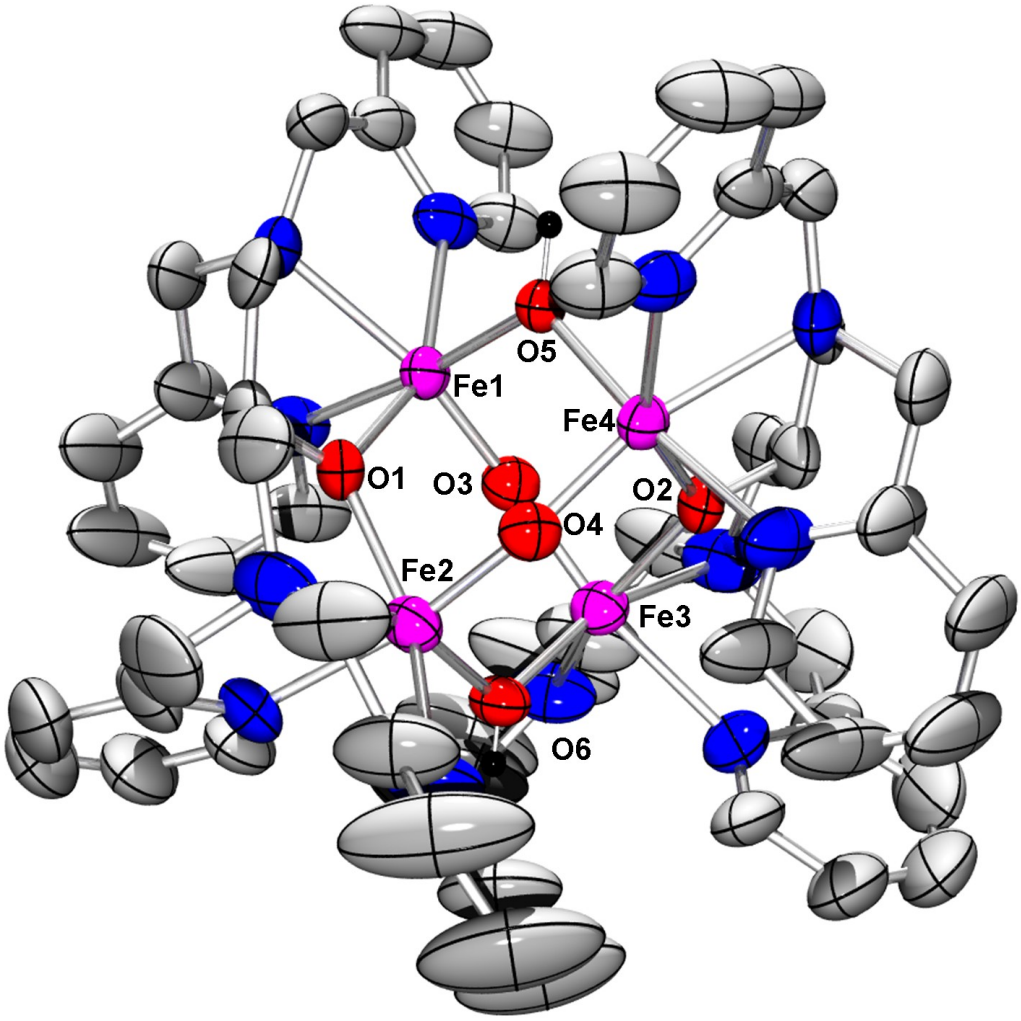

Figure 4.6. ORTEP representation of **6** with selected atoms labeled and hydrogen atoms removed from the HPTP ligand for clarity. The hydrogen atoms on the hydroxide oxygen atoms (O5 and O6) are black. Note the large ellipsoids indicative of disorder in the bottom most pyridyl ring.

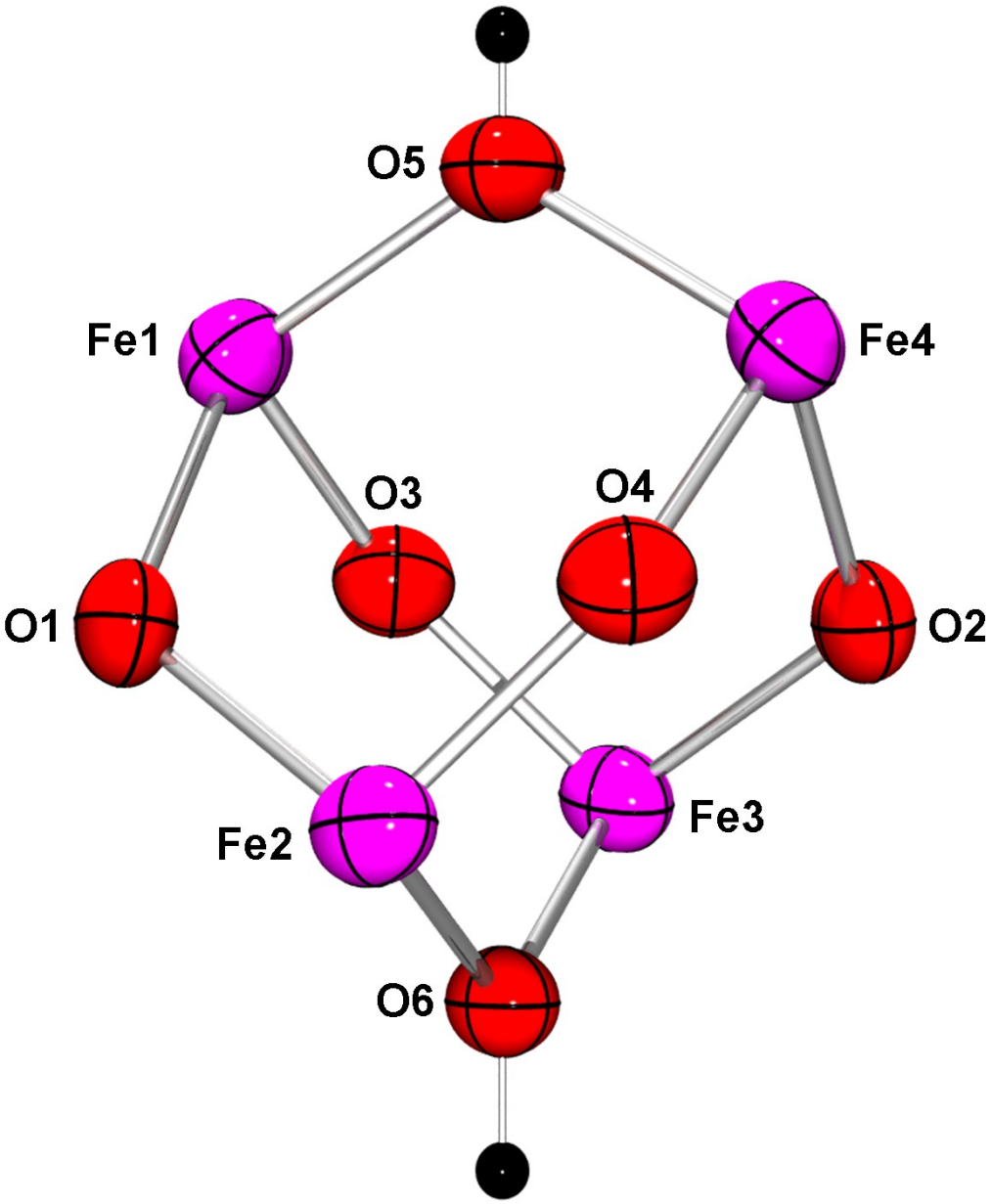

Figure 4.7. ORTEP representation of the "adamantane" core of **6**.

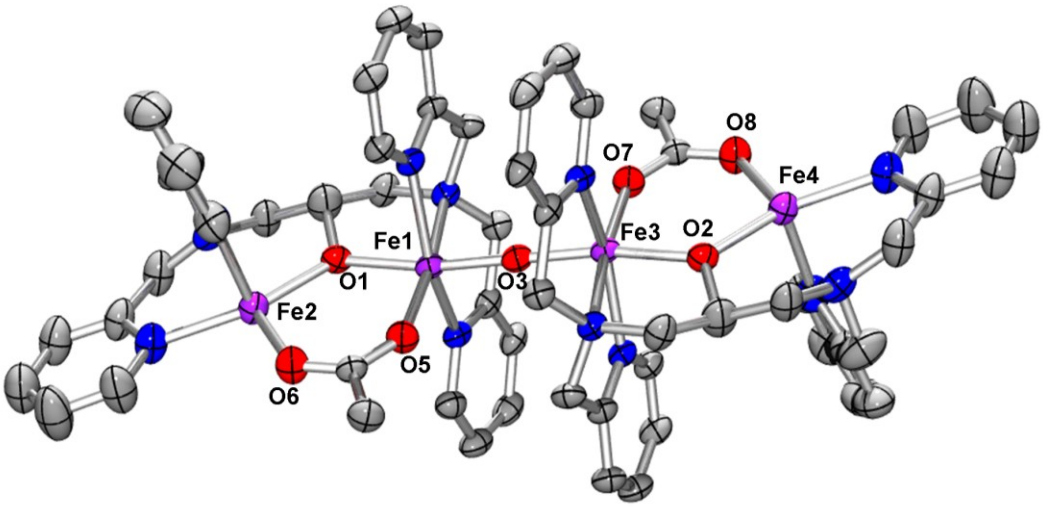

Figure 4.8. ORTEP representation of **7** with selected atoms labeled and hydrogen atoms and acetonitrile ligands removed for clarity.

The four new crystal structures presented here are all tetrairon clusters formed upon dimerization of diiron complexes synthesized using the dinuclear ligand HPTP (Figure 4.9). With the exception of two of the metal centers in **7**, all of the iron atoms are ferric. Prior to dimerization, each diiron HPTP complex contains an oxyanion acting as a three-atom bridge between the iron centers. The coordination modes of these oxyanions after dimerization are used to define three different basic structural types wherein: *(i)* the oxyanions rearrange to bridge the halves of the dimer, connecting iron centers ligated by separate HPTP moieties *(ii)* the oxyanions are replaced by something else and are no longer coordinated to iron atoms in the dimer, and *(iii)* the oxyanions retain their original positions bridging the iron centers ligated by a single HPTP moiety (Figure 4.2). As

structures of other molecules from other publications will be discussed in conjunction with the new ones presented here, it is important to create a standardized system for identification of the atoms in any given crystal, so it can be compared to other crystals of the same type. The labeling scheme for each type is shown in Figure 4.2. Crystallographic and refinement data for the new crystal structures are summarized in Table 4.1. Additionally, a summary of selected bond lengths and interatom distances for each of the complexes discussed is shown in Table 4.2.

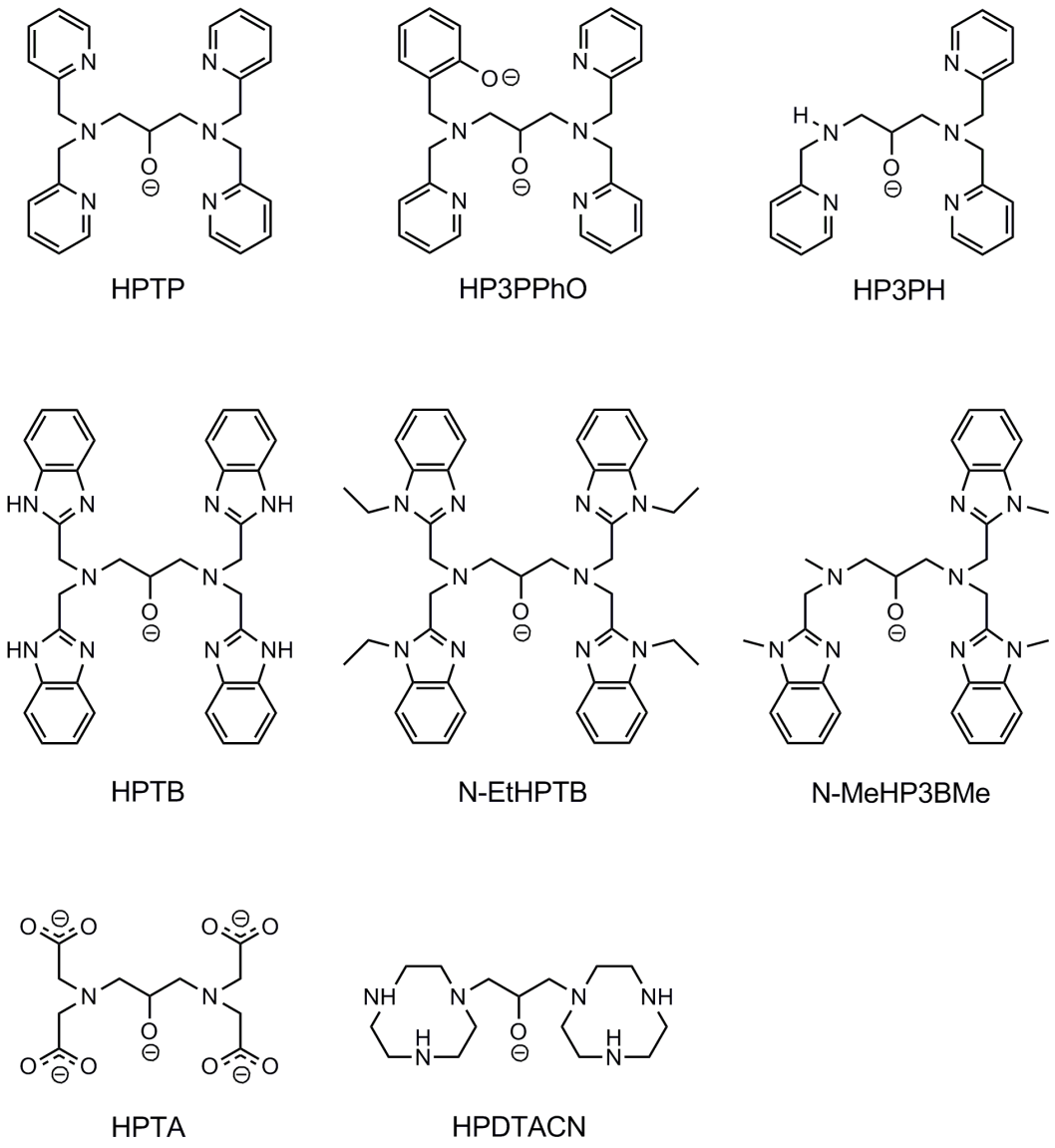

Figure 4.9. Representations of each ligand used to synthesize the complexes discussed in this chapter.

4 (Figure 4.3) and **5 (**Figures 4.4 and 4.5) are both Type 1 crystals (Figure 4.2), defined as molecules in which the oxyanions act as three-atom bridges between the halves of the dimers. The halves of **4** are bridged by two nitrate and

two oxide ions, resulting in a cation with a 4^+ charge. This charge is balanced by four perchlorate anions. Two of these ClO_4^- ions are disordered over two positions (89:11 and 52:48) in addition to one of the solvent molecules being disordered over two positions (70:30). Since the tetranuclear cation is the object of interest, the disorder in the counteranions and solvent is of no consequence. On each ligand, two of the pyridylmethyl substituents are aligned roughly parallel to the propane backbone and the remaining two are approximately perpendicular to that plane, both protruding on the same side of the plane. The planes produced by the propane backbone/pyridylmethyl substructure of each half of the dimer are approximately parallel, with the protruding pyridylmethyl groups of each half pointing in opposite directions. This gives the molecule an S-shape when viewed down the axis formed by the bridging oxides. Each bridging nitrate combines with a bridging oxide to form a six-membered ring consisting of two iron atoms and one nitrogen atom, alternating with oxygen atoms. Since it is not bonded to any atom other than a single nitrogen, the terminal nitrate oxygen atom exhibits considerable thermal motion.

The halves of **5** are bridged by four benzoate and two oxide ions, resulting in a cation with a 2^+ charge. This charge is balanced by two tetraphenylborate anions. One of the benzoate bridges is disordered over two positions (74:26) in addition to one of the nonligated pyridylmethyl groups being disordered over two positions (74:26). The identical disorder proportions indicate that a change in

position of one bridge correlates perfectly to a change in position of a pyridylmethyl substituent. The propane backbone is disordered over two positions (48:52). Additionally, one of the BPh_4^- ions is disordered over three positions (48:21:31). As with **4**, we are only concerned with the tetranuclear cation, so the disorder in the counterion can be discounted. Also, since the disorder in the cation does not affect any Fe-O bond lengths or Fe-Fe interatom distances, it is of little consequence. As noted in the experimental section, the amount and composition of solvent in the structure is not accurately known, but since the cation is the matter of interest, the disordered solvent will be ignored. The cation is a dimer of dimers, with all of the iron centers in identical environments. The two extra bridging benzoate ions make this molecule unique in the Type 1 category. Ligation of the extra benzoate bridges was possible, because one pyridylmethyl ligand on each iron center had come free. Each carboxylate is bidentate, forming six-membered rings consisting of two iron atoms and one carbon atom, alternating with oxygen atoms; the third oxygen atom is the bridging oxide. Eight-membered rings are also formed by each set of two benzoate bridges and the two iron atoms they connect. When the molecule is viewed along the alkoxide axis, the benzoate bridges form two wedges, pointing obliquely at each other. On each propane backbone, the ligated pyridylmethyl groups are on opposite sides of the roughly planar structure formed by the backbone and iron atoms. However, a mirror plane on the bridging oxide axis

reflects the ligated pyridylmethyl groups on one half of the dimer into positions proximal to the corresponding groups on the other half of the dimer. Every atom in one half of the dimer is related to the corresponding atom on the other half through a symmetry transformation (-x + 2,-y,-z).

The only new compound representative of Type 2 complexes (Figure 4.2) is **6** (Figures 4.6 and 4.7). Type 2 complexes consist of molecules in which no three-atom oxyanion bridging moiety is present. The halves of **6** are bridged by two hydroxide and two oxide ions, resulting in a cation with a 4^+ charge. This charge is balanced by four perchlorate anions. Additionally, the unit cell contains one water molecule, the hydrogen atoms of which are not included in the structure solution. One of the ClO_4^- ions is disordered, but as with both **4** and **5**, the tetranuclear cation is the object of interest, so the perchlorate disorder and the unmapped hydrogen atoms on the included water molecule are of no concern. The loss of the bridges originally between the iron centers leads to formation of an "adamantane" core, composed of four iron atoms and six oxygen atoms. Two oxygen atoms come from the ligand alkoxides, two are bridging oxides and two are bridging hydroxides (Figures 4.2 and 4.7). In each half of the dimer, two pyridylmethyl groups are aligned with the propane backbone along a gentle curve. The remaining two pyridylmethyl groups extend perpendicularly to the outside of this arc. To produce the dimer, one dinucleated HPTP ligand can be reflected and

rotated approximately ninety degrees. Addition of oxide and hydroxide bridges completes the structure.

By default, **7** (Figure 4.8) falls into the Type 3 category (Figure 4.2) by virtue of the fact that oxyanions forms three-atom bridges between the iron atoms ligated by each HPTP moiety. The halves of **7** are bridged by a single oxide ion. Each half of the dimer contains two metal centers, which are bridged by an acetate ion. The iron atoms are in two oxidation states (two ferrous and two ferric), resulting in a cation with a 4^+ charge. This charge is balanced by four tetraphenylborate anions. Finally, the sixth coordination site on each of the non-oxide-bridged atoms is filled by acetonitrile. As with **5**, the amount and composition of solvent in the structure is not accurately known, but since the cation is the matter of interest, the disordered solvent will be ignored. **7** is unique in two respects. It is the only one of these structures to contain metal centers in various states of oxidation. It is also the only one of these structures with a single oxide bridge linking the halves of the dimer. The single oxide bridge allows the molecule to stretch out in a linear fashion. The iron centers and the bridging oxide form a rough axis. On each dinuclear ligand, the propane backbone, the acetate bridge and one of the pyridylmethyl groups lie in a rough plane parallel to this axis. The remaining pyridylmethyl groups and acetonitrile ligands are nearly perpendicular to this plane. Each dinuclear ligand lies on the opposite side of the axis. Each acetate ion is coordinated to two iron atoms, forming a six-membered

ring consisting of two iron atoms and a carbon atom alternating with oxygen atoms. Every atom in one half of the dimer is related to the corresponding atom on the other half through a symmetry transformation (-x + 1,-y + 1,-z + 2).

4.4 Discussion

In recent years, interest in discovery and characterization of oxygen-activating diiron enzymes grown.[1,3,5-10] Unfortunately, Although some of the intermediates in the catalytic cycles of these biological systems have been characterized,[11-19] many are too transient to be trapped and studied. Synthetic chemists address this problem by producing diiron(II) complexes designed to mimic natural active sites.[20-29] A commonly employed ligand backbone used in these syntheses is an *N,N,N',N'*-tetrasubstituted 1,3-diaminopropan-2-ol moiety. For this work, we will focus on amine substituents containing nitrogen as the coordinating atoms. Adding these substituents results in ligands that can bind two iron atoms using a 3N1O binding motif for each nucleus. Affixing a bridging anion to this moiety produces a complex with two five-coordinate iron atoms (Figure 4.1).

The diiron(III) complexes usually formed upon reaction of these complexes with oxidants often dimerize into tetranuclear iron(III) clusters with six-coordinate iron centers. Examination of crystals of these species allowed us to classify them by where the number and locations of oxyanions acting as three-atom bridges. This resulted in three general types in which: *(i)* oxyanions act as

bridges connecting iron atoms coordinated by separate *N,N,N',N'*-tetrasubstituted 1,3-diaminopropan-2-ol-based ligands, *(ii)* there are no three-atom oxyanion bridges present, and *(iii)* the oxyanions form three-atom bridges between the iron centers ligated by one *N,N,N',N'*-tetrasubstituted 1,3-diaminopropan-2-ol backbone (Figure 4.2).

4.4.1 Type 1

Substances in which the oxyanions bridge the halves of the dimer are the most common type. However, of the five crystals of this type discussed here, only one was formed using a ligand that exhibits the 3N1O binding motif. One of the other four complexes has one iron center which is ligated in a 2N2O motif, two others contain one iron center ligated in a 2N1O motif and in the final compound both iron centers are ligated in a 2N1O motif.

The first of these five substances (**QOLJUW**)[91] was formed using HP3PPhO (Figure 4.9), a modified HPTP ligand in which one of the pyridylmethyl substituents is replaced with a methylphenolate group. The second compound (**JUJMAC**)[92] was formed using N-MeHP3BMe (Figure 4.9), a modified N-MeHPTB ligand in which one of the N-methyl-methylbenzimidazolyl substituents is replaced with a methyl group. The literature contains characterizations of over a dozen tetranuclear crystals formed using HPTA (Figure 4.9),[93-98] a ligand synthesized by placing acetic acid substituents on the *N,N,N',N'*-tetrasubstituted 1,3-diaminopropan-2-ol backbone, compared to only

three made using forms of methylbenzimidazole as the amine substituents (HPTB and N-EtHPTB, Figure 4.9),[65] one of which has fluoro rather than hydroxo bridges.[99] While this surplus of HPTA complexes is by no means proof that neutral, bulky substituents interfere with tetranuclear complex formation, it may point in that direction. The oxo-bridges connecting the halves of the dimer form "strings" connecting iron atoms which are located at the bottoms of two bowls formed by the amine substituents (the bulkier the substituents, the deeper the bowls). During dimer formation, either the bowls are semi-nested or the lips are pressed together. In either case, deeper bowls produce longer strings. Since the Fe-O-Fe bridges can only stretch so far, it stands to reason that bulky substituents inhibit dimer formation. More evidence of this is the fact that in the only carboxylate-bridged dimer formed using methylbenzimidazole substituents, one of them has been replaced with a methyl group, which takes up very little space and is not even ligated to the iron center. In this rare case, the iron center in question is not saturated, being connected to only five atoms.

The third of these complexes in which the oxyanions bridge the dimer (**GUNDUO**)[100] was also formed using a modified HPTP ligand, HP3PH (Figure 4.9). In this case, one of the pyridylmethyl groups is replaced with a hydrogen atom. However, instead of being unsaturated in the tetranuclear form like **JUJMAC**, the iron center associated with this hydrogen substituent ends up with six ligands, the sixth being a water molecule. This solvent may bind to the iron

center, because **GUNDUO** is less sterically hindered than **JUJMAC** in two ways. Instead of methylbenzimidazolyl substituents, **GUNDUO** has pyridylmethyl groups. Also, one of the four substituents is replaced with a hydrogen atom instead of a methyl group, as in the case of **JUJMAC**. Both of these facts may account for the ability of solvent to coordinatively saturate the iron centers of **GUNDUO** and the inability to do the same to the unsaturated centers of **JUJMAC**.

The fourth complex (**5**) is unique in being the only Type 1 crystal in which the halves of the dimer are bridged by four carboxylates instead of two. In this case, one pyridylmethyl group comes loose from each iron center. Upon formation of the dimer, these empty coordination sites are individually occupied by one end of one of two benzoate bridges.

The fifth of these complexes (**4**) is bridged not by benzoate, but by nitrate. This is the only crystal of these five which was formed using unmodified, completely ligated HPTP. Because one pyridylmethyl group on each iron center comes free during formation of **5** (which was also formed using unmodified HPTP), the iron centers of both **4** and **5** are in duplicate environments within each respective complex. There is no difference the Fe-alkoxide bond lengths in each half of **5** and those in **4** fall within 0.002Å of each other. Those same bond distances vary from each other by as little as 0.003Å and as much as 0.068Å in the other complexes, with **GUNDUO** varying the least and **JUJMAC** the most.

Interestingly, the Fe-alkoxide bond lengths in **GUNDUO** are more symmetric than those in **QOLJUW**. This may be due to fact that the former has a water molecule in place of a methylpyrdine, whereas the latter sees that pyridine replaced by a phenolate. Although the phenolate is structurally more similar to pyridine than is water, in this case, substituent charge difference appears to play a more significant role than size similarity.

The amount of variation in Fe-oxide bond lengths follows almost the same pattern as the Fe-alkoxide bond lengths. **4** is the most symmetric, followed closely by **GUNDUO** and then **5**, with **QOLJUW** being the least symmetric, showing again that dimers formed using modified, unsymmetric ligands come together in an awkward fashion.

The interiron distances on each half of a dimer should be the same if the dimer is perfect. However, with the exceptions of **JUJMAC** and **5**, that is not the case for these complexes. In fact, the variation in interiron distances for each half of the dimer is greatest for **4** (0.136Å), followed by **GUNDUO** (0.039Å) then **QOLJUW** (0.019Å). Excluding **5**, the Fe-oxide bond length variations trend in exactly the opposite order as those of the Fe-alkoxide bonds.

Since the halves of both **JUJMAC** and **5** are related through symmetry transformations (-x,-y + 1,-z + 1 and –x + 2,-y,-z, respectively), the respective interiron distances within each complex are duplicates. However, this distance perfection only applies to interiron distances when they are seen as forming the

sides of a parallelogram. While the lengths of opposite sides of the parallelogram are perforce the same, diagonals connecting opposite corners are not necessarily so. This holds true for **JUJMAC** and **5** as well, where we see diagonal interiron distances which vary by 0.547 and 0.010 Å, respectively. The variations in these distances for these and other compounds do not correlate with the previous trends in any way.

4.4.2 Type 2

Both structures of this type have four bridges between the halves of the dimer, two oxides and two hydroxides. These bridges, in conjunction with the *N,N,N',N'*-tetrasubstituted 1,3-diaminopropan-2-ol-based alkoxides and iron centers, form an "adamantane" core (Type 2 in Figure 4.2). There are no published structures of this type which were formed using bulky substituents on the *N,N,N',N'*-tetrasubstituted 1,3-diaminopropan-2-ol backbone. Two have been synthesized using HPTA,[96,98] but the two we will discuss were created with each iron center originally bound in the 3N1O motif. The first of these substances (**6**) was formed using HPTP. The second (**LAXNIH**)[101] was formed using an unusual ligand, HPDTACN (Figure 4.9), wherein the terminal nitrogen atoms on the propane backbone are part of triazacyclononyl rings. Use of this ligand results in a complex with 3N1O ligated metal centers without the extraneous ligand bulk produced through the use of larger substituents (e.g. pyridylmethyl or methylbenzimidazolyl groups). The nature of the "adamantane" core forces the

propane backbone of one half of the dimer to be approximately perpendicular to the backbone of the other half. Turning the backbones at right angles allows the iron centers to occupy the termini of a tetrahedron, instead of being forced into a plane, as is the case with Type 1 structures. This perpendicularity relieves some of the strain produced by forcing the dinuclear ligands into close proximity, although the distance between the iron centers from one half of the dimer to the other is greater than in any of the Type 1 complexes (a minimum of 3.350 Å for Type 2 compared to a maximum of 3.286 Å for a non-diagonal interiron distance for Type 1). However, the interiron distances of Type 2 complexes are much more consistent than those of Type 1 structures. This consistency applies not only to individual members of the Type 2 class, but also to the class as a whole. The interiron distances (including diagonals) for both Type 2 complexes range from 3.350 Å to 3.569 Å, a difference of only 0.219 Å. In contrast, Type 1 complexes have interiron distances (including diagonals) ranging from 3.146 to 5.048 Å, a difference of 1.902 Å. It is apparent that removing the planar restriction in Type 1 complexes which forces the iron atoms into parallelograms also removes significant steric interference, allowing the interiron distances of Type 2 complexes to fall into a narrow range, even taking into account diagonal distances.

Although both Type 2 structures contain symmetric ligands, neither contains any atoms related through symmetry transformations. The alkoxide Fe-O bonds of **6** vary by as much as 0.037 Å while those of **LAXNIH** vary by as

much as 0.081 Å. Oddly, in the Type 1 complex with the most distorted alkoxide bonds (**JUJMAC**), these same bonds vary by only 0.068Å. **JUJMAC** was synthesized using N-MeHP3BMe, a quite unsymmetric ligand, especially compared to those used to create **LAXNIH** and **6** (HPDTACN and HPTP, respectively). The Fe-oxide bonds of **6** vary by 0.020 Å while those of **LAXNIH** vary by as much as 0.058 Å. Once again, the Type 1 complex with the most distorted bond of this type (**QOLJUW**) was synthesized with an unsymmetric ligand (H3PPhO) and once again, those bond distances vary by less (0.043 Å) than those of the worst Type 2 complex. It appears that while the parallelogram structure evident in Type 1 complexes does not allow for consistent interiron distances, it does allow for consistent Fe-O bonds, both oxide and alkoxide. However, it is important to note that although Type 2 complexes display more variation in oxide and alkoxide bond lengths than Type 1 structures, within error the averages of those lengths are the same for both types (Table 4.3).

4.4.3 Type 3

The third type of structure includes substances in which an oxyanion forms a three atom bridge between the iron atoms ligated by a single *N,N,N',N'*-tetrasubstituted 1,3-diaminopropan-2-ol backbone. Two examples of this phenomenon are **GIJDUY** and **GIJFAG**.[65] Both of these complexes contain benzoate bridges between the iron centers in each half of the dimers. They also have two Fe-O-Fe bridges linking the halves of the dimers. **GIJDUY** was

synthesized using HPTB while **GIJFAG** was created using N-EtHPTB (Figure 4.9). The third member of this group (**7**) was created using HPTP with acetate bridges linking the dinuclear iron centers. As mentioned earlier, this third structure falls into the Type 3 category only because it has a carboxylate moiety acting as a three-atom bridge between the iron atoms ligated by each dinuclear ligand. However, the iron centers are in two oxidation states and there is only one oxide bridge holding the dimer together.

GIJDUY and **GIJFAG** are the only structures discussed in this paper that were synthesized using methylbenzimidazolyl groups for all of the amine substituents. It is possible that the steric bulk of these substituents forced the complexes to adopt the unique geometries they exhibit. The structures of both of these crystals are very similar, so the following observations can be applied to both of them. Rotation of one dinuclear ligand and the attached benzoate bridge about an axis drawn through the bridging oxides produces the second half of the dimer. The benzoate ion, the propane backbone and the methylbenzimidazolyl groups proximal to the axis are also parallel to it. They form rough planes that allow the dimer halves to approach each other without excessive steric interference. The remaining methylbenzimidazolyl groups are perpendicular to these planes, distal from the oxide axis. This oxide-only bridging geometry may be preferred, because rearrangement of a benzoate bridge to become a bridge holding the dimer together would necessitate rotation of a dinuclear ligand on its

iron axis to move the propane backbone away from the encroaching aromatic ring. If the second benzoate bridge then moved to become a dimer bridge, the other dinuclear ligand would also have to rotate to avoid the aromatic ring. This rotation would bring would put the moving propane backbone in close proximity to the other benzoate bridge, causing excessive steric problems. It is possible that these steric issues would prevent the formation of a Type 1 complex, and this may be the reason that the only fully formed Type 3 crystals have been formed with bulky ligands.

With this in mind, it is possible that **7** is not fully formed and may in fact be an intermediate on the path to formation of a Type 1 or Type 2 complex. It is the only singly oxide-bridged tetrairon crystal synthesized using ligands formed with the *N,N,N',N'*-tetrasubstituted 1,3-diaminopropan-2-ol backbone. Assuming it crystallized as an intermediate between the dinuclear and tetranuclear species, its structure might lend insight into how these transformations take place. Further evidence that it appears to have crystallized mid-reaction comes in the form of two oxidation states. This mixed valence complex could certainly be on its way to becoming a fully oxidized tetranuclear ferric species.

Following this line of thought, we need to examine the structure of **7** more closely. The assignment of O3 as an oxide is supported by the bond lengths between it and both Fe1 and Fe3. A bond length of 1.804 Å between a ferric center and an oxide is typical for complexes of this type (Table 4.3). However, if

Fe1 and Fe3 are assumed to be ferrous, to balance the molecular charge, O3 would have to be part of a water molecule. This is unreasonable, because the bond between high-spin ferrous iron and water would be much longer, in the range of 2.2 to 2.3 Å. Additionally, if O3 were part of a hydroxide ion, to balance the molecular charge, only one iron atom in the molecule would be ferric. This atom would have different bond distances to corresponding ligands than those of its ferrous counterpart. The halves of this dimer are related through a symmetry transformation, indicating that Fe1 is the same as Fe3 and that Fe2 is the same as Fe4. If only one iron atom were to be in a different oxidation state, it could not be equivalent to any of the others. Since we are presented with two sets of duplicate iron centers, we must assume that the members of each set are in the same oxidation states.

4.5 Summary and Conclusions

In this chapter, we discussed various forms of tetranuclear iron(III) complexes that form upon oxidation of diiron(II) precursors synthesized using ligands with *N,N,N',N'*-tetrasubstituted 1,3-diaminopropan-2-ol backbones. The complexes were separated into three categories. These classes include structural motifs wherein: *(i)* oxyanions act as three-atom bridges the halves of the tetranuclear dimer, *(ii)* the halve of the tetranuclear cation are bridged by oxides and hydroxides and *(iii)* oxyanions form bridges between the iron centers ligated by a *N,N,N',N'*-tetrasubstituted 1,3-diaminopropan-2-ol backbone (Figure 4.2).

There are many tetrairon(III) crystals formed using this backbone with charged amino substituents (e.g. acetate). This introduces electronic effects that were not examined in detail, as this work focused on amine substituents which coordinate to the iron centers using neutral nitrogen ligands. We reported an unusual nitrato-bridged complex and a unique mixed-valent diiron(II)-diiron(III) crystal. Our analysis of the crystallographic data presented here leads us to conclude that the steric bulk present in the amine substituents is the primary reason the tetranuclear cation of a given complex crystallizes in one of three basic structural motifs. Further work examining electronic effects produced by charged amine substituents may be necessary to confirm this premise.

4.6 Acknowledgements

This work was supported by the National Institutes of Health through Grant GM-38767. We thank Dr. Victor Young, Jr. of the X-ray Crystallographic Laboratory at the University of Minnesota for his invaluable assistance. We are also grateful to Clyde Cady for providing some of the crystals discussed in this chapter.

Chapter 5: Resonance Raman Investigation of Fe(IV)=O Stretching Frequencies

5.1 Introduction

There exists a vast number of nonheme oxygen-activating monoiron enzymes encompassing dioxygenases, lipoxygenases, hydroxylases and synthases.[4,32] The oxoiron(IV) intermediates commonly present as the oxidative species in biological catalytic cycles are of interest, because they may be used as templates for synthetic chemists attempting to create industrially applicable catalysts. For this reason, various synthetic complexes have been produced in efforts to copy these natural systems.[33] A prerequisite for designing better biomimetic molecules is an understanding of how ligand structure and electronic properties affect the active species, the oxoiron(IV) intermediates. For this reason, characterization of oxoiron(IV) species is an important part of the study of synthetic monoiron systems.

With varying degrees of success, chemists have been using resonance Raman (rR) spectroscopy to examine vibrational properties of oxoiron(IV) intermediates. Unfortunately, most oxoiron(IV) species do not have visible chromophores, making successful collection of rR spectra of these intermediates a relative rarity.[34-39] In this chapter, we will discuss the reasons for these difficulties. Following that, we will detail a new method for capturing rR spectra of oxoiron(IV) adducts which addresses these problems and show the results produced by its application.

5.2 Experimental Section

5.2.1 Materials and Syntheses

All solvents were purchased from commercial sources and were used as received, unless noted otherwise. They were dried according to published procedures and distilled under Ar prior to use.[42] The $^{18}OH_2$ (98%) used in labeling studies was purchased from ICON, Summit, NJ. Preparation and handling of air sensitive materials were carried out under an inert atmosphere by using either standard Schlenk and vacuum line techniques or a glovebox. All complexes used to produce the rR spectra shown here were synthesized by collaborators. As the aim of this chapter is to relate a spectroscopic technique and show the results there from, synthetic details will not be reported.

5.2.2 Physical Methods

Resonance Raman spectra were collected on an ACTON AM-506M3 monochromator with a Princeton LN/CCD data collection system using either a Spectra-Physics Model 2060 krypton laser or a Spectra-Physics Model 2066-7S argon laser. Low-temperature spectra of the peroxo intermediates were obtained at 77 K using a 135° backscattering geometry. Samples were frozen onto a gold-plated copper cold finger in thermal contact with a Dewar flask containing liquid nitrogen. Raman frequencies were referenced to the features of indene. Slits were set for a band-pass of 4 cm^{-1} for all spectra.

5.3 Results

Oxygen activating monoiron enzymes are of interest because they perform a wide variety of reactions, many of which could be catalytically useful on an industrial scale.[4,32] Synthetic complexes are often created to aid chemists in their investigations into the active sites of these enzymes.[33] Many of these complexes produce oxoiron(IV) intermediates as their active species. Understanding the nature of these moieties may lead to new or modified ligands intended to tune the chemistry of the oxidative intermediate. For this reason, resonance Raman (rR) spectroscopy has been used to investigate the properties of various Fe(IV)=O bonds.[34-39] As an investigative method, resonance Raman spectroscopy relies on laser excitation of electrons in charge transfer bands. This limits its effectiveness as tool for examining oxoiron(IV) intermediates, because they rarely have significant visible absorbance. Oxo-to-iron charge transfer bands in the near UV region have forced spectroscopists to use relatively high frequency lasers for excitation. The use of high-energy photons coupled with the inherent instability of oxoiron(IV) intermediates produces a host of problems.

It is virtually impossible to produce usable rR spectra of oxoiron(IV) moieties using UV lasers which excite directly into charge transfer bands. This is likely because the photons are high enough in energy to induce reduction of the highly oxidative species under examination. For this reason, most rR spectra of these complexes are undertaken using laser wavelengths around 400 nm. With

one exception, all of the spectra presented in this chapter were produced using a 406.7 nm laser line. This is the wavelength used for most oxoiron(IV) investigations, but it presents a different problem. While using a longer wavelength cuts down on the amount of photoreduction, it also lowers the signal intensity of the resonance enhanced vibrations, because the excitation wavelength is hitting the low-energy tail of the charge transfer band. This means that longer exposure times are necessary, which reintroduces the issue of photoreduction while addressing the signal-to-noise problem. Some chemists successfully dealt with this by reducing the power of the excitation laser and collecting spectra over extended periods using liquid samples.[34-36,38] However, many of the intermediates under investigation are not stable for hours in solution, so this technique could not be applied. Also, the low laser powers necessary to prevent photoreduction meant that many species with virtually no visible absorption did not experience significant signal enhancement, therefore no spectra of these complexes were available.

We present here a new method that addresses these problems and was used to produce rR spectra of intermediates that previously had not been successfully characterized using rR spectroscopy. Development of this method was a stepwise process, as we changed conditions to counter the problems presented by the old technique. Initially, we merely raised the concentration of the solution being examined. This was an attempt to counter the signal-to-noise

problem produced by excitation into the tail of the charge transfer band. In theory, increased concentrations should have produced more intense resonance enhanced signals, allowing us to separate them from background noise. In reality, we did not observe a signal-to-noise ratio any better than that produced using the old method. In fact, as the concentration was progressively increased, we saw a decline in signal intensity. The obvious conclusion was that the Raman-shifted photons being emitted by the sample were being absorbed by other non-solvent molecules due to their increased concentration.

This issue was addressed via the simple expedient of freezing the solution at 77 K using liquid nitrogen. In addition to focusing the laser on the surface of the sample, thus providing the emitted photons with an unblocked path to the monochromator, freezing the sample also prevented auto-decay, allowing us to utilize longer exposure times. However, this method did have one drawback. Because the sample was frozen in a matrix, only a small portion of the molecules in the sample was experiencing laser excitation. Over time, signal intensity would again fade. When in solution, the molecules exposed to the laser are in constant flux, meaning that even if a molecule is photoreduced, a different molecule will soon take its place in the beam. Because of this, photoreduction in solution sometimes becomes a problem only after an extended time. When using a solid sample, this effect is noticeable much sooner.

The final step in perfecting our new technique was to solve the photoreduction problem associated with prolonged exposure of the surface of a frozen sample. Rather than freezing a few drops on a cold finger, we opted to coat a flat surface with frozen material. This involves reducing the temperature of the cold finger to just above the freezing point of the solution. If the temperature drops below the freezing point of the solution before it is introduced to the cold finger, the liquid will ball up, freeze and fall off the mounting surface. Applying a very thin layer of solution to the cold finger then chilling it below the freezing point produces a frozen film. This film is too thin to be effectively used for spectroscopy, but more layer of solution can be added stepwise to build up the thickness. Careful application produces a frozen layer approximately one mm thick over an area of approximately one cm^2. By aligning the cold finger so the surface of the sample is in the focal plane of the monochromator, we are able to move the sample within that plane without losing focus. During the excitation period, the sample is kept in constant motion. This limits the loss of signal due to photoreduction, because unexposed sections of sample are constantly moving in the laser beam. Using this new method, we were able to produce rR spectra of a variety of oxoiron(IV) intermediates produced using the ligands shown in Figure 5.1. The Fe-O stretching frequencies of these complexes are summarized in Table 5.1 and the spectra are shown in Figures 5.2 to 5.17.

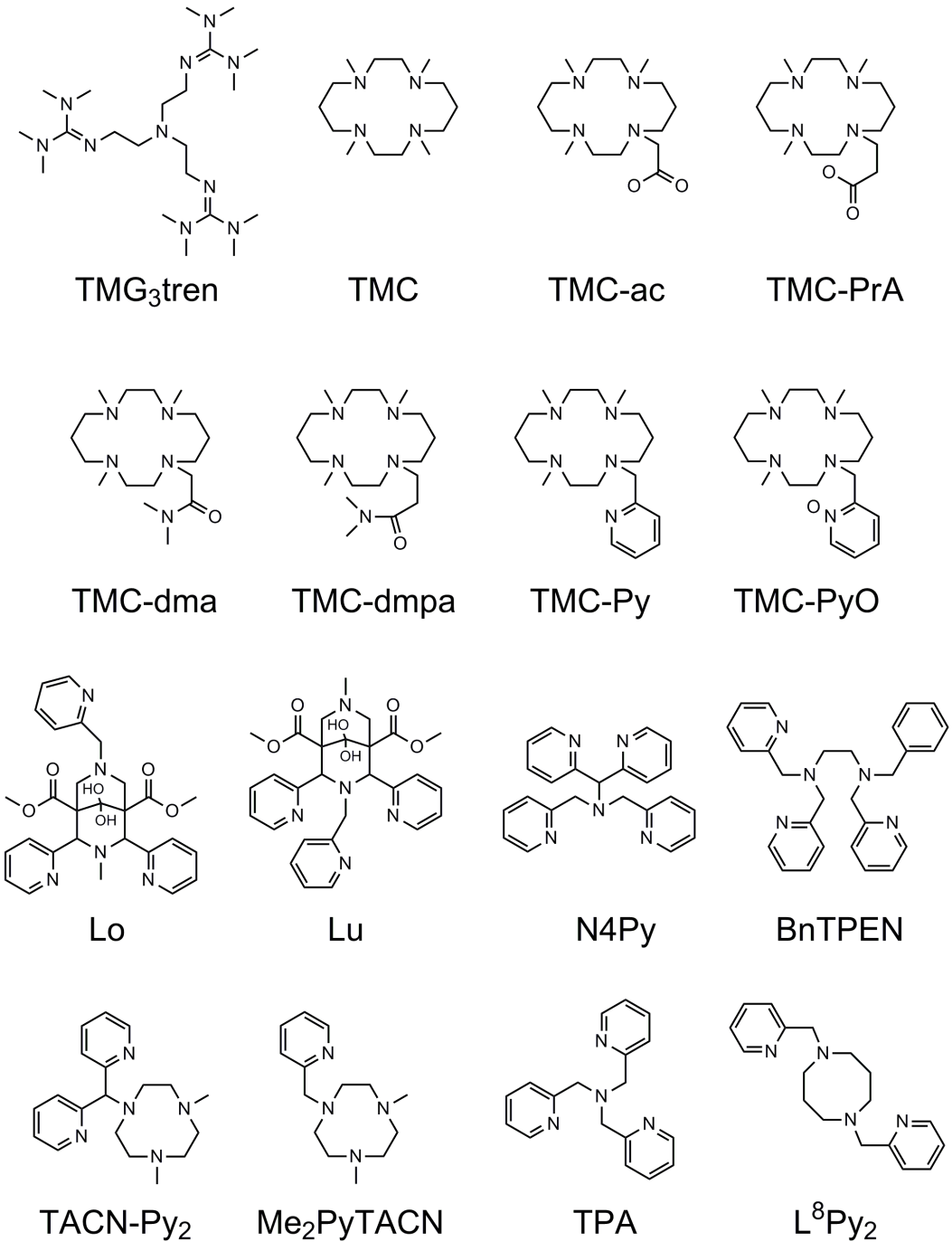

Figure 5.1. Ligands used to synthesize the oxoiron(IV) intermediates examined via resonance Raman spectroscopy.

Table 5.1. Fe-O stretching frequencies of oxoiron(IV) complexes determined in frozen MeCN using resonance Raman spectroscopy (values are in cm^{-1}).

Ligand	ν_{Fe-O} (^{18}O)	Calc. [a]
TMG_3tren	842 (810)	805
TMC [b]	824 (790)	788
TMC-ac	831 (791)	794
TMC-PrA	822 (790)	786
TMC-dma	834 (798)	797
TMC-dmpa	833 (798)	796
TMC-Py	824 (793)	788
TMC-PyO	829 (791)	793
Lo	825 (791)	789
Lu	840 (805)	803
N4Py	841 (806)	804
BnTPEN	835 (796)	798
TACN-Py_2	831, 847 (804)	802 [c]
Me_2PyTACN	831 (788)	794
TPA	833 (799)	796
L^8Py_2	834 (--) [d]	797

[a] Expected values predicted for an Fe-O oscillator by application of Hooke's law.
[b] Acetate added to solution (3 eq.).
[c] Value calculated from center of Fermi doublet at 839 cm^{-1}.
[d] Attempts to label this intermediate with ^{18}O were unsuccessful.

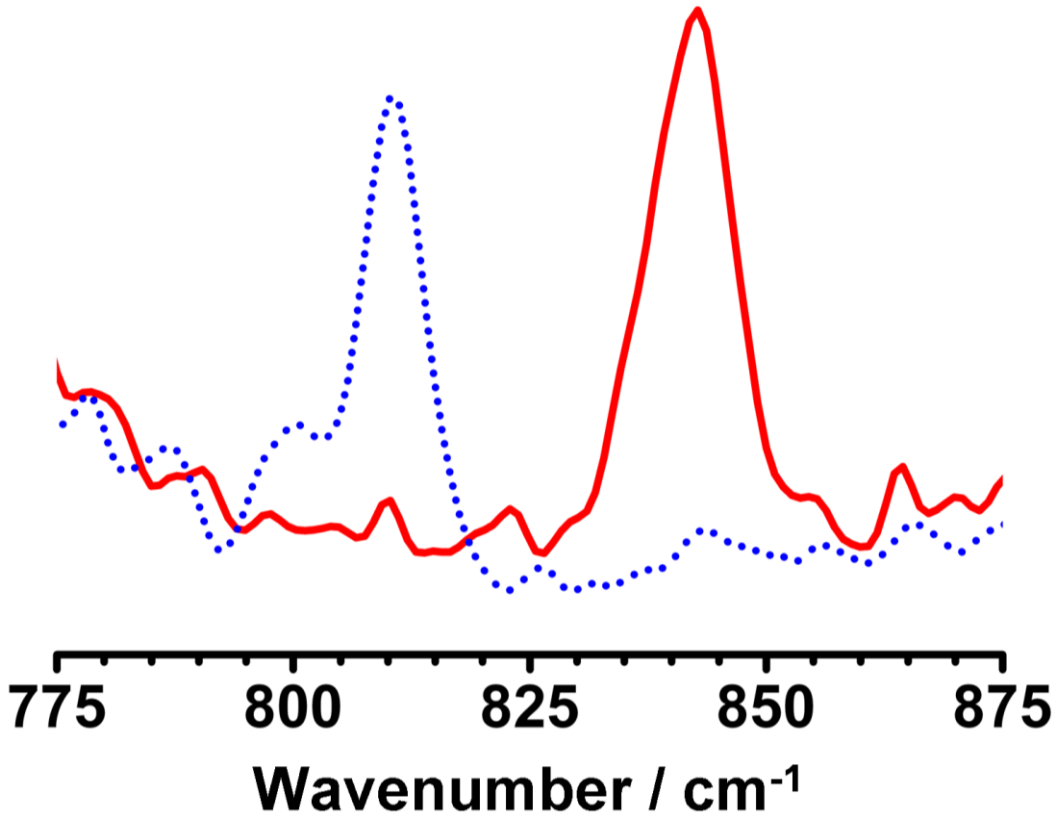

Figure 5.2. Resonance Raman spectra of oxoiron(IV) species produced using the ligand TMG_3tren (Figure 5.1). Solid red line = ^{16}O; dotted blue line = ^{18}O.

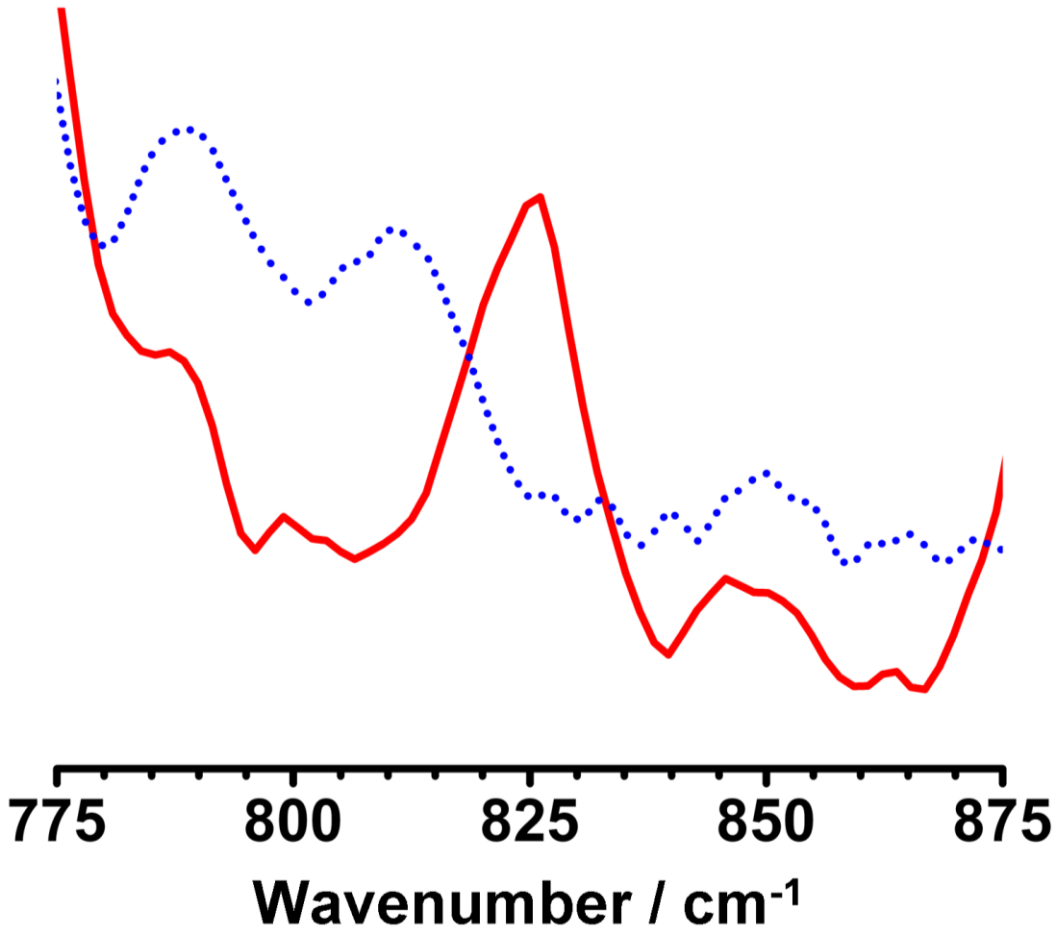

Figure 5.3. Resonance Raman spectra of oxoiron(IV) species produced using the ligand TMC (Figure 5.1) with 3 equivalents of acetate. Solid red line = ^{16}O; dotted blue line = ^{18}O.

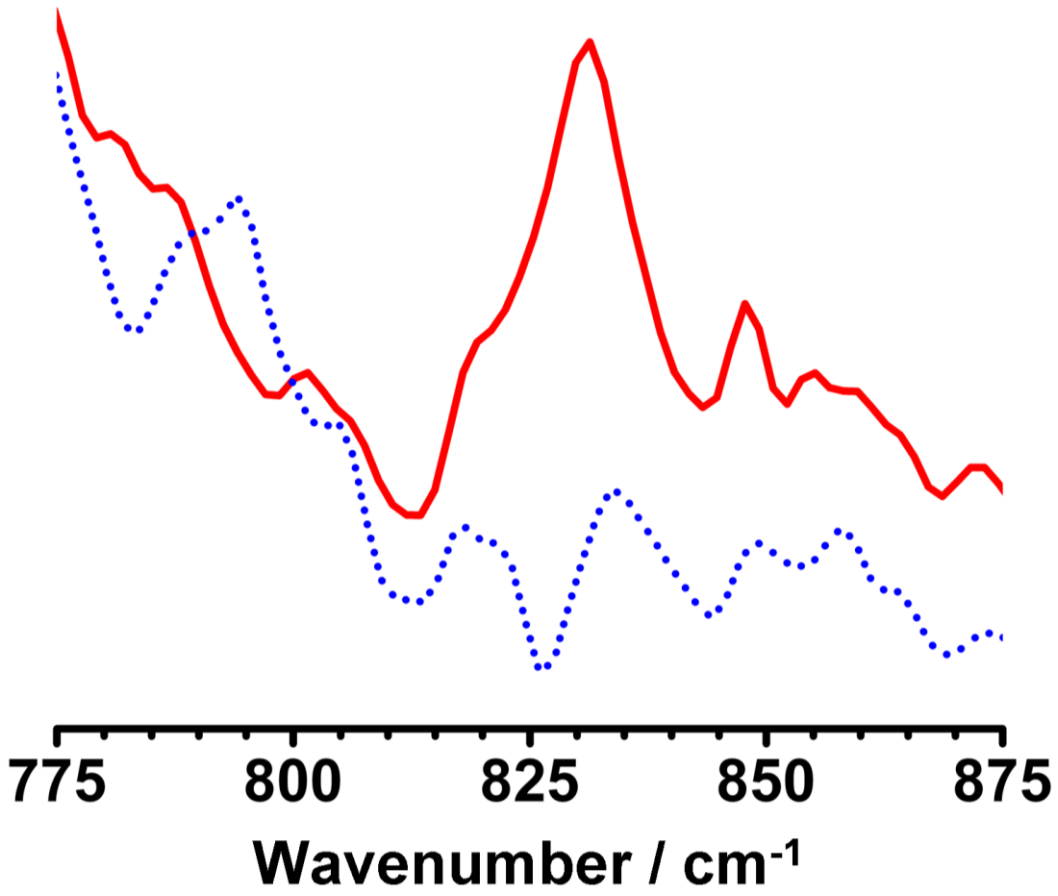

Figure 5.4. Resonance Raman spectra of oxoiron(IV) species produced using the ligand TMC-ac (Figure 5.1). Solid red line = ^{16}O; dotted blue line = ^{18}O.

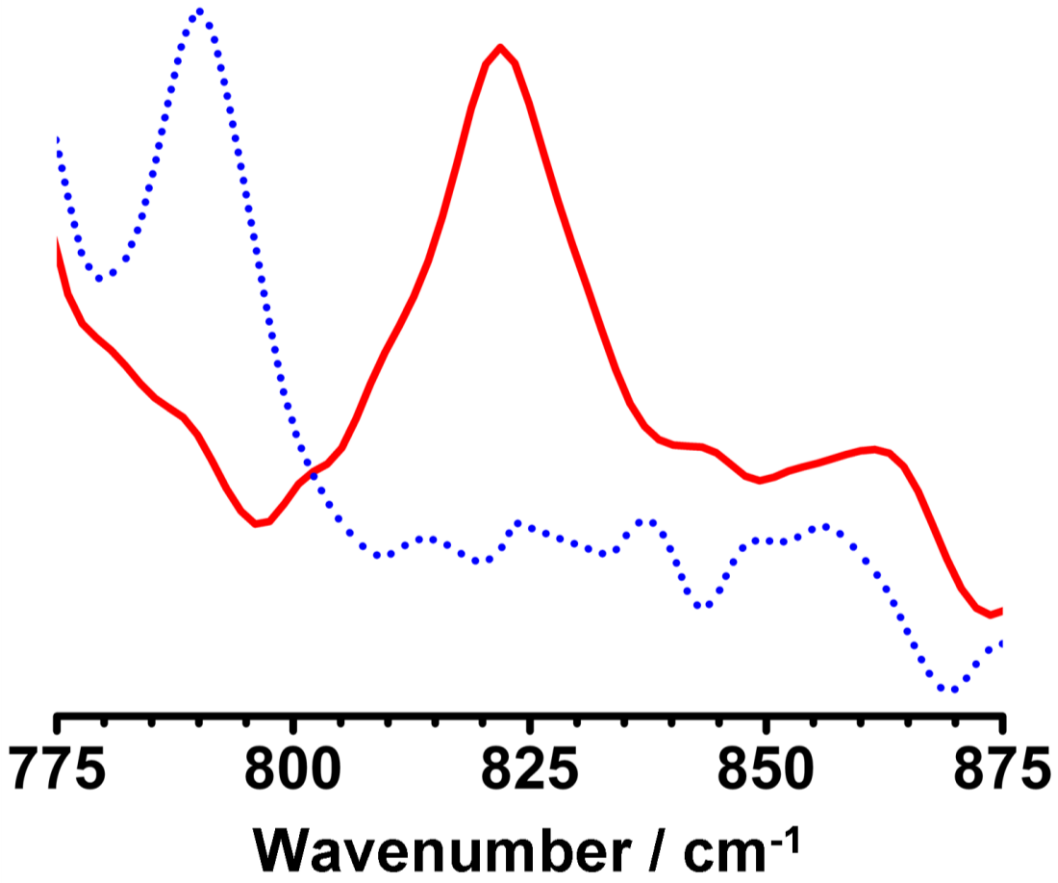

Figure 5.5. Resonance Raman spectra of oxoiron(IV) species produced using the ligand TMC-PrA (Figure 5.1). Solid red line = ^{16}O; dotted blue line = ^{18}O.

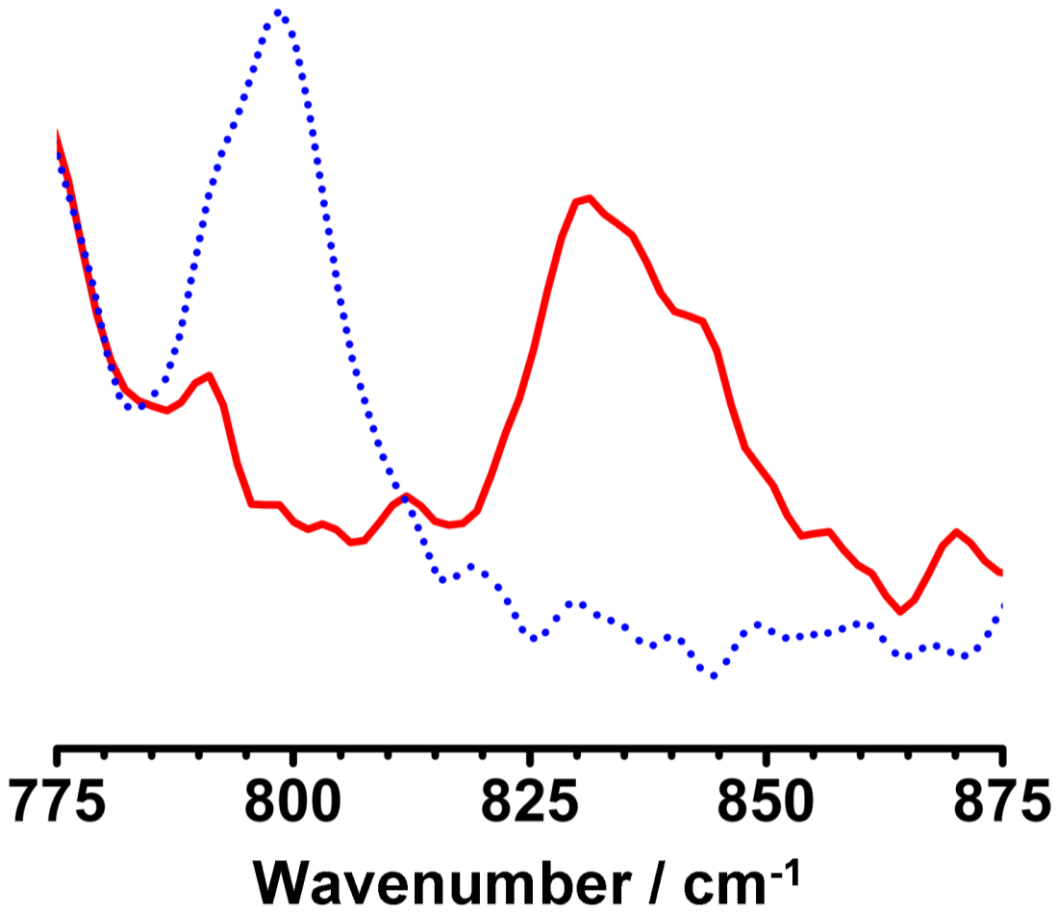

Figure 5.6. Resonance Raman spectra of oxoiron(IV) species produced using the ligand TMC-dma (Figure 5.1). Solid red line = ^{16}O; dotted blue line = ^{18}O.

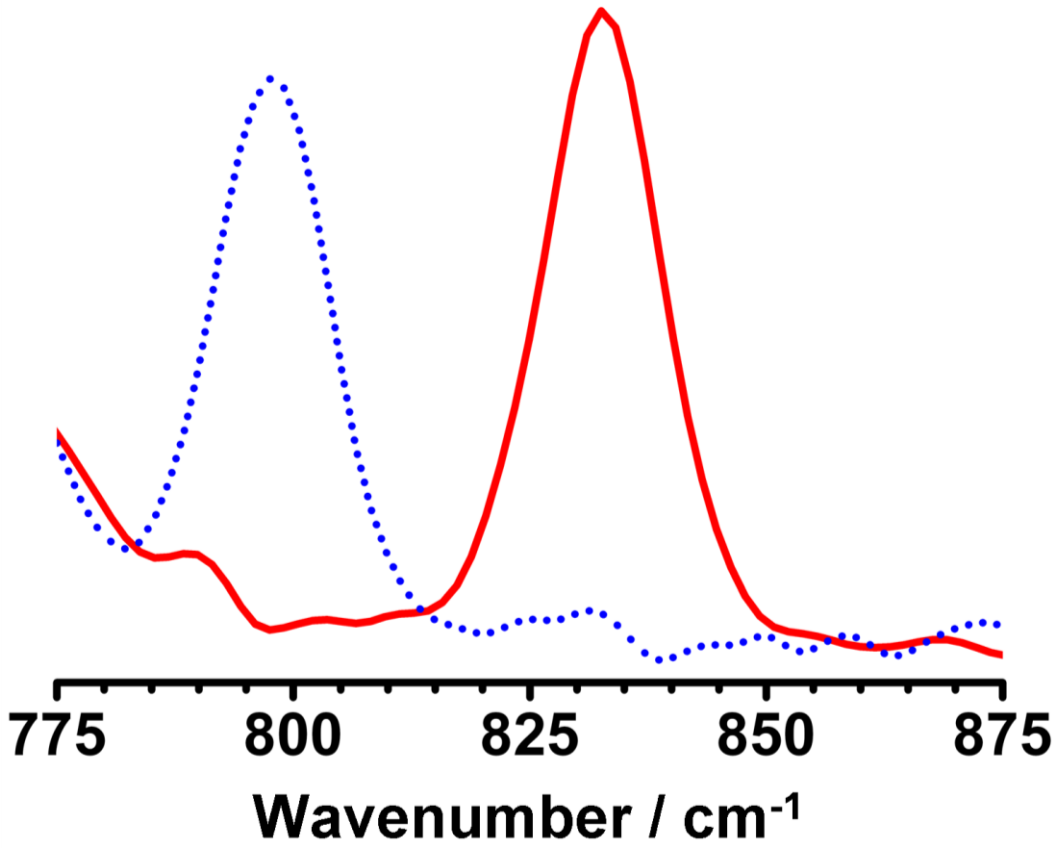

Figure 5.7. Resonance Raman spectra of oxoiron(IV) species produced using the ligand TMC-dmpa (Figure 5.1). Solid red line = ^{16}O; dotted blue line = ^{18}O.

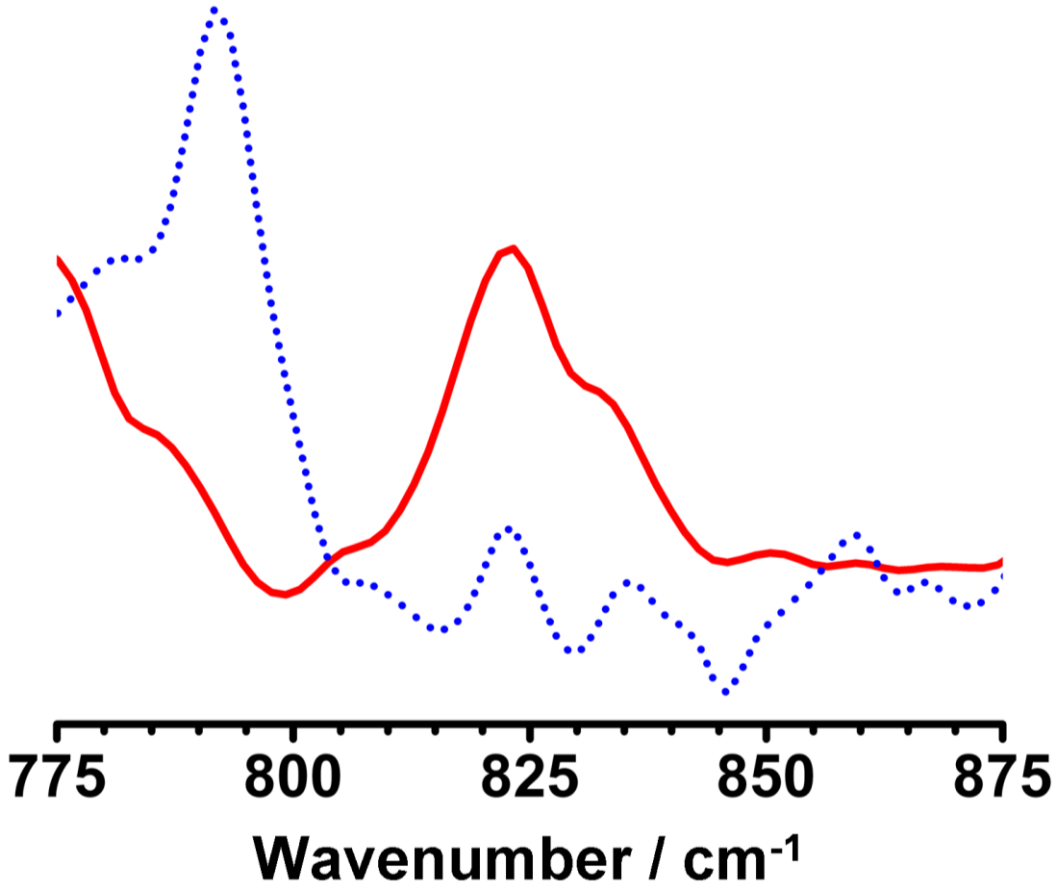

Figure 5.8. Resonance Raman spectra of oxoiron(IV) species produced using the ligand TMC-Py (Figure 5.1). Solid red line = ^{16}O; dotted blue line = ^{18}O.

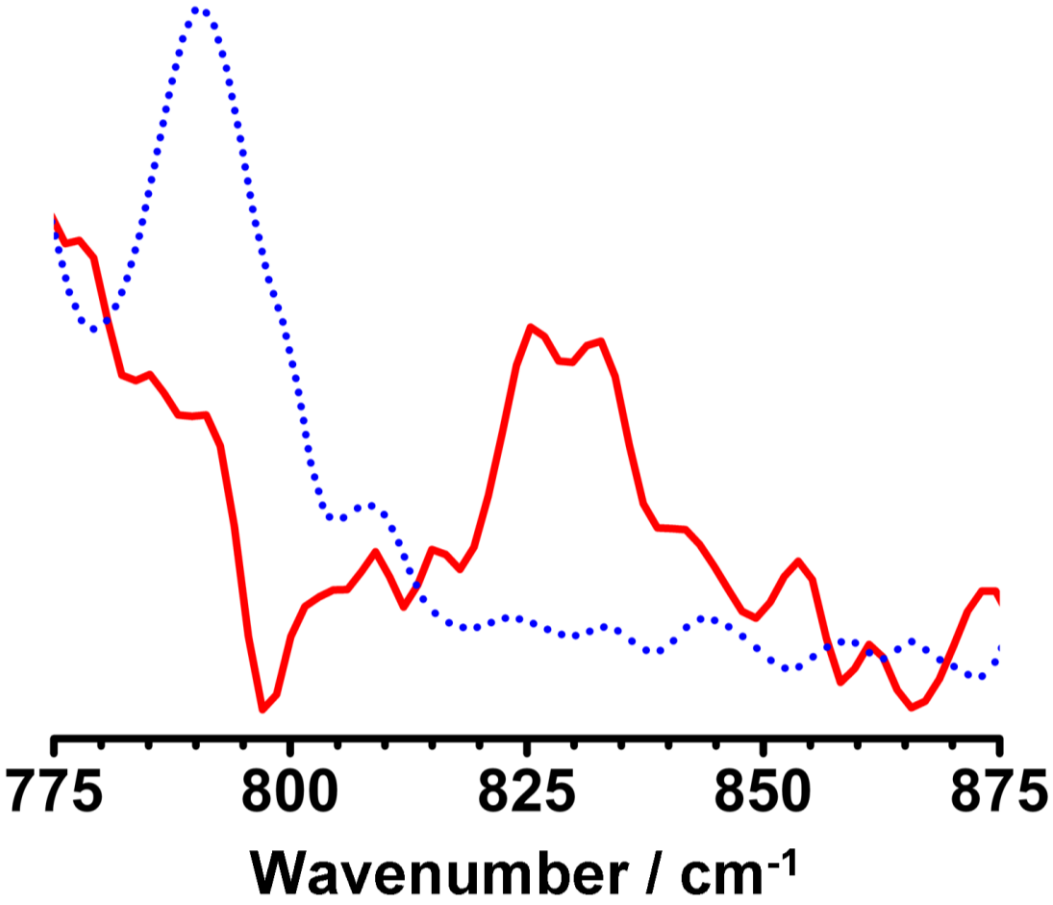

Figure 5.9. Resonance Raman spectra of oxoiron(IV) species produced using the ligand TMC-PyO (Figure 5.1). Solid red line = ^{16}O; dotted blue line = ^{18}O.

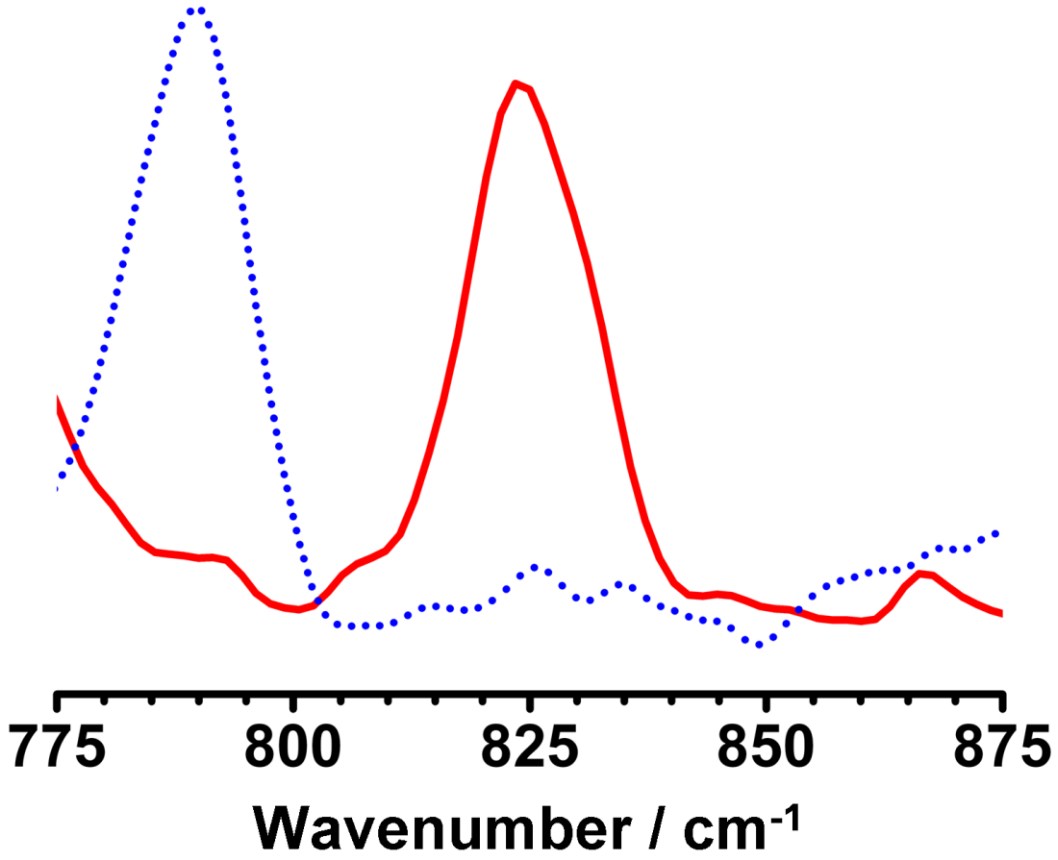

Figure 5.10. Resonance Raman spectra of oxoiron(IV) species produced using the ligand Lo (Figure 5.1). Solid red line = ^{16}O; dotted blue line = ^{18}O.

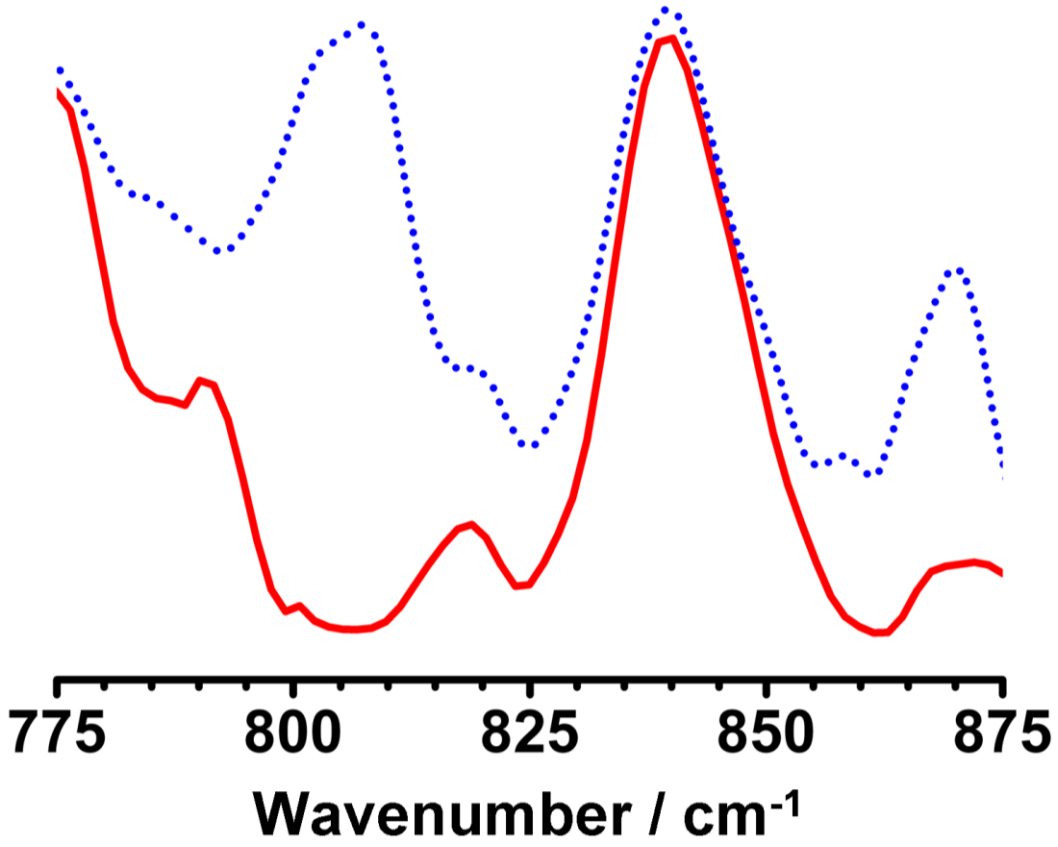

Figure 5.11. Resonance Raman spectra of oxoiron(IV) species produced using the ligand Lu (Figure 5.1). Solid red line = ^{16}O; dotted blue line = ^{18}O.

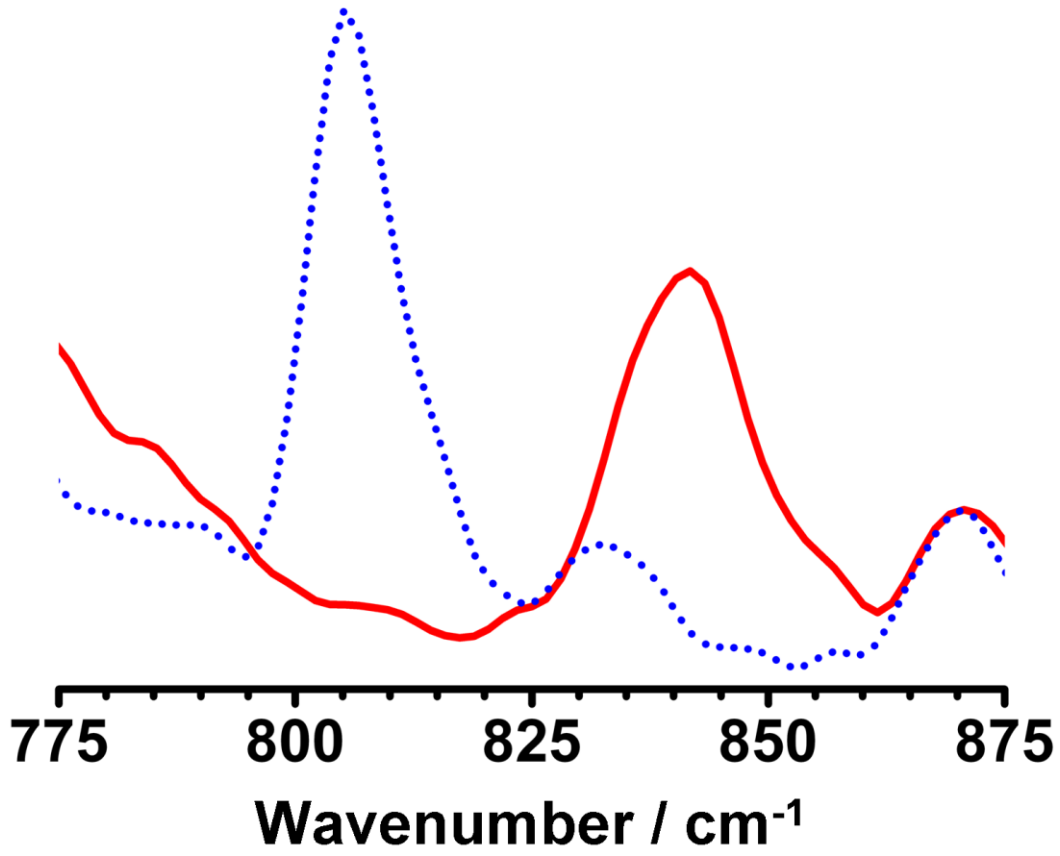

Figure 5.12. Resonance Raman spectra of oxoiron(IV) species produced using the ligand N4Py (Figure 5.1). Solid red line = ^{16}O; dotted blue line = ^{18}O.

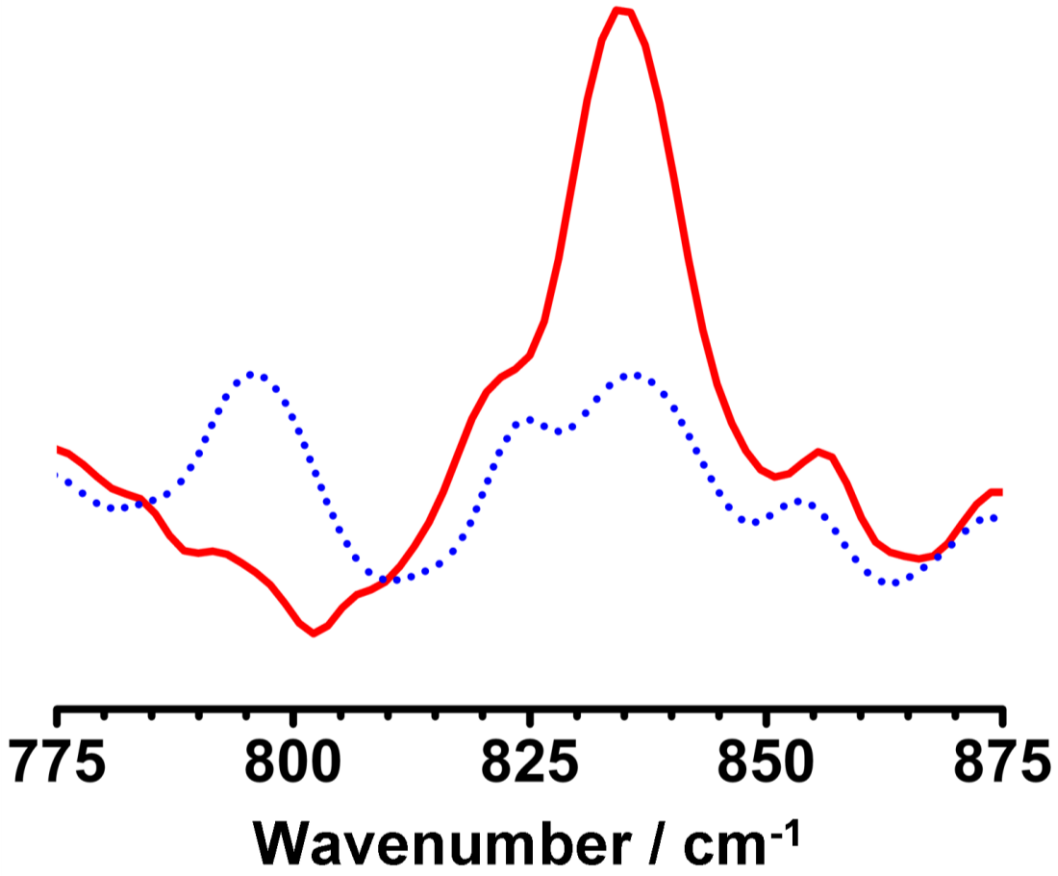

Figure 5.13. Resonance Raman spectra of oxoiron(IV) species produced using the ligand BnTPEN (Figure 5.1). Solid red line = ^{16}O; dotted blue line = ^{18}O.

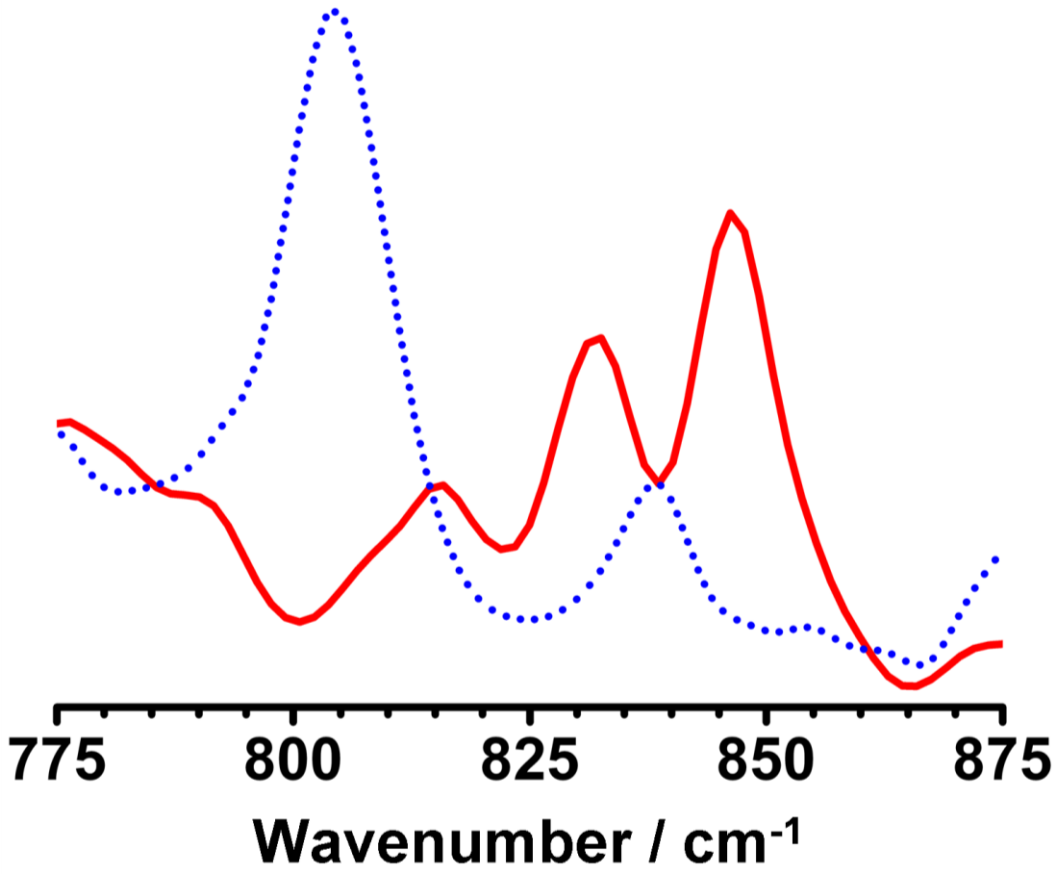

Figure 5.14. Resonance Raman spectra of oxoiron(IV) species produced using the ligand TACN-Py_2 (Figure 5.1). Solid red line = ^{16}O; dotted blue line = ^{18}O.

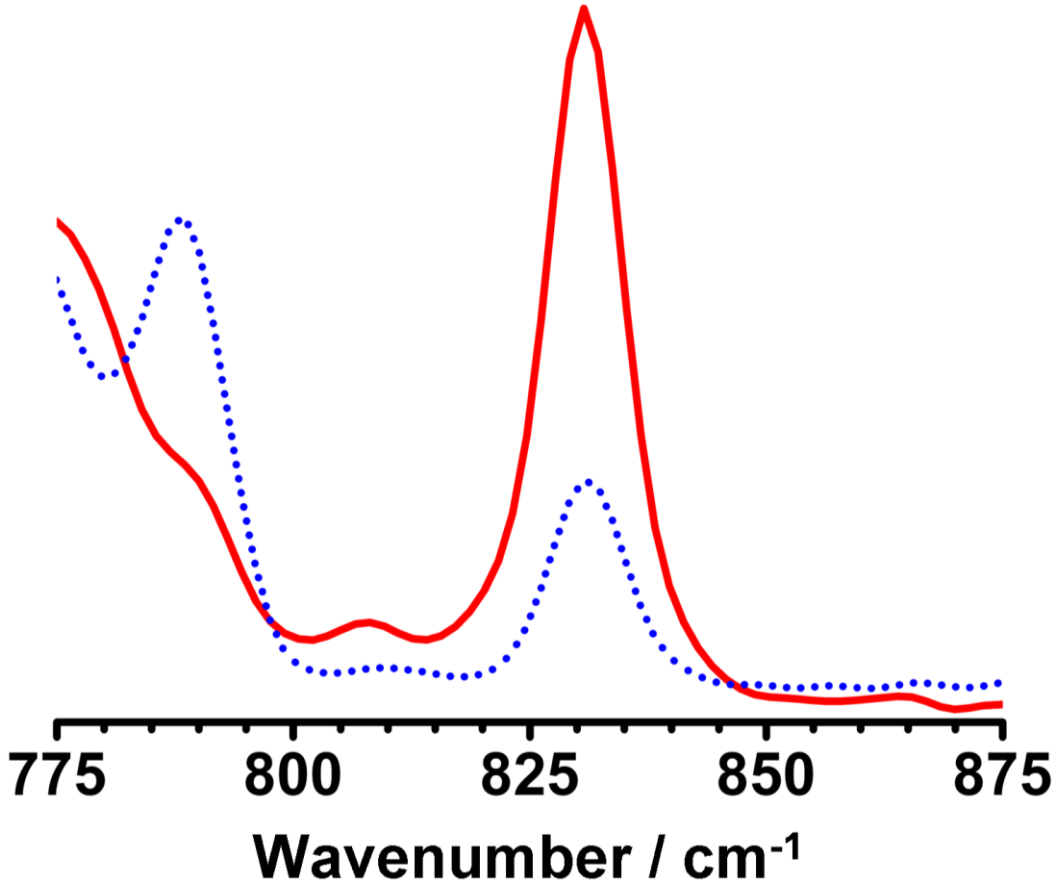

Figure 5.15. Resonance Raman spectra of oxoiron(IV) species produced using the ligand Me_2PyTACN (Figure 5.1). Solid red line = ^{16}O; dotted blue line = ^{18}O.

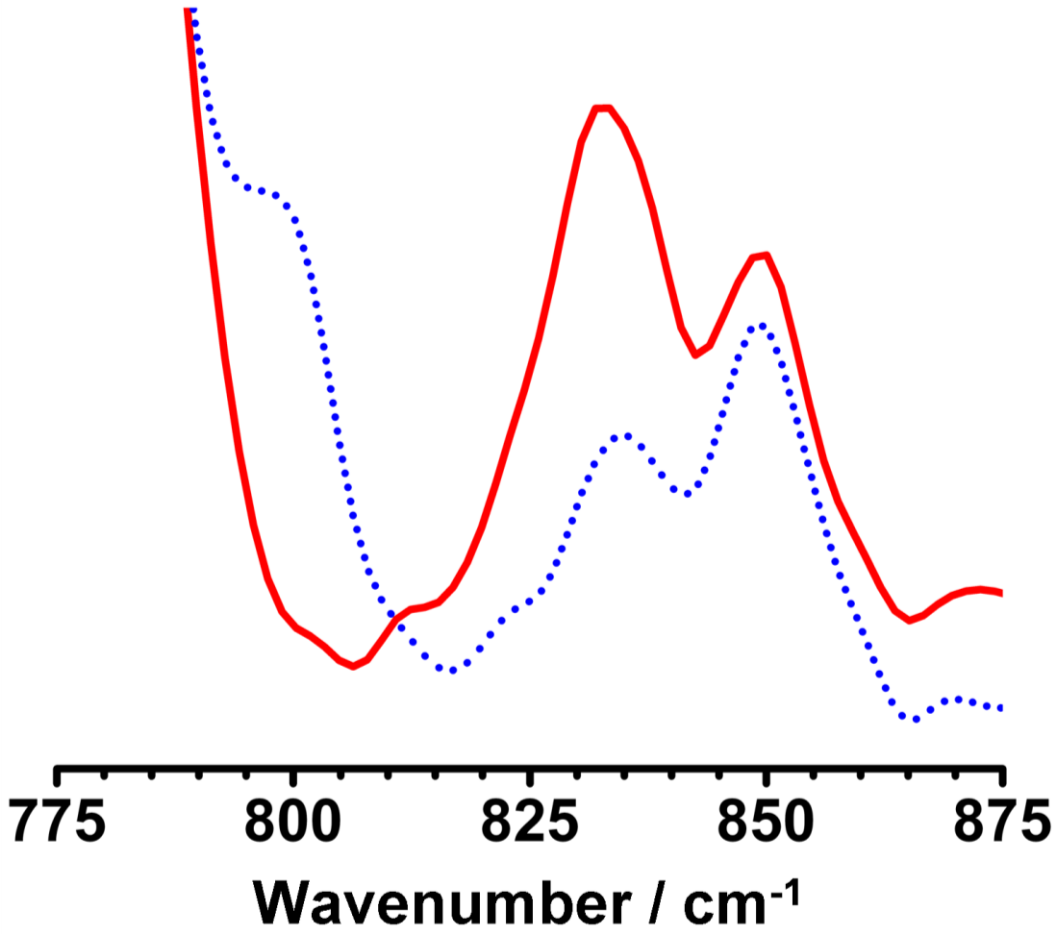

Figure 5.16. Resonance Raman spectra of oxoiron(IV) species produced using the ligand TPA (Figure 5.1). Solid red line = ^{16}O; dotted blue line = ^{18}O.

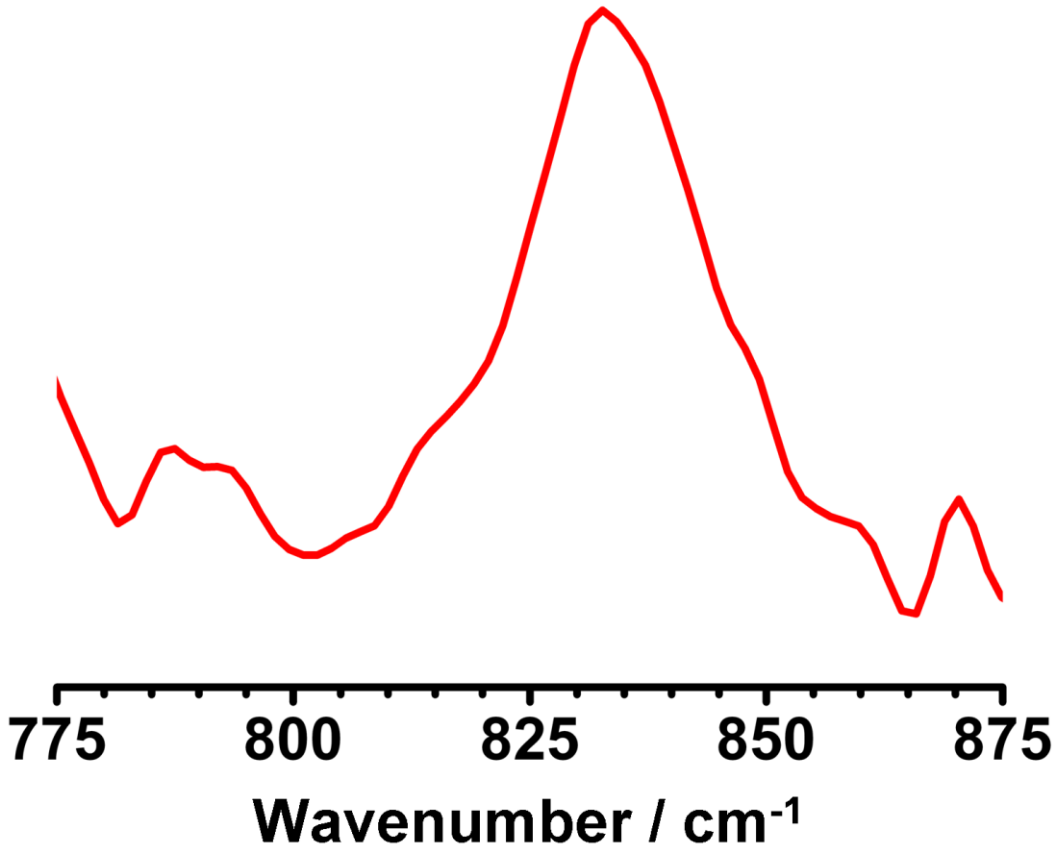

Figure 5.17. Resonance Raman spectrum of the oxoiron(IV) species produced using the ligand L^8Py_2 (Figure 5.1).

5.4 Discussion

Catalytically important oxoiron(IV) intermediates are often too transient to be observed in natural systems. As these species are frequently the intermediates of interest to chemists, much research has been focused on mimicking and elucidating the structures and properties of these moieties through the use of synthetic models.[33] Resonance Raman (rR) spectroscopy is one of the tools applied to this problem, but its successful employment has been limited due to

properties of oxoiron(IV) species that make them difficult to study using a technique that relies on laser excitation of the often unstable intermediates of interest. In the Results section, we outlined a procedure for dealing with these problems and showed some spectra collected using the new method.

Resonance Raman spectroscopy is used to investigate vibrational properties of molecules. In the case of oxoiron(IV) complexes, the vibration of primary interest is the Fe(IV)=O stretch, values of which are summarized in Table 5.1. The reactivities and stabilities of various oxoiron(IV) complexes vary widely, and this work was an attempt to find some correlation between $\nu_{Fe\text{-}O}$ and those characteristics. Jackson and coworkers reported lower observed $\nu_{Fe\text{-}O}$ values in conjunction with the addition of more basic *trans* donor ligands to oxoiron(IV) complexes produced using TMC (Figure 5.1) with stretching frequencies ranging from 814 to 854 cm^{-1}.[36] In our experiments using TMC-X (X = a pendant axial ligand in place of a methyl group) we did not observe this trend (Table 5.1 and Figures 5.4 to 5.9). In fact, no correlation between $\nu_{Fe\text{-}O}$ values ranging from 822 to 834 cm^{-1} and any ligand property was evident. The same is true for a series of pentadentate N5 ligands (Lo, Lu, N4Py, BnTPEN and TACN-Py_2). While the values have a slightly greater range (825 to 840 cm^{-1}) than those recorded for the TMC-X complexes, again no correlation involving $\nu_{Fe\text{-}O}$ values was observed.

In summary, we have devised a new method for employing rR spectroscopy as an investigative tool. The effectiveness of this technique has

been proven by using it to successfully produce spectra of over a dozen oxoiron(IV) intermediates as well as their isotopomers. Unfortunately, the data we collected did not offer significant insight into the properties of the species we investigated. However, this new procedure for gathering rR spectroscopic data will undoubtedly be put to good use in the future, providing spectra of complexes that would otherwise go unrecorded.

5.5 Acknowledgements

This work was supported by the National Institutes of Health through Grant GM-38767. We are indebted to Dr. Jason England, Dr. Kallol Ray, Dr. Genqiang "Ken" Xue, Dr. Anna Company and Laura Gomez, each of whom provided at least one of the intermediates examined in this work.

Chapter 6: Summary and Conclusions

6.1 Introduction

The main content of this thesis can be divided into four components: *(i)* the discovery and characterization of a group of novel (μ-η^1:η^1-peroxo)diiron(III) species, *(ii)* investigations into the stability of those intermediates, *(iii)* x-ray crystallographic characterization of tetranuclear iron(III) products and *(iv)* development and implementation of a new method for resonance Raman spectroscopy of oxoiron(IV) complexes. Chapter 2 introduces the unusual (μ-η^1:η^1-peroxo)diiron(III) intermediates and focuses on their characterization and identification. Chapter 3 explores factors that influence their formation and stabilization. The products from decay of these peroxo species are putatively tetranuclear iron(III) clusters. Several species falling into this class are examined in Chapter 4 via x-ray crystallography. Chapter 5 focuses on the evolution of a new technique for utilizing resonance Raman spectroscopy (rR) as an investigative tool and demonstrates its effectiveness using oxoiron(IV) intermediates.

6.2 Characterization of Two (μ-η^1:η^1-Peroxo)Diiron(III) Intermediates Produced from a Single Diiron(II) Precursor

For this work, we replaced the benzoate bridge of the well studied complex [Fe_2(N-EtHPTB)(OCPh)] (**1**•O_2CPh) with either diphenylphosphinate (**1**•O_2PPh_2) or dimethylarsinate (**1**•O_2AsMe_2). When reacted with oxygen in

solution at -40 °C, both of the new complexes produced green-blue (μ-η^1:η^1-peroxo)diiron(III) intermediates (**2**•O_2PPh_2 and **2**•O_2AsMe_2). The UV-Vis and resonance Raman spectra of these intermediates differed significantly from those of the deep-blue benzoate peroxo complex (**3**•O_2CPh). The visible absorption maxima of the new intermediates were red-shifted and the peroxo stretching frequencies determined using rR spectroscopy were approximately 50 cm^{-1} lower. When warmed to -30 °C, a solution of **2**•O_2PPh_2 converted to a deep-blue species (**3**•O_2PPh_2) with spectral characteristics nearly identical to those of **2**•O_2CPh. The same is not true of **2**•O_2AsMe_2. When a solution of **2**•O_2AsMe_2 was warmed, it converted to a yellow product (**4**•O_2AsMe_2) without visible appearance of a deep-blue intermediate akin to **3**•O_2PPh_2 and **3**•O_2CPh. The stability of **2**•O_2X intermediates appeared to be influenced by the O···O bite distance of the oxyanion bridge present in **1**•O_2X. Benzoate had the shortest distance and **2**•O_2CPh was not observed. Dimethylarsinate had the longest distance and **3**•O_2AsMe_2 was also not observed. Diphenylphosphinate had an intermediate distance and allowed us to observe both triply-bridged **2**•O_2PPh_2 and doubly-bridged **3**•O_2PPh_2. The bite distance of O_2PPh_2 appeared to be in the goldilocks zone, making **1**•O_2PPh_2 the only such complex reported in the literature.[84]

6.3 Factors Influencing Conversion Kinetics of Triply-Bridged (μ-η^1:η^1-Peroxo)Diiron(III) Intermediates to Doubly-Bridged (μ-η^1:η^1-Peroxo)Diiron(III) Intermediates

Following up on our work with **1**•O_2CPh, **1**•O_2PPh_2 and **1**•O_2AsMe_2, we synthesized several more complexes using various O_2X bridges chosen with the intent of examining the relationship between **2**•O_2X stability and oxyanion steric and electronic properties. In the process, we showed that every complex we examined produces the previously unobserved **2**•O_2X moiety. As with the previous work, we concluded the oxyanion O···O bite distance is the primary factor influencing **2**•O_2X stability. However, work with carboxylate bridges revealed a stability trend dependent on oxyanion steric bulk. There appears to be evidence for electronic effects, but further work is required before a definitive conclusion on this issue can be reached.

6.4 X-ray Crystallographic Examination of Tetrairon(III) Complexes

The (μ-η^1:η^1-peroxo)diiron(III) intermediates we have been examining putatively form tetrairon(III) decay products. We synthesized and crystallized several tetrairon(III) clusters using ligands with *N,N,N',N'*-tetrasubstituted 1,3-diaminopropan-2-ol backbones and examined them using x-ray crystallography. We concluded that the products could be divided into three classes based on the presence or absence of the originally bridging O_2X ligands and their coordination

modes if present. Steric bulk present on the amine subtituents appeared to influence the form taken by each tetranuclear iron(III) core.

6.5 Resonance Raman Investigation of Fe(IV)=O Stretching Frequencies

Solution state resonance Raman (rR) spectroscopy of oxoiron(IV) complexes has been inhibited by the nature of the intermediates. Using solutions of low enough concentration to prevent signal absorption produces spectra with poor signal-to-noise ratios. Raising the power of the excitation laser to intensify resonance enhanced signals usually results in photoreduction of the sample. The method introduced here solves both the concentration and photoreduction problems. By exciting the surface of frozen samples, we avoided the problem of signal absorbance. This also allowed us to use higher concentration solutions, thus producing better signal-to-noise ratios. The problem of photoreduction was solved by producing a smooth sample surface that could be moved through the laser beam. During the data collection process, the samples were kept in constant motion, meaning that fresh areas of sample surface were constantly moving into the excitation beam. We proved the efficacy of this method by collecting spectra of several oxoiron(IV) complexes and their isotopomers.

6.6 References

1. Wallar, B. J.; Lipscomb, J. D. *Chem. Rev.* **1996**, *96*, 2625-2658.
2. Sono, M.; Roach, M. P.; Coulter, E. D.; Dawson, J. H. *Chem. Rev.* **1996**, *96*, 2841-2887.
3. Solomon, E. I.; Brunold, T. C.; Davis, M. I.; Kemsley, J. N.; Lee, S.-K.; Lehnert, N.; Neese, F.; Skulan, A. J.; Yang, Y.-S.; Zhou, J. *Chem. Rev.* **2000**, *100*, 235-349.
4. Costas, M.; Mehn, M. P.; Jensen, M. P.; Que, L., Jr. *Chem. Rev.* **2004**, *104*, 939-986.
5. Que, L., Jr. In *Bioinorganic Catalysis*; 2nd ed.; Reedijk, J., Bouwman, E., Eds.; Marcel Dekker: New York, 1999, p 269-321.
6. Merkx, M.; Kopp, D. A.; Sazinsky, M. H.; Blazyk, J. L.; Müller, J.; Lippard, S. J. *Angew. Chem. Int. Ed.* **2001**, *40*, 2782-2807.
7. Fox, B. G.; Lyle, K. S.; Rogge, C. E. *Acc. Chem. Res.* **2004**, *37*, 421-429.
8. Bollinger, J. M., Jr.; Diao, Y.; Matthews, M. L.; Xing, G.; Krebs, C. *Dalton Trans.* **2009**, 905-914.
9. Sazinsky, M. H.; Lippard, S. J. *Acc. Chem. Res.* **2006**, *39*, 558-566.
10. Murray, L. J.; Lippard, S. J. *Acc. Chem. Res.* **2007**, *40*, 466-474.
11. Liu, K. E.; Valentine, A. M.; Qiu, D.; Edmondson, D. E.; Appelman, E. H.; Spiro, T. G.; Lippard, S. J. *J. Am. Chem. Soc.* **1995**, *117*, 4997-4998.
12. Bollinger, J. M., Jr.; Krebs, C.; Vicol, A.; Chen, S.; Ley, B. A.; Edmondson, D. E.; Huynh, B. H. *J. Am. Chem. Soc.* **1998**, *120*, 1094-1095.
13. Broadwater, J. A.; Ai, J.; Loehr, T. M.; Sanders-Loehr, J.; Fox, B. G. *Biochemistry* **1998**, *37*, 14664-14671.
14. Broadwater, J. A.; Achim, C.; Münck, E.; Fox, B. G. *Biochemistry* **1999**, 12197-12204.
15. Lee, S.-K.; Lipscomb, J. D. *Biochemistry* **1999**, *38*, 4423-4432.
16. Saleh, L.; Krebs, C.; Ley, B. A.; Naik, S.; Huynh, B. H.; Bollinger, J. M. *Biochemistry* **2004**, *43*, 5953-5964.
17. Murray, L. J.; Garcia-Serres, R.; Naik, S.; Huynh, B. H.; Lippard, S. J. *J. Am. Chem. Soc.* **2006**, *128*, 7458-7459.
18. Yun, D.; Garcia-Serres, R.; Chicalese, B. M.; An, Y. H.; Huynh, B. H.; Bollinger, J. M., Jr. *Biochemistry* **2007**, *46*, 1925-1932.
19. Vu, V. V.; Emerson, J. P.; Martinho, M.; Kim, Y. S.; Münck, E.; Park, M. H.; Que, J., L *Proc. Nat. Acad. Sci.* **2009**, *106*, 14814-14819.
20. Tshuva, E. Y.; Lippard, S. J. *Chem. Rev.* **2004**, *104*, 987-1012.
21. Ookubo, T.; Sugimoto, H.; Nagayama, T.; Masuda, H.; Sato, T.; Tanaka, K.; Maeda, Y.; Okawa, H.; Hayashi, Y.; Uehara, A.; Suzuki, M. *J. Am. Chem. Soc.* **1996**, *118*, 701-702.

22. Dong, Y.; Yan, S.; Young, V. G., Jr.; Que, L., Jr. *Angew. Chem. Int. Ed. Engl.* **1996**, *35*, 618-620.
23. Kim, K.; Lippard, S. J. *J. Am. Chem. Soc.* **1996**, *118*, 4914-4915.
24. Zhang, X.; Furutachi, H.; Fujinami, S.; Nagatomo, S.; Maeda, Y.; Watanabe, Y.; Kitagawa, T.; Suzuki, M. *J. Am. Chem. Soc.* **2005**, *127*, 826-827.
25. Kryatov, S. V.; Chavez, F. A.; Reynolds, A. M.; Rybak-Akimova, E. V.; Que, L., Jr.; Tolman, W. B. *Inorg. Chem.* **2004**, *43*, 2141-2150.
26. Korendovych, I. V.; Kryatov, S. V.; Reiff, W. M.; Rybak-Akimova, E. V. *Inorg. Chem.* **2005**, *44*, 8656-8658.
27. Kryatov, S. V.; Taktak, S.; Korendovych, I. V.; Rybak-Akimova, E. V.; Kaizer, J.; Torelli, S.; Shan, X.; Mandal, S.; MacMurdo, V.; Mairata i Payeras, A.; Que, L., Jr. *Inorg. Chem.* **2005**, *44*, 85-99.
28. Yoon, S.; Lippard, S. J. *Inorg. Chem.* **2006**, *45*, 5438-5446.
29. Fiedler, A. T.; Shan, X.; Mehn, M. P.; Kaizer, J.; Torelli, S.; Frisch, J. R.; Kodera, M.; Que, L., Jr. *J. Phys. Chem. A* **2008**, *112*, 13037–13044.
30. Than, R.; Schrodt, A.; Westerheide, L.; Eldik, R. v.; Krebs, B. *Eur. J. Inorg. Chem.* **1999**, 1537-1543.
31. Yan, S.; Cheng, P.; Wang, Q.; Liao, D.; Jiang, Z.; Wang, G. *Science in China, Series B: Chemistry* **2000**, *43*, 405-411.
32. Koehntop, K. D.; Emerson, J. P.; Que, L., Jr. *J. Biol. Inorg. Chem.* **2005**, *10*, 87-93.
33. Que, L., Jr. *Acc. Chem. Res.* **2007**, *40*, 493-500.
34. Sastri, C. V.; Park, M. J.; Ohta, T.; Jackson, T. A.; Stubna, A.; Seo, M. S.; Lee, J.; Kim, J.; Kitagawa, T.; Münck, E.; Que, L., Jr.; Nam, W. *J. Am. Chem. Soc.* **2005**, *127*, 12494-12495.
35. Suh, Y.; Seo, M. S.; Kim, K. M.; Kim, Y. S.; Jang, H. G.; Tosha, T.; Kitagawa, T.; Kim, J.; Nam, W. *J. Inorg. Biochem.* **2006**, *100*, 627-633.
36. Jackson, T. A.; Rohde, J.-U.; Seo, M. S.; Sastri, C. V.; DeHont, R.; Ohta, T.; Kitagawa, T.; Münck, E.; Nam, W.; Que, L., Jr. *J. Am. Chem. Soc.* **2008**, *130*, 12394-12407.
37. Thibon, A.; England, J.; Martinho, M.; Young, V. G., Jr.; Frisch, J. R.; Guillot, R.; Girerd, J.-J.; Münck, E.; Que, L., Jr.; Banse, F. *Angew. Chem. Int. Ed.* **2008**, *47*, 7064-7067.
38. Lee, Y.-M.; Dhuri, S. N.; Sawant, S. C.; Cho, J.; Kubo, M.; Ogura, T.; Fukuzumi, S.; Nam, W. *Angew. Chem. Int. Ed.* **2009**, *48*, 1803-1806.
39. England, J.; Martinho, M.; Farquhar, E. R.; Frisch, J. R.; Bominaar, E. L.; Münck, E.; Que, J., L *Angew. Chem. Int. Ed.* **2009**, *48*, 3622-3626.
40. Ménage, S.; Brennan, B. A.; Juarez-Garcia, C.; Münck, E.; Que, L., Jr. *J. Am. Chem. Soc.* **1990**, *112*, 6423-6425.
41. McKee, V.; Zvagulis, M.; Dagdigian, J. V.; Patch, M. G.; Reed, C. A. *J. Am. Chem. Soc.* **1984**, *106*, 4765-4772.

42. Armarego, W. L. F.; Perrin, D. D. *Purification of Laboratory Chemicals*; Butterworth-Heinemann: Oxford, 1997.
43. Hagen, K. S. *Inorg. Chem.* **2000**, *39*, 5867-5869.
44. Bruker *SMART V5.054*; Bruker Analytical X-Ray Systems: Madison, WI, 2001.
45. Blessing, R. H. *Acta Cryst.* **1995**, *A51*, 33-38.
46. Bruker *SAINT+ V6.45*; Bruker Analytical X-Ray Systems: Madison, WI, 2003.
47. Bruker *SHELXTL V6.14*; Bruker Analytical X-Ray Systems: Madison, WI, 2000.
48. Scarrow, R. C.; Trimitsis, M. G.; Buck, C. P.; Grove, G. N.; Cowling, R. A.; Nelson, M. J. *Biochemistry* **1994**, *33*, 15023-15035.
49. George, G. N.; Pickering, I. J.; Stanford Synchrotron Radiation Laboratory, Stanford Linear Accelerator Center: Stanford, California, 2000.
50. Riggs-Gelasco, P. J.; Stemmler, T. L.; Penner-Hahn, J. E. *Coord. Chem. Rev.* **1995**, *144*, 245-286.
51. Dong, Y.; Ménage, S.; Brennan, B. A.; Elgren, T. E.; Jang, H. G.; Pearce, L. L.; Que, L., Jr. *J. Am. Chem. Soc.* **1993**, *115*, 1851-1859.
52. Addison, A. W.; Rao, T. N.; Reedijk, J.; Rijn, J. v.; Verschoor, G. C. *J. Chem. Soc., Dalton Trans.* **1984**, 1349-1356.
53. Mirica, L. M.; Vance, M.; Rudd, D. J.; Hedman, B.; Hodgson, K. O.; Solomon, E. I.; Stack, T. D. P. *J. Am. Chem. Soc.* **2002**, *124*, 9332-9333.
54. Kim, E.; Shearer, J.; Lu, S.; Moënne-Loccoz, P.; Helton, M. E.; Kaderli, S.; Zuberbühler, A. D.; Karlin, K. D. *J. Am. Chem. Soc.* **2004**, *126*, 12716-12717.
55. Chishiro, T.; Shimazaki, Y.; Tani, F.; Tachi, Y.; Naruta, Y.; Karasawa, S.; Hayami, S.; Maeda, Y. *Angew. Chem., Int. Ed.* **2003**, *42*, 2788-2791.
56. Yamashita, M.; Furutachi, H.; Tosha, T.; Fujinami, S.; Saito, W.; Maeda, Y.; Takahashi, K.; Tanaka, K.; Kitagawa, T.; Suzuki, M. *J. Am. Chem. Soc.* **2007**, *129*, 2-3.
57. Kauffmann, K. E.; Münck, E. In *Spectroscopic Methods in Bioinorganic Chemistry*; Solomon, E. I., Hodgson, K. O., Eds.; American Chemical Society: Washington, D.C., 1998.
58. Krebs, C.; Bollinger, J. M., Jr.; Theil, E. C.; Huynh, B. H. *J. Biol. Inorg. Chem.* **2002**, *7*, 863-869.
59. Westre, T. E.; Kennepohl, P.; DeWitt, J. G.; Hedman, B.; Hodgson, K. O.; Solomon, E. I. *J. Am. Chem. Soc.* **1997**, *119*, 6297-6314.
60. Roe, A. L.; Schneider, D. J.; Mayer, R. J.; Pyrz, J. W.; Widom, J.; Que, L., Jr. *J. Am. Chem. Soc.* **1984**, *106*, 1676-1681.
61. Hedman, B.; Co, M. S.; Armstrong, W. H.; Hodgson, K. O.; Lippard, S. J. *Inorg. Chem.* **1986**, *25*, 3708-3711.

62. Eulering, B.; Ahlers, F.; Zippel, F.; Schmidt, M.; Nolting, H.-F.; Krebs, B. *J. Chem. Soc., Chem. Commun.* **1995**, 1305-1307.
63. Eulering, B.; Schmidt, M.; Pinkernell, U.; Karst, U.; Krebs, B. *Angew. Chem. Int. Ed. Engl.* **1996**, *35*, 1973-1974.
64. Slater, J. C. *J. Chem. Phys.* **1964**, *41*, 3199-3204.
65. Chen, Q.; Lynch, J. B.; Gomez-Romero, P.; Ben-Hussein, A.; Jameson, G. B.; O'Connor, C. J.; Que, L., Jr. *Inorg. Chem.* **1988**, *27*, 2673-2681.
66. Feig, A. L.; Becker, M.; Schindler, S.; van Eldik, R.; Lippard, S. J. *Inorg. Chem.* **1996**, *35*, 2590-2601.
67. Brunold, T. C.; Tamura, N.; Kitajima, M.; Moro-oka, Y.; Solomon, E. I. *J. Am. Chem. Soc.* **1998**, *120*, 5674-5690.
68. Footnote.
69. Feig, A. L.; Lippard, S. J. *J. Am. Chem. Soc.* **1994**, *116*, 8410-8411.
70. Kilpatrick, M. L. *J. Am. Chem. Soc.* **1949**, *71*, 2607-2610.
71. Shin, T.-W.; Kim, K.; Lee, I.-J. *J. Sol. Chem.* **1997**, *26*, 379-390.
72. Edmundson, R. S. *Dictionary of Organophosphorus Compounds*; Chapman and Hall: New York, 1988.
73. Lide, D. R. *CRC Handbook of Chemistry and Physics*; 72nd ed.; CRC Press: Boston, 1991.
74. Rardin, R. L.; Tolman, W. B.; Lippard, S. J. *New J. Chem.* **1991**, *15*, 417-430.
75. Rosenzweig, A. C.; Frederick, C. A.; Lippard, S. J.; Nordlund, P. *Nature* **1993**, *366*, 537-543.
76. Whittington, D. A.; Lippard, S. J. *J. Am. Chem. Soc.* **2001**, *123*, 827-838.
77. Sazinsky, M. H.; Bard, J.; Donato, A. D.; Lippard, S. J. *J. Biol. Chem.* **2004**, *279*, 30600-30610.
78. Nordlund, P.; Sjöberg, B.-M.; Eklund, H. *Nature* **1990**, *345*, 593-598.
79. Nordlund, P.; Eklund, H. *J. Mol. Biol.* **1993**, *232*, 123-164.
80. Rehr, J. J.; Mustre de Leon, J.; Zabinsky, S. I.; Albers, R. C. *J. Am. Chem. Soc.* **1991**, *113*, 5135-5140.
81. Leon, J. M. d.; Rehr, J. J.; Zabinsky, S. I.; Albers, R. C. *Phys. Rev. B* **1991**, *44*, 4146-4156.
82. Ravel, B.; Newville, M. *J. Synchrotron Rad.* **2005**, *12*, 537-541.
83. Spek, A. L. *PLATON. A multipurpose crystallographic tool*; Utrecht University: Utrecht, The Netherlands, 2002.
84. Frisch, J. R.; Vu, V. V.; Martinho, M.; Münck, E.; Que, L., Jr. *Inorg. Chem.* **2009**, *48*, 8325-8336.
85. Kilpatrick, M. L.; Fackenthal, E. *Journal of the Electrochemical Society* **1953**, *100*, 185-193.
86. Sergeant, E. P.; Dempsey, B. *Ionisation Constants of Organic Acids*; Pergamon Press: New York, 1979.

87. Scanlon, P. M.; Thunberg, J. C. *United States Patent #3,780, 100* **1973**.
88. Costas, M.; Cady, C. W.; Kryatov, S. V.; Ray, M.; Ryan, M. J.; Rybak-Akimova, E. V.; Que, L., Jr. *Inorg. Chem.* **2003**, *42*, 7519-7530.
89. Altomare, A.; Burla, M. C.; Camalli, M.; Cascarano, G.; Giacovazzo, C.; Guagliardi, A.; Moliterni, A. G. G.; Polidori, G.; Spagna, R. *J. Appl. Cryst.* **1999**, *32*, 115-119.
90. Spek, A. L. *Acta Cryst.* **1990**, *A46*, C34.
91. Horn, A.; Neves, A.; Bortoluzzi, A. J.; Drago, V.; Ortiz, W. A. *Inorg. Chem. Comm.* **2001**, *4*, 173-176.
92. Satcher, J. H., Jr.; Olmstead, M. M.; Droge, M. W.; Parkin, S. R.; Noll, B. C.; May, L.; Balch, A. L. *Inorg. Chem.* **1998**, *37*, 6751-6758.
93. Jameson, D. L.; Xie, C.-L.; Hendrickson, D. N.; Potenza, J. A.; Schugar, H. J. *J. Am. Chem. Soc.* **1987**, *109*, 740-746.
94. Tanase, T.; Inagaki, T.; Yamada, Y.; Kato, M.; Ota, E.; Yamazaki, M.; Sato, M.; Mori, W.; Yamaguchi, K.; Mikuriya, M.; Takahashi, M.; Takeda, M.; Kinoshita, I.; Yano, S. *J. Chem. Soc., Dalton Trans.* **1998**, 713-718.
95. Tanase, T.; Inoue, C.; Ota, E.; Yano, S.; Takahashi, M.; Takeda, M. *Inorg. Chim. Acta* **2000**, *297*, 18-26.
96. Schmitt, W.; Jordan, P. A.; Henderson, R. K.; Moore, G. R.; Anson, C. E.; Powell, A. K. *Coord. Chem. Rev.* **2002**, *228*, 115-126.
97. Schmitt, W.; Anson, C. E.; Sessoli, R.; van Veen, M.; Powell, A. K. *J. Inorg. Biochem.* **2002**, *91*, 173-189.
98. Schmitt, W.; Anson, C. E.; Pilawa, B.; Powell, A. K. *Z. Anorg. Allg. Chem.* **2002**, *628*, 2443-2457.
99. Westerheide, L.; Müller, F. K.; Than, R.; Krebs, B. *Inorg. Chem.* **2001**, *40*, 1951-1961.
100. Fernandes, C.; Neves, A.; Vencato, I.; Bortoluzzi, A. J.; Drago, V.; Weyhermüller, T.; Rentschler, E. *Chem. Lett.* **2000**, 540-541.
101. Sessler, J. L.; Sibert, J. W.; Burrell, A. K.; Lynch, V.; Markert, J. T.; Wooten, C. L. *Inorg. Chem.* **1993**, *32*, 4277-4283.